UiT The Arctic University of Norway

Faculty of Science and Technology
Department of Physics and Technology

Automatic validation of Sentinel-1 borne snow avalanche detections

Jarle Langseth Pedersen

Master’s thesis in Energy, Environment and Climate EOM-3901 June 2020

This thesis document was typeset using the *UiT Thesis LaTeX Template*.

“Algorithms don’t do a good job of detecting their own flaws.”
–Clay Shirky

Abstract

Snow avalanches threaten human lives, settlements and roads in snow covered mountainous areas. For avalanche forecasting, knowledge of the spatio-temporal occurrence of avalanche activity is critical. Automatic avalanche detection algorithms have been developed to enable consistent avalanche activity monitoring for large regions. The Satskred avalanche detection algorithm developed by NORCE applies synthetic aperture radar (SAR) data from the Sentinel-1 satellite constellation and detects avalanches through a relative increase in energy scattered back to the radar from avalanche debris. Field Validation of all automatically detected features is desirable, but not achievable due to weather- , light- , and avalanche danger-conditions as well as avalanches occurring at remote locations.

In this thesis, an algorithm is presented for automatic comparison of the Satskred avalanche detections to crowd-sourced avalanche observations from regObs, the Norwegian public registry for snow-, weather-, flood-, and ice observations. Thereby, the validation set of field observed avalanches grows with every registered observation and validation of detected features can be performed without further manual intervention. To evaluate whether a detection matches an observed avalanche, the comparison algorithm initially filters detections by time period to ensure temporal similarity. Then, the detection is evaluated with regards to distance, slope aspect and membership of the same drainage basin region as the observation to ensure spatial similarity. If the detection fulfills all the similarity requirements, it is considered to likely represent the same avalanche.

Studying a 120 x 86 km area centered over Tromsø in Northern Norway, 308 avalanche observations from 2014 - 2019 were automatically compared to a set of avalanche detections from the same area and time period. The field observations were used as a truth-set and the resulting probability of detection (POD) for the Satskred algorithm was 25.3% (78 out of 308). Further analysis identified trends of larger POD for wet- than dry avalanches, and an increasing POD with avalanche size. A large proportion of avalanches entered to the regObs database are dry slab avalanches, which was found to partly explain the low POD.

Acknowledgements

First of all, I would like to thank my supervisors Anthony Paul Doulgeris and Markus Eckerstorfer. You have supported me from the beginning and encouraged me to work hard. Thank you for all your time, suggestions, reading and commenting that truly raised the quality of the thesis. Also, thank you Markus for suggesting this very interesting project and believing that I would be able to do it.

NORCE is thanked for giving me access to the dataset of avalanche detections, as well as the masks applied by the detection algorithm.

regObs is thanked for providing freely available avalanche observations through an easy-to-use API. The python code by Ragnar Ekker made retrieving observations from regObs understandable. Jørgen Loe Kvalberg is also thanked for answering all my technical regObs-related questions.

Maren, takk for den imponerende tålmodigheten du har vist og for all hjelp og støtte. Gjennomlesing og retting har gjort at teksten er oppe på ditt nivå i engelsk.

Til gjengen i Barista Boyz: Takk for alle kaffekopper, turer, faglige diskusjoner og alle de andre stundene med lite faglig fokus gjennom fem år. Vi har klart dette sammen.

Contents

List of Figures

List of Tables

1

Introduction

1.1 Background for the study

Snow avalanches, hereafter called avalanches, are a significant natural hazard to human lives and infrastructure in snow covered mountainous areas. Over the last 10 winters (2009 - 2019), a total of 75 people have lost their lives in avalanche accidents in Norway (NGI, 2019). Northern Norway is overrepresented in these statistics with 18 out of 28 fatalities in the period 2014 - 2019 (Varsom, 2019b).

Avalanche forecasting is one of the approaches used to try to mitigate avalanche risk. Knowledge of recent avalanche activity is vital when creating avalanche bulletins, as there is a strong correlation between avalanche activity and avalanche risk (Schweizer, 2003). However, a complete and repeatedly updated overview of avalanche activity within a given forecasting region is not achievable using field based observations. A recent study (Eckerstorfer et al., 2018) has shown that avalanche debris is detectable in Sentinel-1 SAR images, consistently both in space and time.

The processing chain developed at NORCE outputs automatic avalanche detections on a daily basis. Both manual detections and field observations of avalanches are currently the benchmark used to improve the performance of the automatic detection algorithm. Field validation of both automatic and manual avalanche detections is desirable, but not achievable in a consistent manner due to weather- , light- , and avalanche danger-conditions as well as avalanches occurring at remote locations. Consequently, the dataset of field observed avalanches is much smaller than those detected in SAR images.

One way to increase the number of available field observations is to make use of the crowd-sourced information at www.regObs.no, where the public is encouraged to register their avalanche observations.

1.2 Objectives

The overall objective of the project is to improve the automatic avalanche detection algorithm by systematically comparing automatic detections to field-observed avalanches.

The motivation for creating an algorithm to compare avalanche detections to avalanche observations from regObs is to enable validation of the detections against field data without the workload associated with manually reviewing all the observations.

Therefore, the secondary objectives of the project are:

- Design and test a prototype that automatically compares avalanche detections with crowd-sourced field observations of avalanches in the regObs database.
- Evaluate and discuss the effectiveness of the prototype.
- Gain an improved understanding of the capabilities of the automatic avalanche detection algorithm in terms of avalanche sizes, avalanche types, snow conditions and spatial occurrence.

2

Theory

This chapter presents some of the basic theory on avalanches, avalanche forecasting and avalanche detection using remote sensing, with emphasis on spaceborne radars.

2.1 Avalanche theory

Avalanches are masses of snow that rapidly slide, tumble or flow down a steep slope. They can be categorized by several factors such as release mechanism, size, water content and velocity. A common distinction is made between slab avalanches and loose snow avalanches, in addition to separating between dry and wet avalanches (NVE, 2016). Figure 2.1 illustrates an avalanche with the nomenclature used in this thesis. *Deposits* and *avalanche debris* will be used interchangeably.

Dry slab avalanches account for 99% of all avalanches triggered by recreationists (Landrø, 2007, p.44). According to Schweizer et al. (2003a), slab avalanches occur when an extended weak layer below a cohesive slab no longer withstands the shear forces and fractures (Figure 2.2a). These avalanches can be recognized by a distinct crown and debris deposited as various sized blocks (Figure 2.2a).

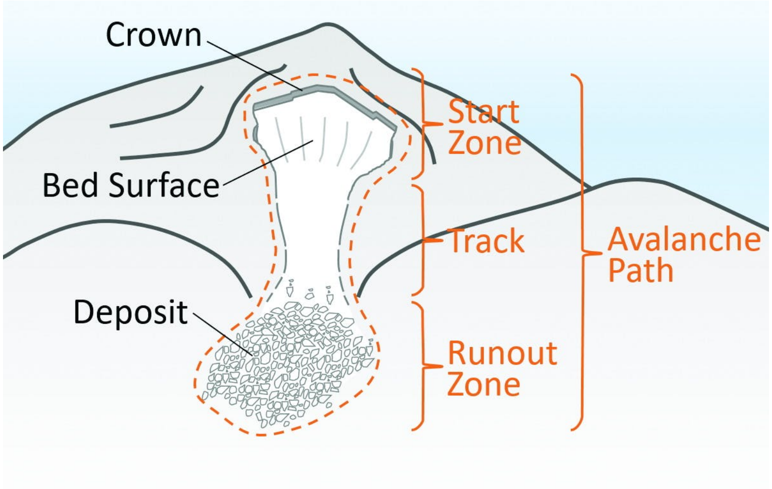

Figure 2.1: Overview of an avalanche path with names attached to each zone. Retrieved from Avalanche Canada (2020)

In a snowpack with less cohesion, a loose snow avalanche can form through a chain reaction initiated by a single moving grain. The avalanche collects more mass as it descends and spreads into a elongated pear-like shape, as illustrated in Figure 2.2b (Landrø, 2007, p.44).

Dry and wet avalanches can often be distinguished by observing the color of the debris, as wet avalanches tend to have a more blueish color. Furthermore, wet avalanches have a larger ability to erode the underlying soil, and the debris can thus comprise a mixture of snow, rocks and finer fractions (NVE, 2016).


(a) (b)

Figure 2.2: (a) Dry slab avalanche triggered by skier. Photo by Leif@ObsKorps, retrieved and modified from www.regobs.no. (b) Wet loose snow avalanches. Retrieved from EAWS (2019).

There are three other common snow related avalanche types in addition to slab- and loose snow avalanches: cornice fall avalanches, glide avalanches and slush avalanches. Cornices form incrementally along ridges during the winter and can fail due to their own weight or potentially the added weight of a person. When breaking off, the cornice can occasionally trigger avalanches on the slope beneath it despite of relatively stable snow conditions (NVE, 2016).

Glide avalanches occur when the entire snowpack slowly slides on the ground. The gliding process, caused by melt-water lubricating the ground, can often last for days or weeks before the avalanche releases. Smooth slopes in wet climates are most prone to glide avalanches (Tremper, 2008, p.33).

Slush avalanches can release on gentle slopes and consist of water-saturated snow flowing rapidly like a flood. The high water content is often caused by rapid melting or by another avalanche damming a river. Slush avalanches have a high destructive potential due to their high density and velocity (NVE, 2013).

Studies of catastrophic avalanches have found that very few avalanches released on slopes with less than 30° slope angle (Ammann, 2000; Schweizer and Jamieson, 2001). With that said, it is important to recognize that avalanche tracks can easily extend into terrain $< 30^\circ$, where the debris comes to rest in the runout zones (Figure 2.1).

The avalanche size classification used in this thesis follows the sizes used for public avalanche forecasting in Norway (Table 2.1). Avalanches are divided into five size categories defined, among other things, by the potential damage caused (Varsom, 2020c).

Table 2.1: Avalanche size categories, modified after Varsom (2020c) and EAWS (2020).

Size	Typical volume	Typical length	Could bury or destroy
1 - Small	$100\ m^3$	10 m	
2 - Medium	$1000\ m^3$	100 m	Person
3 - Large	$10,000\ m^3$	1000 m	Car, hut
4 - Very large	$100,000\ m^3$	2000 m	Several buildings or large amount of forest
5 - Extremely large	$> 100,000\ m^3$	3000 m	Villages. Gauges the landscape

2.2 Avalanche forecasting

One of the approaches used to try to mitigate avalanche risk is avalanche forecasting. The general public receives through an avalanche forecast, updated information on the current snow stability and avalanche danger, in addition to a forecast of the near future situation (McClung, 2002a). The typical content of an avalanche forecast is described by Techel et al. (2018) as: Avalanche danger level, most critical terrain, avalanche problems, hazard description and information of the snowpack and weather. The forecast is valid for a specified region and time span.

In 2013, the Norwegian public avalanche danger service Varsom (www.varsom.no) was established as a response to the numerous lives lost in avalanche accidents and the problems avalanches cause for transport and settlements. The service is a member of the European Avalanche Warning Services (EAWS) and follows European standards (Engeset, 2013). By using international standards, backcountry users can be sure that the forecasted danger levels are equivalent to the danger levels in their home region.

The forecasting process must begin with collecting data to establish the current avalanche situation as accurately as possible (McClung, 2002b). The data is collected by trained observers in the field through stability tests, snow measurements etc., in addition to snow- and weather- data from computer models and weather stations. The general public is also encouraged to register their relevant avalanche observations through the natural hazard observation site www.regObs.no or Varsom regObs mobile app (Engeset et al., 2018) (Section 3.2). When the knowledge of the current situation is sufficient, a forecast for the following day can be made by predicting how the forecasted weather will affect the snowpack and consequently the avalanche danger (Varsom, 2019a). Therefore, avalanche forecasting also has the time-scale problem of rapidly increasing uncertainty associated with weather forecasting.

The term *information entropy* is, according to LaChapelle (1980), often equated with uncertainty and can be used to describe how hard it is to apply relevant information to stability estimates. The data available to avalanche forecasters can be categorized by entropy, following LaChapelle (1985). Figure 2.3 illustrates three data classes with entropy increasing with class number.

In addition to ranking the data based on ease of interpretation, the data is weighted differently if the information points towards snowpack stability or instability. One sample indicating instability can outweigh an entire series of data indicating stable conditions. Therefore, avalanche occurrences or other obvious signs of instability are considered more important for (in)stability estimates than the lack of such observations (McClung, 2002b).

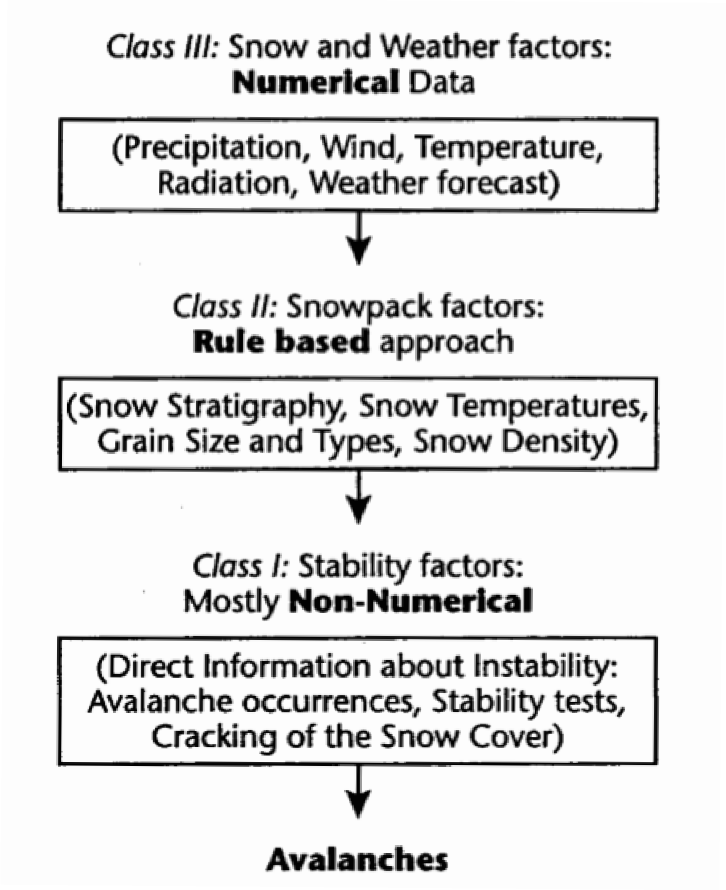

Figure 2.3: Information classes ranking data available when interpreting instability. Decreasing entropy along the arrows. Retrieved from (McClung, 2002b).

2.3 Avalanche detection by spaceborne radars

Knowing when and where avalanches have occurred is very important due to the low information entropy of these observations, and the emphasis placed on instability information in general. Avalanche activity monitoring have traditionally been based on field observations (Schweizer et al., 2003b). Bad weather, absence of daylight, remote locations and prevailing avalanche danger are some of the factors that can complicate data collection in the field.

Large amounts of avalanche activity data, with few temporal and spatial gaps are required to perform statistically meaningful data analysis and risk calculations for an entire forecasting region (Eckerstorfer et al., 2016). Furthermore, such complete spatio-temporal avalanche activity records of an entire winter are not achievable using field-based methods alone (Wesselink et al., 2017). Remote sensing can be a more reasonable approach, as demonstrated by Eckerstorfer et al. (2017) who presented a winter-long daily avalanche activity record of a forecasting region using satellite borne synthetic aperture radar (SAR) data from Sentinel-1.

Avalanche detection can be done using a number of different remote sensors. The extent to which each of the remote sensors can contribute to avalanche activity mapping was summarized by Eckerstorfer et al. (2016). Optical- and radar satellite data are the preferred technologies for monitoring avalanche activity on a regional scale (Eckerstorfer et al., 2019). The remote sensing data applied in this thesis is based on spaceborne SAR. This is therefore the technology that will be focused on from now on.

Radar systems use active sensors that transmit coherent microwave radiation pulses and measure the strength and phase of the signal backscattered to the sensor (Liu and Wu, 2001). In a radar image, the brightness of a target is determined by its radar cross section, defined as the ratio of energy received by the sensor over the energy that would be received from a target scattering the incident energy isotropically (Elachi and Van Zyl, 2006). The normalized radar cross section, typically denoted σ_0, is the radar cross section averaged over a resolution cell. The SAR technique is based on using a moving platform, such as an airplane or a satellite to enable a small antenna to record radar echoes over a large distance and through data processing replicate the aperture of a much larger antenna (Vu et al., 2013).

The backscattered signal from snow can be modeled as the sum of the contributions from the air-snow and snow-ground interfaces in addition to the volume scattering within the snowpack (Figure 2.4) (Eckerstorfer et al., 2016). Compared to the relatively smooth, undisturbed surface of the surrounding snow, avalanche debris is rough and therefore detectable in radar images due to the increased backscatter. Ulaby et al. (1986) described how the physical properties of snow largely influences the backscattered signal. While backscatter from dry snow is mostly dependent on snow density, wet snow scatters according to the content of liquid water (Hallikainen et al., 1986).

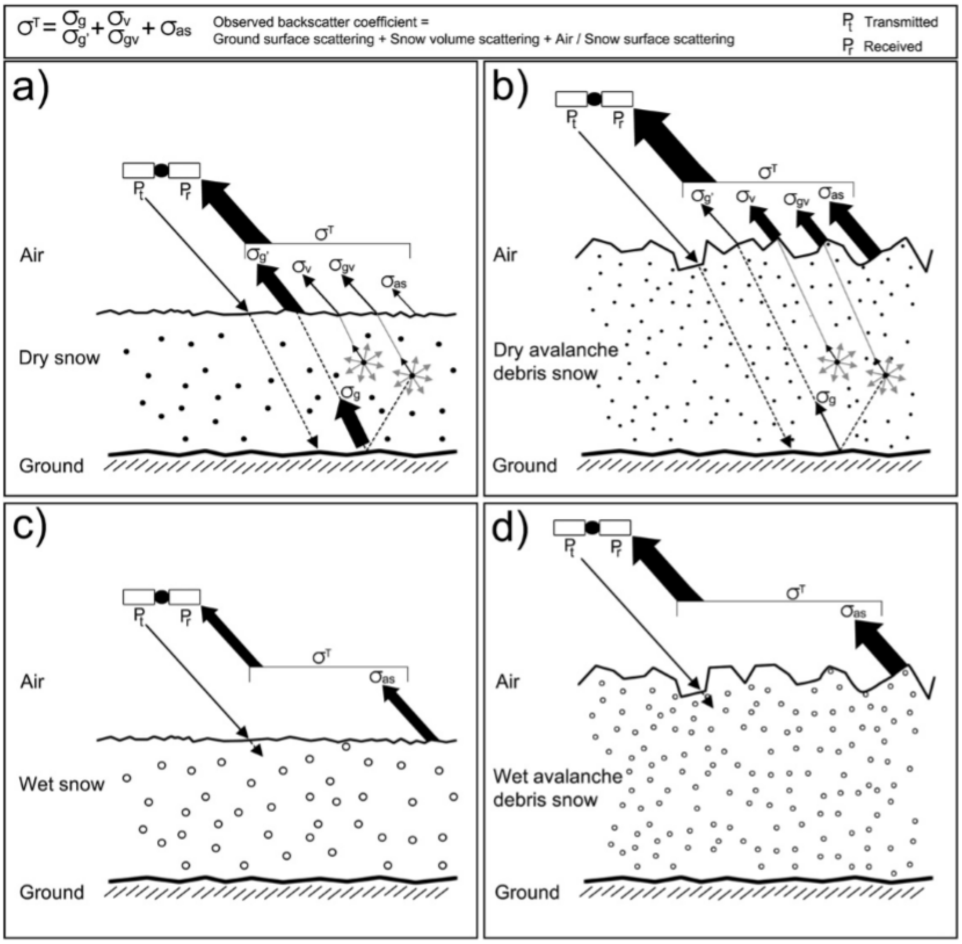

Figure 2.4: Schematic models illustrating both origin and strength of the contributions to observed backscatter from a) dry snow b) dry avalanche debris c) wet snow and d) wet avalanche debris snow. Retrieved from Eckerstorfer and Malnes (2015)

The potential for avalanche detection using spaceborne SAR was shown nearly two decades ago by Wiesmann et al. (2001) using data from ERS 1/2. More recently, avalanche debris was detected using C-band data from Radarsat-2 (Malnes et al., 2013; Eckerstorfer and Malnes, 2015) and X-band data from TerraSAR-X (Bühler et al., 2014). The European Space Agency (ESA) have provided freely available C-band SAR data from the Sentinel 1A and 1B satellites since they became operational in 2014 and 2016, respectively (ESA, 2020). Malnes et al. (2015) became the first to present avalanche detections in Sentinel images by applying data from Sentinel 1A in the interferometric wide swath mode (IW), with 20 x 20 m spatial resolution and 250 x 150 km swath.

Data from Sentinel 1A was also used when Eckerstorfer et al. (2017) presented a complete avalanche activity record from the forecasting region Tamokdalen for the 2014 - 2016 period. The authors detected avalanches manually by comparing *activity images* to earlier images with the same geometry, *reference images*. Due to the lack of ground-truth data, Radarsat-2 Ultrafine images of superior spatial resolution (3 x 3 m) were used to validate the detections.

Manual detection is both time consuming and prone to human bias, which is why automatic detection algorithms are necessary for building a substantial database of avalanche activity (Vickers et al., 2016). The first automatic avalanche detection scheme applied to Sentinel-1 data was presented by Vickers et al. (2016), who were able to automatically detect avalanche debris through change in radar backscatter and K-means unsupervised object classification. A revised algorithm by Vickers et al. (2017) allowed for different backscatter thresholds depending on the snow conditions. This approach proved beneficial when dealing with varied meteorological conditions within large images or between image pairs. The near-real-time avalanche monitoring system presented by Eckerstorfer et al. (2019) is based on a further development of the aforementioned algorithm, and will be described in section 3.1.

3

Data

In this chapter the two data sources applied in this thesis are presented in separate sections.

3.1 The Satskred dataset of avalanche detections

The dataset provided by NORCE is the combined output from running their automatic avalanche detection algorithm on the available data from 1 December 2014 to 31 May 2019. The same data was described in detail in Eckerstorfer et al. (2019), where the authors presented the first dataset of spatio-temporal avalanche activity over several winters from a large region. This section will summarize the characteristics of the dataset and briefly present the workflow of the detection algorithm producing the detections. Features detected by the automatic avalanche detection algorithm will from here on be referred to as *avalanche detections* or simply *detections*.

3.1.1 Study area

The study area where the detection algorithm was applied is defined using a 120 km x 86 km bounding box. The area is roughly centered around the town of Tromsø in Northern Norway. Even though the regObs database spans all of Norway, the study area of the detection algorithm determines where observations and detections can be compared, as no detections outside the study area are included in the dataset. This area is therefore the area of interest (AOI) used throughout the thesis. Figure 3.1 illustrates the AOI along with the masks applied to define where the algorithm should search for avalanche detections. The runout mask defines where avalanche debris can be detected, and comprises all possible runout zones. Furthermore, water-, agriculture-glacier- and forest masks were used to reduce the search area and to avoid false detections from these areas (Figure 3.1).

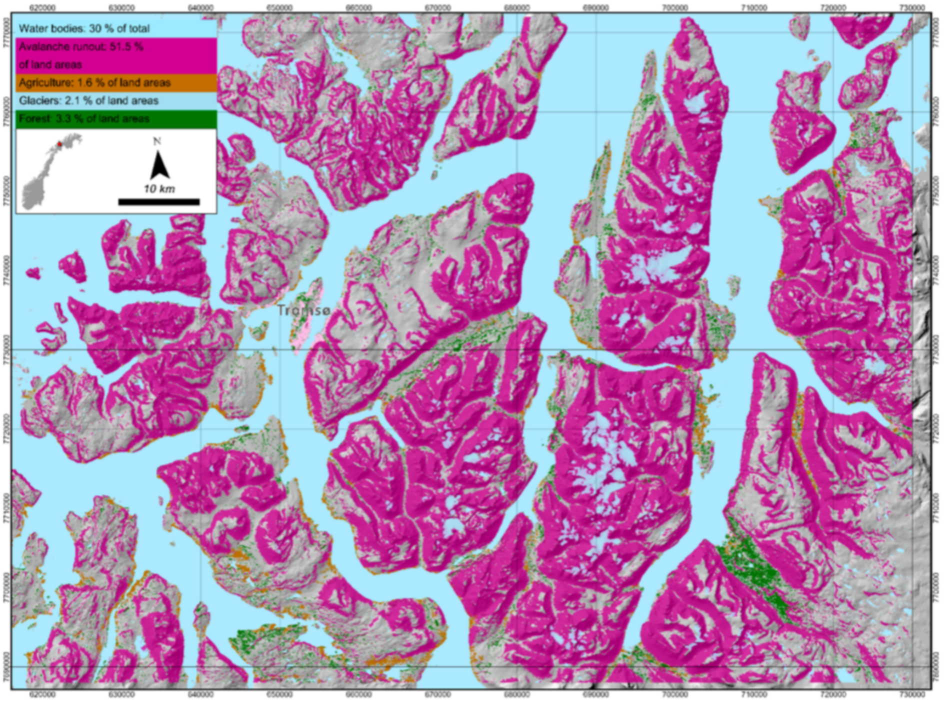

Figure 3.1: The area of interest with avalanche runout mask, water bodies, agricultural and forested areas superimposed onto a hillshade map. Modified from Eckerstorfer et al. (2019)

3.1.2 Sentinel 1 availability and spatial coverage

Eckerstorfer et al. (2019) downloaded Sentinel-1 data in the period of 1 December to 31 May each winter, which is the avalanche forecasting season in Norway. The data was ground range detected (GRD) in IW mode for both VV (vertical transmit and receive) and VH (vertical transmit, horizontal receive) polarizations. The ground range pixel resolution was 20 m.

Images of both ascending and descending orbits were used. During the study period there was a trend towards increased amount of data available from ESA and three new swaths became available. From the 2016 - 2017 season onward, four satellite swaths were available for the ascending orbits, while six swaths were available for the descending geometry.

The Sentinel satellites (S1A and S1B) are identical and together they make the repeat cycle of each swath six days (ESA, 2020). Due to the high latitude of the study area, combined with the polar orbits of the satellites, the study area is covered daily. On average during the 2017 - 2018 season, 7.3 Sentinel images covered the avalanche runout area illustrated in Figure 3.1 within the six days repeat cycle (Eckerstorfer et al., 2019).

3.1.3 Detection algorithm workflow

The workflow of the avalanche detection algorithm is illustrated in Figure 3.2. Each of the steps will be briefly presented in this subsection.

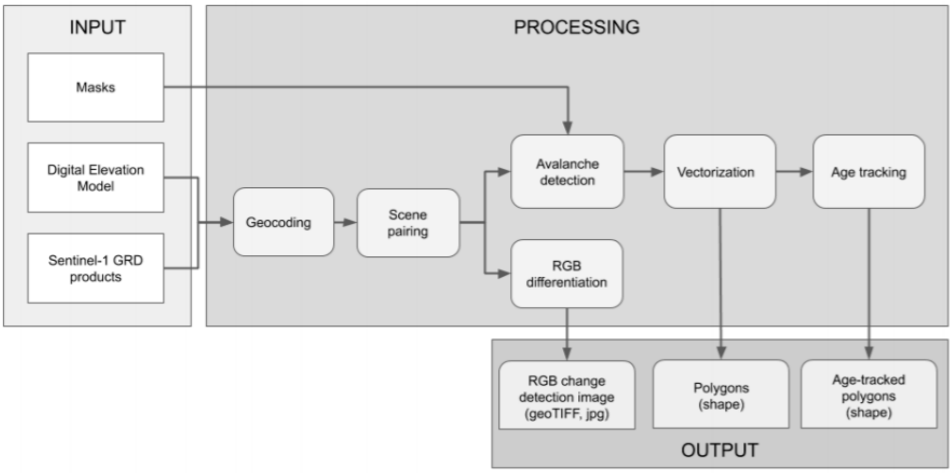

Figure 3.2: Workflow of the Satskred automatic avalanche detection algorithm. Retrieved from Eckerstorfer et al. (2019)

The first processing step of the detection algorithm involves geocoding of the Sentinel images using a Digital Elevation Model (DEM). The geocoded images are then paired into reference image and activity images of similar geometry and orbit that are separated in time by one repeat cycle. The scene pairing outputs difference images, showing relative change in backscatter from the preceding image (reference) to the current image (activity). The RGB differentiation step consists of making a pseudo-color image by displaying the reference image in the red and blue channel, while the activity image is displayed in the green channel. These RGB images can be used for manual avalanche detection, as avalanche debris appears green due to the positive backscatter change (Eckerstorfer et al., 2019).

The automatic avalanche detection step applies the difference images from the scene pairing together with the input masks (Figure 3.2). Avalanche detection is carried out separately by two approaches: Difference of Gaussians (DoG) filtering and Segmentation. The results are combined to form a binary map of pixels classified into either *avalanche* or *not avalanche*. If an area classified as *avalanche* spans less than 10 pixels, or more than 390 pixels, it is considered noise and therefore disregarded (Eckerstorfer et al., 2019).

The final step involves vectorizing the binary avalanche detection map into polygons by tracing the outline of each detected feature. The metadata added to the detection polygons is listed in subsection 3.1.5.

3.1.4 Age tracking

The total number of avalanche detections in the full 2014 - 2019 dataset is 44048. As some avalanches were detected in multiple subsequent Sentinel images, the set contains numerous detections representing the same avalanches. Eckerstorfer et al. (2019) developed an age tracking algorithm to identify these detections by assuming that features from different geometries overlapping in space and time are likely to be the same avalanche.

The age tracked dataset for the 2014 - 2019 period consists of 31863 detections. The age tracking algorithm did not output a sufficiently reliable classification at the start of this project. Therefore, the data used in the thesis is the full set of 44048 detections. The age tracked data is applied once for comparison purposes, in Figure 5.5.

3.1.5 Data format and available metadata

The avalanche detection dataset was made available in a shapefile format. In addition to the polygon geometries, the shapefile included the metadata described in Table 3.1.

Table 3.1: Explanation of the metadata attributes of the avalanche detection polygons.

Attribute	Explanation
OBJECTID	Unique ID number
area	Area of the polygon in m^2
east	Longitude of polygon centroid
north	Latitude of polygon centroid
length	Maximum length of polygon
raster_val	Number of detected pixels
sat_geom	Satellite track number
t_0	Timestamp of reference image
t_1	Timestamp of activity image
dem_mean	Mean elevation of entire polygon
dem_median	Median elevation of entire polygon
dem_min	Minimum elevation of entire polygon
dem_max	Maximum elevation of entire polygon
slp_mean	Mean slope angle of entire polygon
slp_min	Minimum slope angle of entire polygon
slp_max	Maximum slope angle of entire polygon
vv0_max / min ...	Backscatter parameters

The mean, median, min and max value of the reference- and activity-image producing the detection were available for both polarizations (VV and VH) as well.

3.1.6 Detection algorithm performance

The Sentinel images' spatial resolution of 20 m allows for detection of avalanches with typical path lengths of around 100 m. This corresponds to roughly size 2 - *Medium* in Table 2.1. Even so, larger avalanches with thin, elongated shapes could still be difficult to detect. By comparing the automatic avalanche detections to a set of 243 field-observed avalanches, Eckerstorfer et al. (2019) found that the probability of detection (POD) was 57%. When comparing to avalanches that were manually detectable in the difference images instead, the resulting POD was 73%.

The detection performance was found to be dependent on changing snow conditions between the reference and activity images. A transition from dry to wet snow, associated with a net decrease in backscatter, is favorable. On the contrary, a wet to dry transition is associated with a high false alarm rate due to a net increase in backscatter. According to Eckerstorfer et al. (2019), the latter case is not typically associated with widespread avalanche activity as the snowpack dries up and stabilizes. Therefore, these days with high false alarm rates was deleted manually.

3.2 The regObs database

regObs (short for registration of observations) is a Norwegian public registry for snow, weather, flood and ice observations. The system is developed and operated by the Norwegian Water Resources and Energy Directorate (NVE) and Norwegian Public Roads Administration (SVV). regObs consists of a database with an Application Programming Interface (API) at www.api.nve.no, a web site (www.regobs.no) and a mobile app. The national website for warning of avalanche, flood, ice and landslide hazards is varsom.no and the regObs system is a part of the Varsom portfolio (Engeset et al., 2018)

regObs encourages everyone to contribute with their observations related to natural hazards. An *observation* in the regObs context is a collection of data submitted by a user through the app or website. Submitted observations are time-stamped, geographically positioned and immediately available for other platform users. The data in regObs is presented *as is* and NVE does not guarantee for information quality or actuality. It is important to recognize that submitted observations may be erroneous or incomplete (regObs, 2020).

Data access

Observations can be viewed in the app or website. For other purposes, the data can be accessed using the API (api.nve.no) by posting date queries with a specified time period to the URL. The data in the regObs database is open and licensed according to Norwegian Licence for Public Data (NLOD).

The regObs data applied in this thesis was accessed through the API by the comparison algorithm at runtime. The dates limiting the query was set equal to the dates defining the Satskred detection season (1 December - 31 May).

Observer competence

Users have to create an account to be able to upload observations using the web site or mobile app. The user is assigned a competence level by regObs ranging from one to five stars. Users without stars are considered to have low or unknown competence. The requirements for obtaining more stars vary slightly between the natural hazard categories, but for snow observations the competence levels are defined as described in Table 3.2 (Varsom, 2020a):

Table 3.2: Descriptions of the different regObs observer competence levels.

Competence	Description
-	Unknown competence
*	The observer knows the basics of assessing avalanche danger, but is not educated in how regObs and Varsom communicate avalanche danger.
**	The observer is experienced in assessing avalanche danger, but not educated in how regObs and Varsom communicate avalanche danger.
***	The observer is educated and has advanced skills in assessing avalanche danger. The observer has a basic course in how regObs and Varsom communicates avalanche danger.
****	The observer is educated and has advanced skills in assessing avalanche danger. The observer has an extended course in how regObs and Varsom communicates avalanche danger.
*****	The observer is an avalanche forecaster.

3.2.1 Snow related observations in general

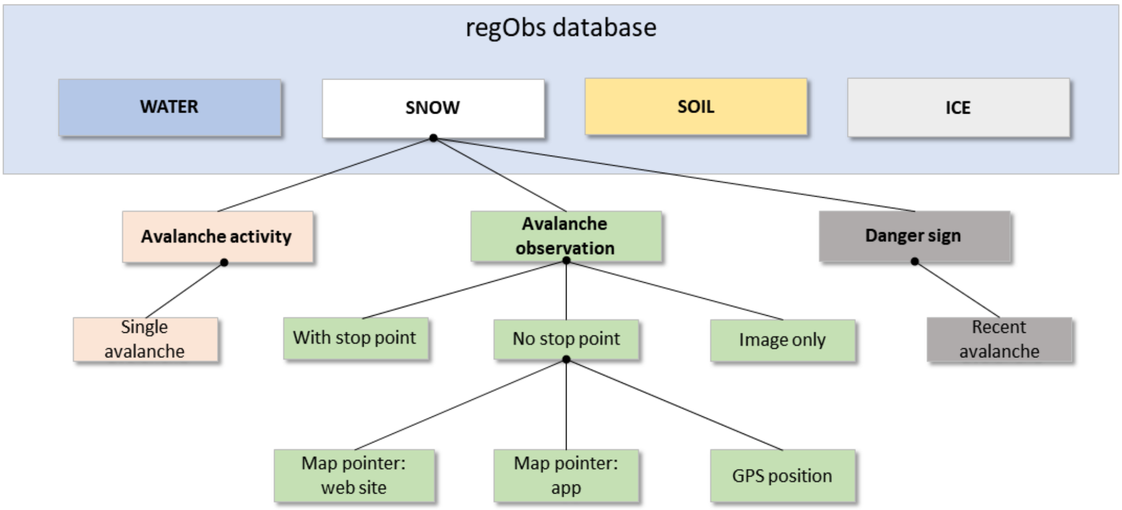

Figure 3.3: Overview of the regObs database categories. The flow chart focuses on the snow related observation data that potentially could be compared to Satskred detections.

The regObs database comprises four main observation categories, as illustrated by Figure 3.3. Every observation contains information on the registration time and location, as well as observer account information. The attributes shared by all regobs entries are listed in Table 3.3

The different observation types within the snow related category are listed in Table 3.4. In order to register a snow related observation, at least one of the observation types from Table 3.4 must be entered (regObs, 2020).

Table 3.3: Descriptions of the attributes shared by all regObs entries. The attribute names correspond to the names returned from the API.

Attribute	**Description**
GeoHazardName	Which geohazard the observation is related to
RegID	Unique ID number of the registration
DtObsTime	Date and time of the observation out in the field
DtRegTime	Date and time when the observation was registered to regObs
DtChangeTime	Only given if the registration has been changed
NickName	Nickname chosen when creating the account
CompetenceLevelName	Competence level associated with the account
UTMEast	East UTM coordinate of the registration
UTMNorth	North UTM coordinate of registration
UTMZone	UTM zone of the registration
Latitude	Latitude of the registration
Longitude	Longitude of the registration
ForecastRegionName	Forecast region
MunicipalName	Municipality
UTMSource	The way the observer registered the location
Uncertainty	Estimated positional uncertainty

Table 3.4: Snow observation types. The observation types illustrated in Figure 3.3 are set to italics. These are the observation types that are potentially useful for comparison to avalanche detections.

Category	**Observation type**
Snow	*Danger sign* *Avalanche observation* *Avalanche activity* Weather Snow cover Column test Snow profile Avalanche problem Avalanche danger assessment Accident/incident Notes

In addition to the general public and professional observers, some of the regObs entries stem from avalanche detections by ground based radars and infrasound avalanche detection systems. In February 2017, a ground based avalanche detection radar was installed to monitor Holmbuktura in Tromsø Municipality (Meier, 2018). The radar was able to detect avalanches through the doppler shifted frequencies of the signal backscattered from the moving snow. During the 2014 - 2019 period, 27 regObs entries of the *avalanche observation* type was based on detections from this radar system.

In Lavangsdalen, an infrasound avalanche detection system is installed. The system detects avalanches with a 360° field of view through their sound signature in the < 20 Hz frequencies (Wyssen, 2019). During the 2014 - 2019 period, 8 regObs entries of the *avalanche observation* type was based on detections from this infrasound system.

Each of the three snow observation types considered potentially useful for comparing to Satskred avalanche detections are presented in subsections 3.2.2, 3.2.3 and 3.2.4.

3.2.2 Avalanche observation

Avalanche observation type entries describe a single event. These observations are also referred to as *avalanche incident* (*Skredhendelse* in the Norwegian version) on the regObs web site. In this thesis the main focus is placed on this observation type. Therefore, *avalanche observation* and *observation* will be used interchangeably. When referring to the observation types *avalanche activity* and *danger sign*, this will be specified.

Within the Satskred AOI, 629 avalanche observations were registered during the five seasons 2014 - 2019. The information attached to the avalanche observations is listed in Table 3.5.

Table 3.5: Description of the attributes of the avalanche observation type regObs entries. Attribute names correspond to names returned from the API.

Attribute	**Description**
AvalancheName	Type of avalanche
AvalancheTriggerName	Trigger mechanism
WeakLayerName	Weak layer
FractureHeight	Height of the crown
FractureWidt	Width of the crown
DestructiveSizeName	Avalanche size
DtAvalancheTime	Estimated release time
HeightStartZone	Height (m.a.s.l) of the start zone
HeightStopZone	Height (m.a.s.l) of the stop zone
SnowLine	Snowline height (m.a.s.l)
TerrainStartZoneName	Terrain in the start zone
Trajectory	Name of the avalanche path
Aspect	Slope aspect
UTMEastStop	East UTM coordinate of stop point
UTMNorthStop	North UTM coordinate of stop point
UTMZoneStop	UTM zone of stop point
StartPoint	Latitude and longitude of the start point
StopPoint	Latitude and longitude of the stop point
Comment	Free-text description

All of the attributes are optional for the observer to enter, except the DtAvalancheTime, which must be specified. The avalanche observations could be categorized into three subcategories based on the stop point information: those with a reported stop point, those without reported stop point and the image-only registrations. The distribution of observations between these subcategories is illustrated in Figure 3.4. Image-only observations contain all of the information from Table 3.3, while none of the attributes from Table 3.5 are given.

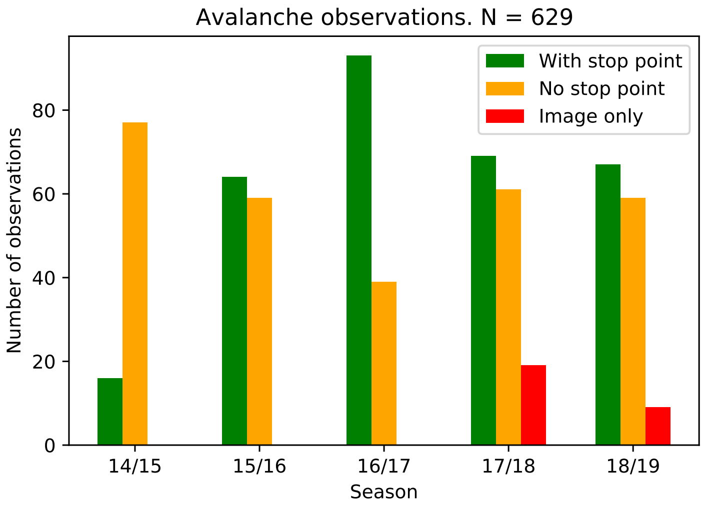

Figure 3.4: Number of avalanche observations sorted by subcategory and season.

The Uncertainty attribute from Table 3.3 is plotted by UTMSource for the avalanche observations without stop point in Figure 3.5. These uncertainty estimates are used in Section 5.1.2, where a method for handling observations without stop point is proposed.

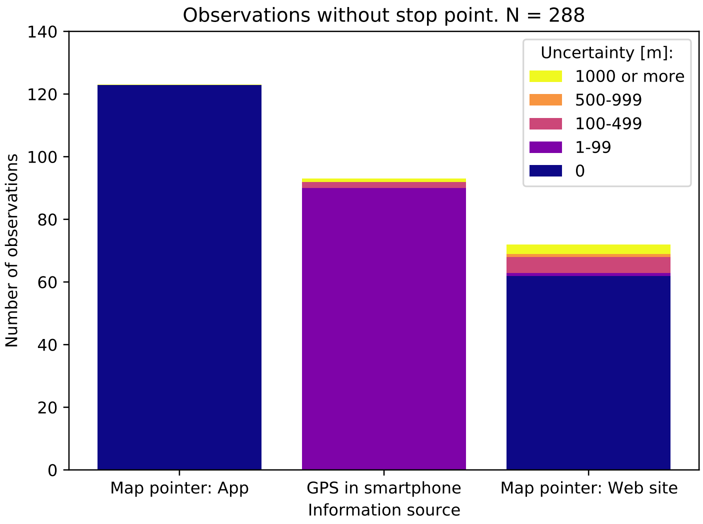

Figure 3.5: Uncertainty values plotted by UTMSource for observations without stop point within the AOI from 2014 - 2019.

3.2.3 Avalanche activity

The *avalanche activity* category of regObs entries can be used to report multiple avalanches, single avalanches and no avalanche activity. Figure 3.6 illustrates the distribution of the estimated number of avalanches reported using this category. The avalanche activity entries of single avalanches are expected to be most applicable for comparison to avalanche detections.

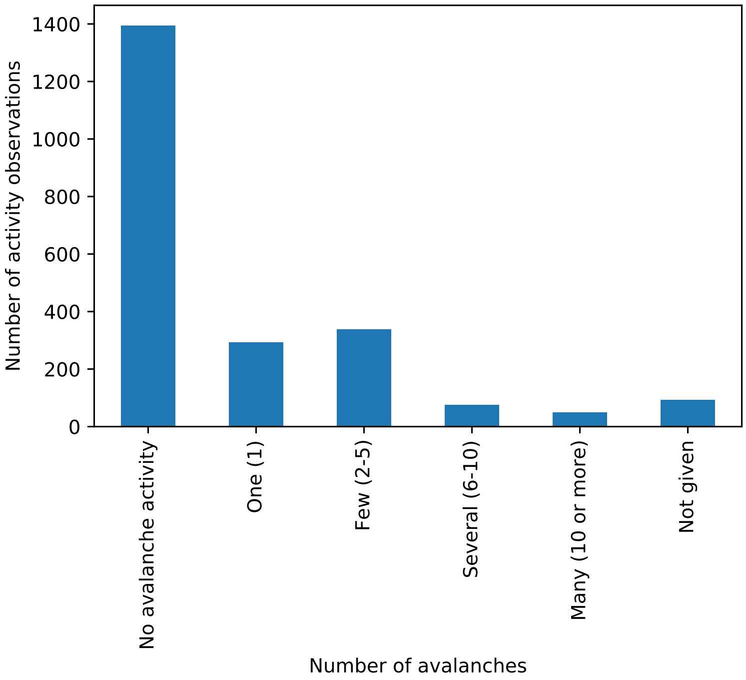

Figure 3.6: Avalanche activity estimated numbers in the Satskred AOI from 2014 - 2019 (N=2245).

3.2.4 Danger sign

The *danger sign* category of regObs entries can be used to report any observed danger sign pointing towards current or future snowpack instability, or the lack of such danger signs. Figure 3.7 illustrates the distribution of the different danger sign types reported. The *recent avalanche* type danger sign entries are expected to be most applicable for comparison to avalanche detections.

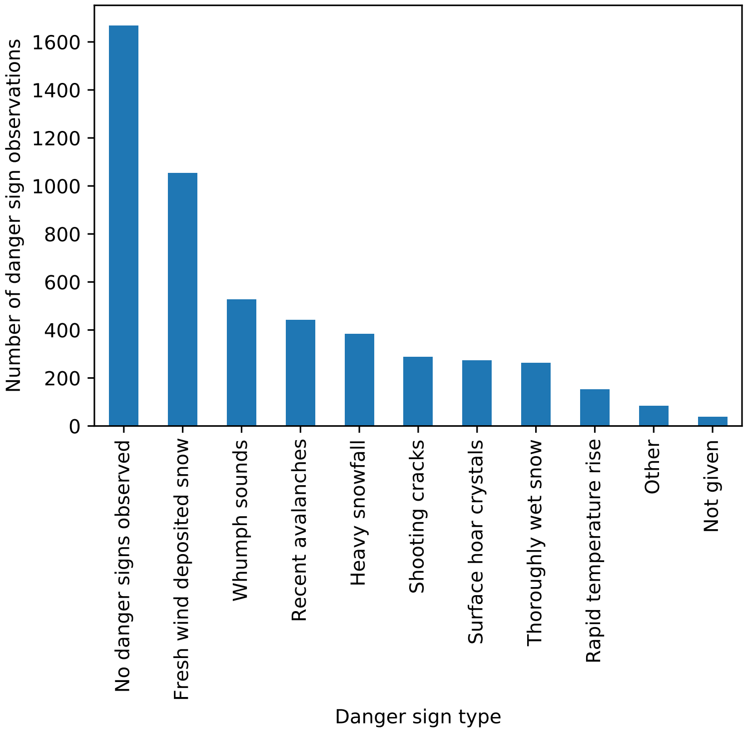

Figure 3.7: Danger sign types reported within the Satskred AOIfrom 2014 - 2019 (N=5181).

4

Methods

This chapter comprises two sections, where the first presents the necessary algorithm input and the second explains the algorithm workflow in a step-wise manner and how the input is handled. In order to visualize both the input and the steps of the algorithm, an example area roughly in the middle of the AOI was chosen. The example area is centered over Ramfjord in Tromsø municipality (Figure 4.1). Note that all algorithm steps presented in this chapter are performed on the complete AOI and the purpose of the example area is simply to present a zoomed-in visualization.

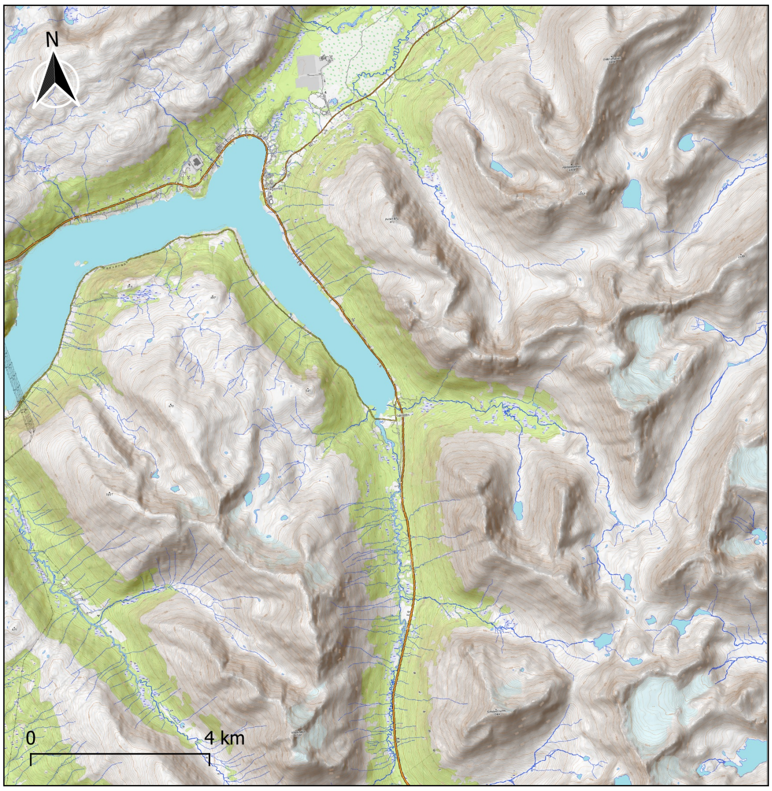

Figure 4.1: The example area used for visualization of algorithm input and workflow.

4.1 Comparison algorithm input and dependencies

Each input will be briefly explained with emphasis on their format and creation, while the way the input is put to use is handled in section 4.2. An overview of the workflow of the comparison algorithm, including where the input files are applied is illustrated in Figure 4.5.

The input files were prepared separately from the algorithm and given as input to avoid re-computing them every time the algorithm ran. All files used as input to the algorithm were stored in the same folder.

4.1.1 Avalanche detections

The avalanche detection dataset was made available by NORCE in a shapefile format. The detection polygons were converted from a coordinate system based on latitude and longitude, to UTM zone 33 coordinates which was the projection used in the comparison algorithm. Subsets of avalanche detections corresponding to each season were also prepared to enable single-season algorithm runs.

4.1.2 Digital Elevation Model

A publicly available Digital Elevation Model (DEM) of 10 m resolution was used to produce several of the input raster files. The DEM itself is not imported to the comparison algorithm, but it made the computation of aspects, slope angles, drainage basins and minimum elevation points possible. The DEM was downloaded from hoydedata.no, the Norwegian Mapping Authorities' website. The accuracy was ±1 m in the areas covered by National Detailed Elevation model (NDH) and ±2-6 m in the areas not covered by NDH.

4.1.3 Minimum elevation points

The DEM was used to find the points of minimum elevation for each of the avalanche detection polygons. These points were stored as a separate shapefile and imported to the comparison algorithm. Computing the minimum elevation points in advance significantly reduces the algorithm runtime for large numbers of detections.

4.1.4 Drainage basins

Drainage basin and *watershed* can be used interchangeably when referring to an area of land that drains all the streams and rainfall to a common outlet (USGS, 2020). In this thesis, *drainage basin* means the land area, while *watershed* is the perimeter of the drainage basin and consequently the border between drainage basins.

Drainage basins were created and used to narrow down the areas when searching for avalanche detections. This approach was based on the idea that it would be highly unlikely that an avalanche detected in one drainage basin corresponded to an avalanche observed and reported in another. The watershed was used to represent the typical boundary for the terrain within line of sight of an observer.

The drainage basin map was made in QGIS using the Geographic Resources Analysis Suport System (GRASS) plugin tool r.watershed with the DEM as input. The minimum number of pixels of an exterior drainage basin is controlled by the threshold parameter, which was set to 60000. The convergence for multiple flow directions was set to 9 out of 10, meaning almost single flow direction. This produced the most pleasing results. The r.watershed tool produced some small unwanted sliver regions that were removed by vectorizing the raster and merging all polygons of areas less than 1 km^2 with the adjacent polygon with longest common border. In addition, some polygons larger than 1 km^2 were merged manually where the partitioning was not necessary. This was typically done in areas with low gradients and few strong terrain features such as sharp ridges. Finally the drainage basin polygons were rasterized into a 20x20 m grid with unique values for every polygon, as illustrated by Figure 4.2.

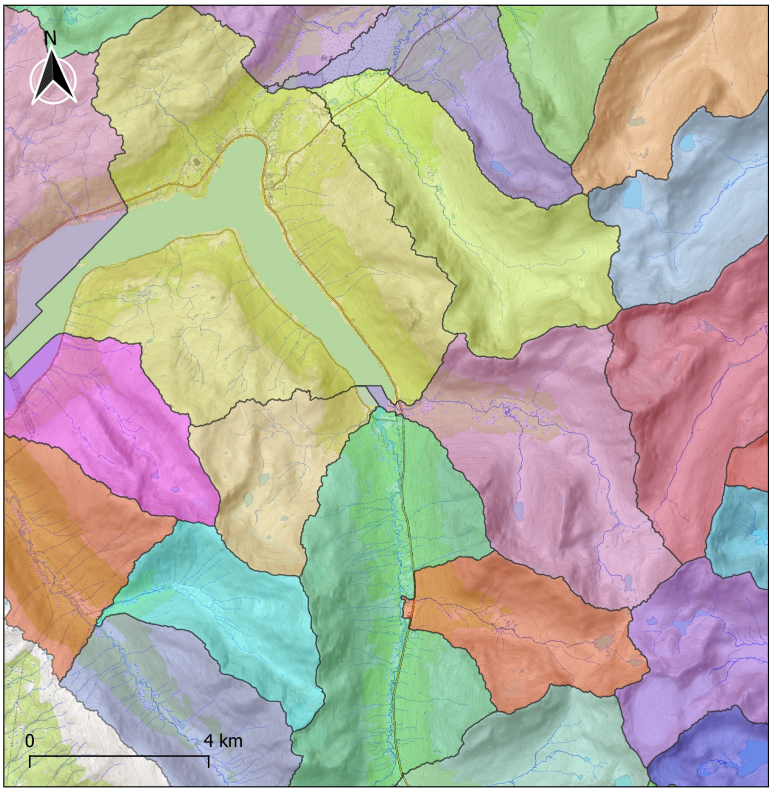

Figure 4.2: Drainage basins with unique raster values illustrated by random colors.

4.1.5 Aspect

The algorithm uses slope aspect as one of the similarity measures when comparing avalanche observations to the detections within the same drainage basin.

A 20 m resolution slope aspect raster was computed using the DEM and the QGIS GDAL plugin tool gdal:aspect with default parameters. The aspect is represented with azimuth degrees, where north is zero and then in clockwise ascending order: east(90), south(180), west(270). The aspect values are not categorized into the four cardinal directions, but kept as floating-point numbers. The aspect raster values are illustrated in Figure 4.3

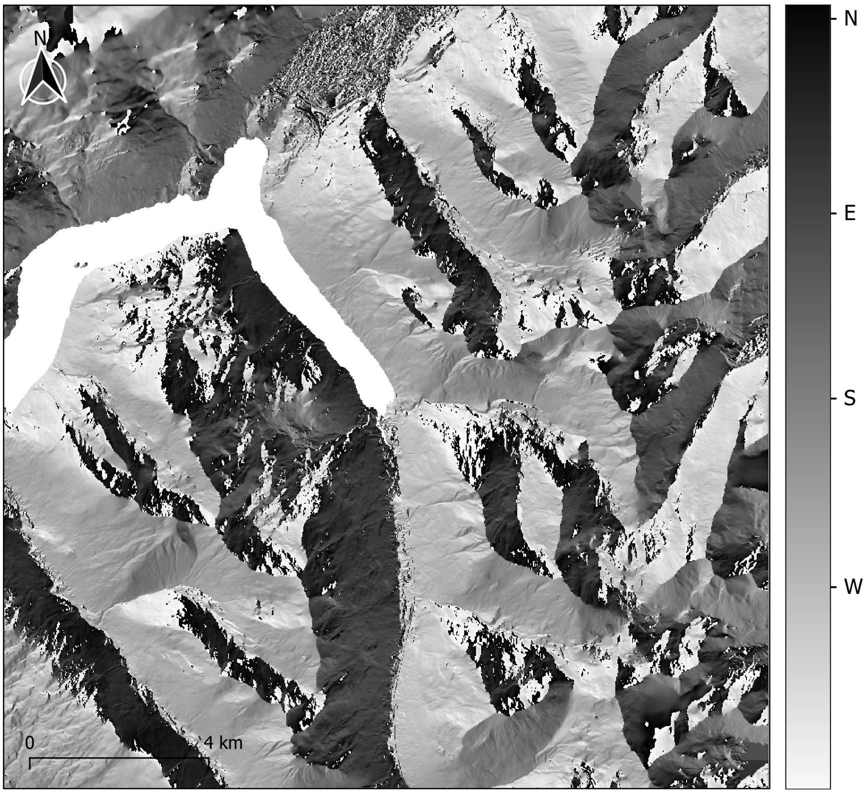

Figure 4.3: Grayscale representation of the aspect raster values. North is 0 degrees (dark), then ascending clockwise to 360 degrees (bright).

4.1.6 Slope angles

The slope aspect is not well-defined for flat ground, which is why the aspect value of the ocean in Figure 4.3 is white, i.e facing north. The algorithm handles this problem by applying a slope angle threshold to avoid assigning aspect values to near-flat ground.

Much like the aspect raster, a 20 m resolution slope raster was produced in QGIS (Figure 4.4).

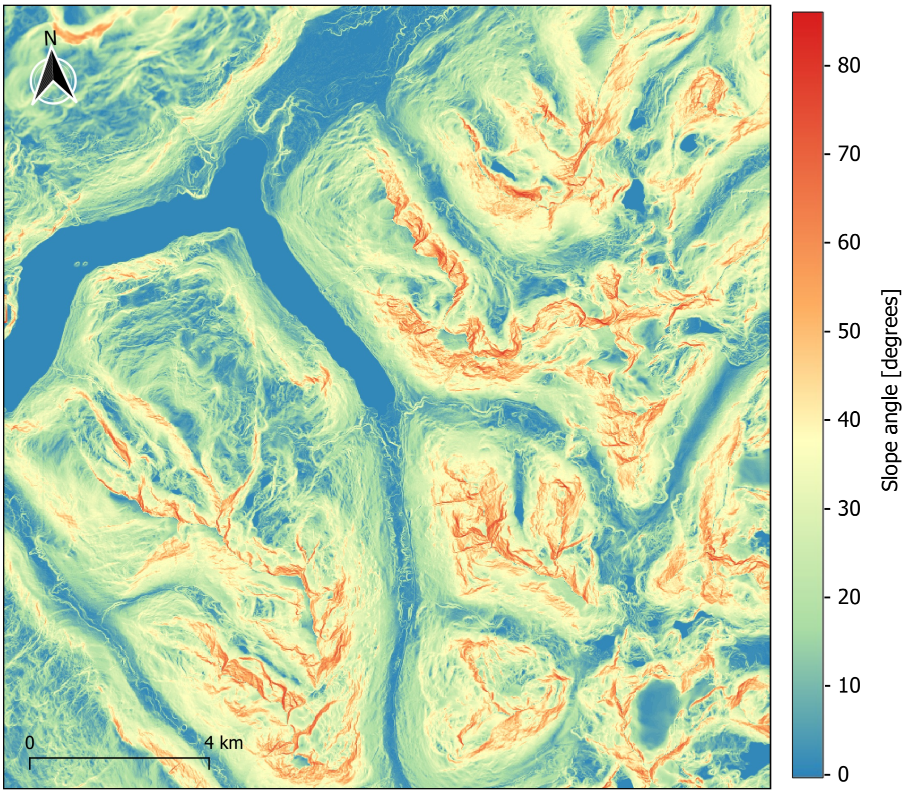

Figure 4.4: Color-coded slope angles for the example area.

4.1.7 Configuration file

All the parameters used by the comparison algorithm can be tuned in the configuration file. This file provides easy access to the parameters related to adjusting algorithm performance and output. Notable parameter categories stored in the configuration file includes: Times and regions limiting the regObs API query, shape parameters for the scoring functions and file-paths to the files required to run the algorithm (Table 4.1).

Table 4.1: The main content of the configuration file.

Parameter	**Description**
use_obstypes	Observation subcategory used (see Figure 3.4)
obsdate_from	Start date of the API query
obsdate_to	Stop date of the API query
AOIregions	The regions of the API query
stop_pt_sigma	Distance scoring function sigma
CCDF_threshold	Distance score significance level
aspect_time_threshold	Threshold for the aspect-time product
slope_threshold	Slope threshold in degrees
timeslack	Variable used when comparing timeframe
no_stp_spread	Distance sigma used without stop point
path_alg_dep	Path to the algorithm dependencies folder

4.2 Comparison algorithm workflow

This section presents the main components of the comparison algorithm in a step-by-step manner following Figure 4.5. The code for the comparison algorithm was written in Python 3 with an object oriented design. The entire algorithm is as an instance of a Python class called *Comparison_Algorithm*. The observations and detections were also handled in the algorithm as instances of the *Observation* and *Detection* classes.

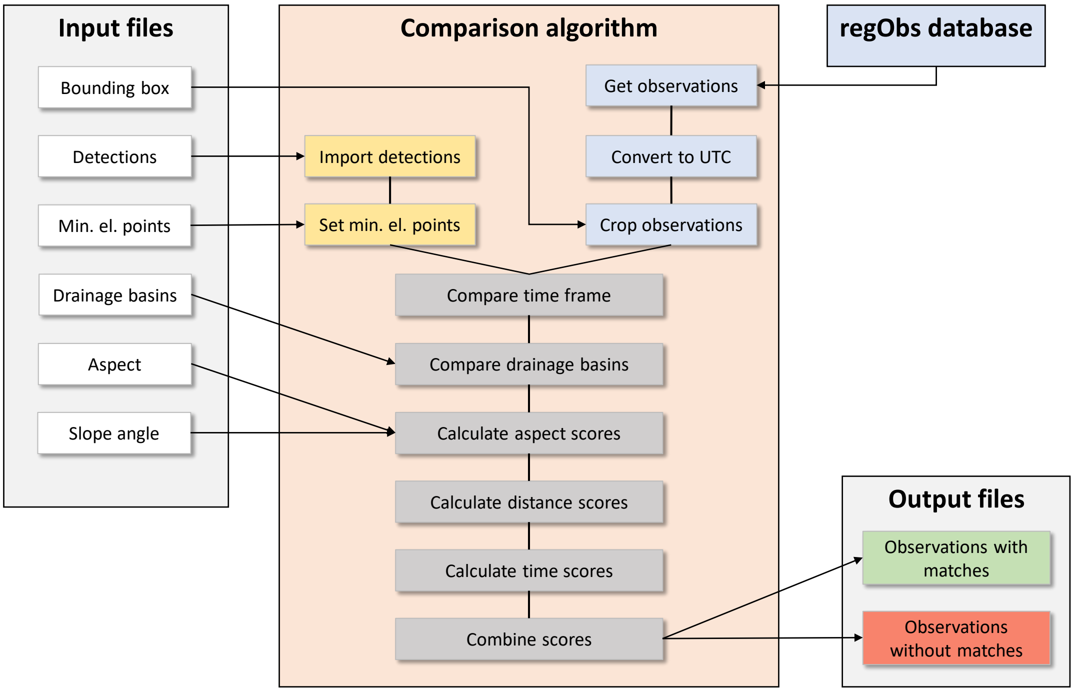

Figure 4.5: Workflow of the comparison algorithm.

4.2.1 Get observations

While the avalanche detections were stored locally, the avalanche observations from regObs were accessed using the regObs python API. The API returned observations matching the search criteria defined in the configuration file as a pandas DataFrame. Python code for accessing avalanche observations using the python API was provided by NVE and can be found at https://github.com/NVE/varsomdata. The get_avalanche method from getobservations.py was used.

The variables given to the API query were *from_date*, *to_date* and *region_ids* defining the temporal and spatial extent of the observations. Figure 4.6 illustrates the locations of avalanche observations from the example area within: *from_date*= '2018-12-01' , *to_date*= '2019-05-31'.

Some of the avalanche observation database entries had no information in the data-frame cells related to the avalanche observation form. This was found to coincide with database entries only containing an image. These image-only observations were filtered out, leaving only observations with non-empty avalanche observation information forms.

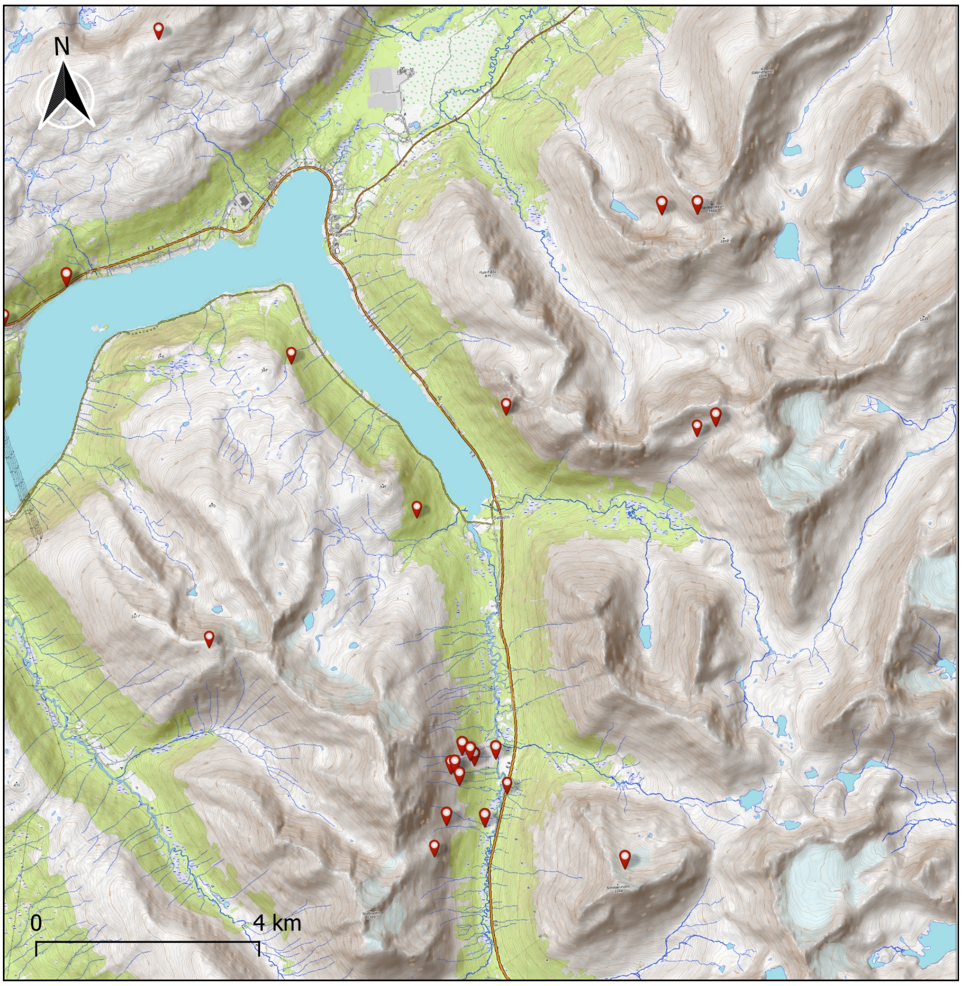

Figure 4.6: Avalanche observations from the 2018 - 2019 season represented by red markers.

If the API output was empty, the algorithm would inform about this and terminate.

4.2.2 Convert timestamps to UTC

The timestamps of the regObs observations are given in local time, while the avalanche detections have timestamps in Coordinated Universal Time (UTC). In order to compare times and produce timedelta objects, all timestamps must be converted to UTC. This way, ambiguities related to time zones and daylight savings time are avoided.

All timestamps referred to and presented in this thesis are UTC times.

4.2.3 Crop observations

The Satskred AOI intersects five of the avalanche forecast regions defined by NVE: Tromsø, Lyngen, Sør-Troms, Indre Troms and Nord-Troms (Varsom, 2020b). Large parts of the three latter regions fall outside the AOI, as illustrated in Figure 4.7. As the input raster layers and the detections are defined only within the AOI, all outside observations are disregarded at this step. Removing the observations outside the AOI ensures that the observations evaluated in the comparison algorithm are located where the avalanches could also be detected in the satellite images. Removing these observations at an early stage also gives a significant algorithm performance gain with regards to processing time.

Some observations are close to the AOI border and could potentially have been misplaced to a location inside the bounding box while the true avalanche location is outside, and therefore not detected by the avalanche detection algorithm. To avoid this issue, observations close to the border are also removed if the observation is closer to the border than its own distance cutoff radius (explained thoroughly in subsection 4.2.7). Because of the distance cutoff, observations further inside the border could not have been assigned matches from detections outside the AOI. Following this approach, one can be sure that no matches were missed due to observations close to the AOI border, at the expense of disregarding less than ten observations over the five seasons 2014 - 2019.

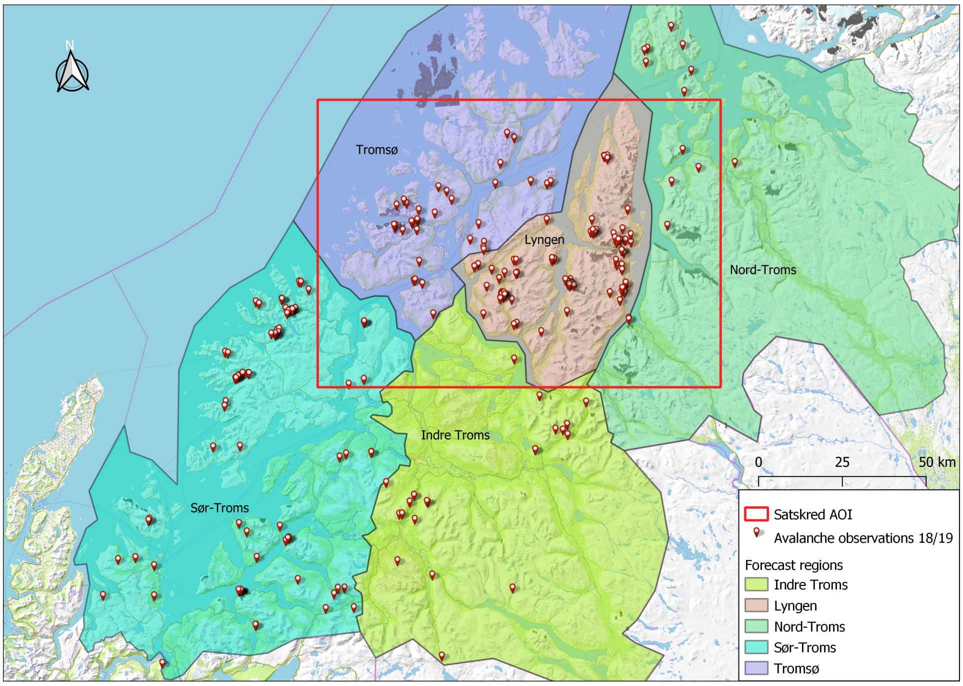

Figure 4.7: The Satskred AOI represented by a red rectangle. Forecast regions according to the NVE definition of December 2016. Avalanche observation locations from the 2018 - 2019 season represented by red markers.

4.2.4 Compare timeframe

The next step involves evaluating the observation time against the timeframe of the detections. The Satskred avalanche detections are change detections based on radar backscatter differences between a reference image taken at time t_0 and an activity image taken at time t_1. A detection represents an event, possibly an avalanche, occurring within this timeframe causing increased backscatter. Avalanche debris can be observed in the field several days after the avalanche event, depending on weather conditions. Therefore, a variable called *timeslack* was used to extend the timeframe by a few days and make possible evaluating field observations after time t_1.

The algorithm evaluates the timeframe of every Satskred detection against the observation time of every avalanche observation. To avoid computationally expensive looping operations, this is done by calculating timedeltas using numpy arrays and outer subtraction. Each observation object is assigned a list of detections with timeframes (+timeslack) that span the observation time. These detections are from now on referred to as "timematches". In the following algorithm steps when additional spatial filtering is done to find potential matches of an observation, only timematches are considered candidate detections.

The timeframe comparison significantly reduces the number of match candidates, which is evident from Figure 4.8 and Figure 4.9. The first illustrates the detections from the 2018 - 2019 season in the example area alongside with one of the avalanche observations from the same season. The latter illustrates the same area and observation, but only the timematching detections.

If no timematches have been found for any of the observations, the algorithm will inform about this and terminate.

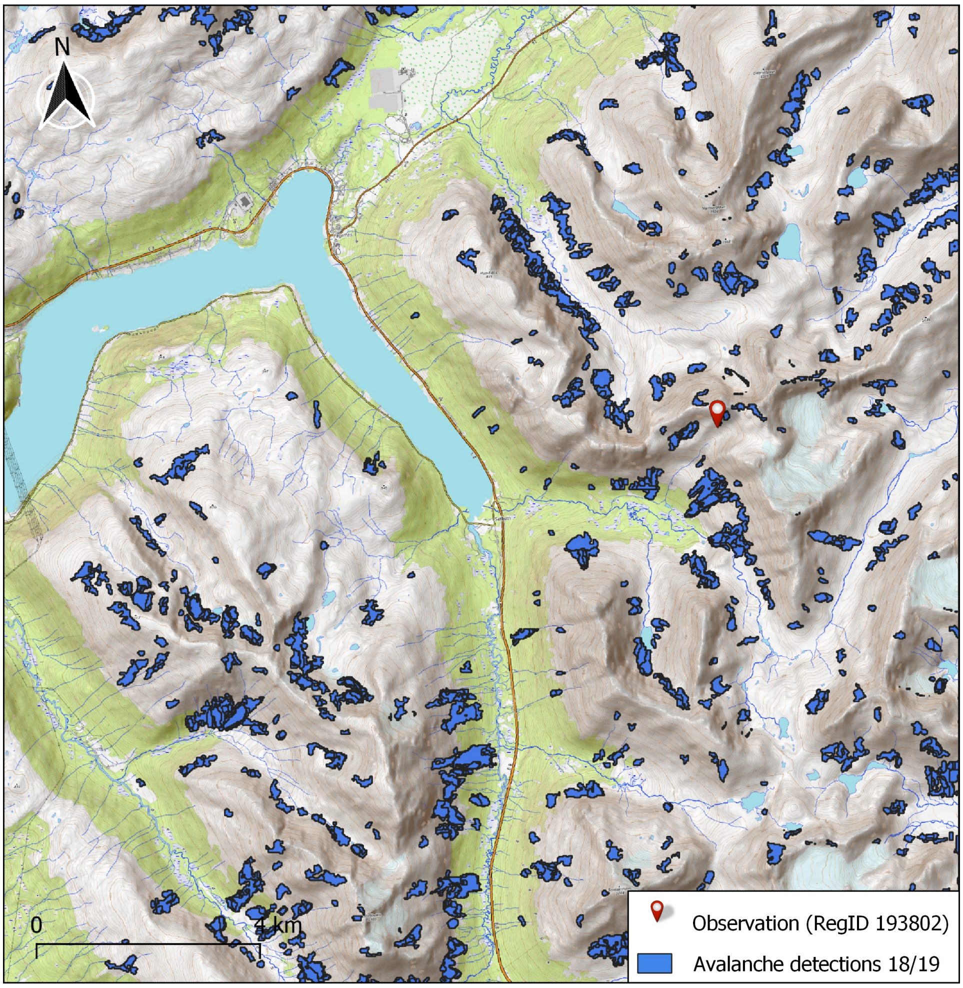

Figure 4.8: Avalanche detections from the 2018 - 2019 season illustrated by blue polygons. Observation location of RegID 193802 represented by red marker.

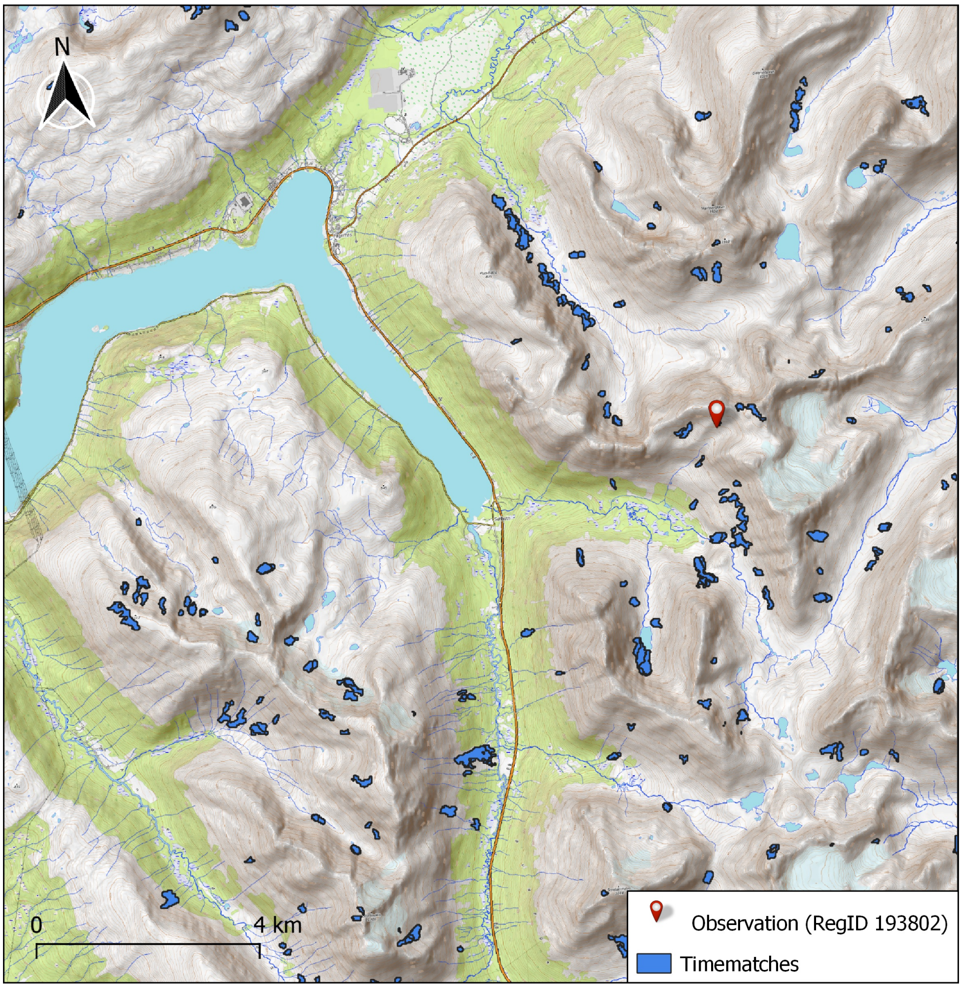

Figure 4.9: Observation location of RegID 193802 represented by red marker. Timematching detections calculated using a timeslack of five days represented by blue polygons.

4.2.5 Compare drainage basins

After temporal filtering, the observations and detections are assigned drainage basin memberships using the drainage basin raster input file. The drainage basins are not used in the classical water-science manner, but instead as a convenient way of dividing the AOI into sub-regions separated by ridges and other prominent terrain features. The purpose of using drainage basins is partly to perform a rough, initial spatial filtering and partly to avoid false matches from detections on the wrong side of a mountain or ridge. If only distance-based spatial filtering was performed, a number of detections could be considered matches even though they were separated from the observation by a ridge.

The drainage basin approach assumes that an observer being asked to point at a field event in the map unlikely misplaces the event to the wrong side of a mountain or ridge. The size of each drainage basin is large to ensure that the spatial filtering performed in this step is not removing any true matches.

Timematches that also belong to the same drainage basin as the observation are stored in another list of *time-DB-matches* (Figure 4.10). These detections have passed the initial filtering in time and space and will be the only ones evaluated in the following algorithm steps.

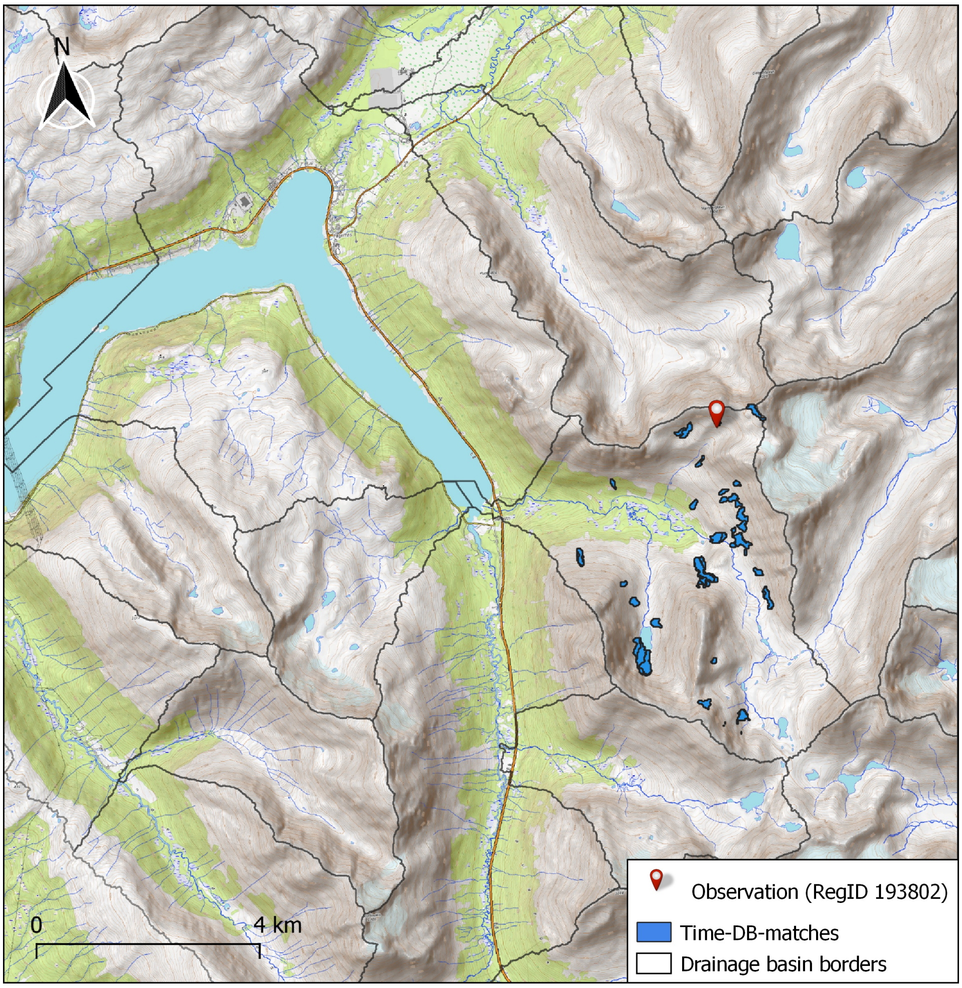

Figure 4.10: Observation location of RegID 193802 represented by red marker. Detections sharing drainage basin and timeframe with the observation as blue polygons. Timeslack: five days. Drainage basins illustrated by black lines along the watersheds.

4.2.6 Calculate aspect scores

Detections of similar aspect to the observation should be considered more likely to be a match than those with opposite aspect. Following this idea, a smooth cutoff function could be used to reduce the aspect score with increasing aspect difference. This approach also assumes that observers seldom misplace the avalanche location onto a slope with opposite aspect.

Using the aspect raster, aspects values are assigned to both observations and detections by sampling the raster at their locations. The aspect difference is then calculated as the least difference between two aspects when turning clockwise or counter-clockwise. Thereby, aspect differences take on values from 0 degrees (equal aspect) to 180 degrees (opposite aspect).

A smooth cutoff function is used to give the detections an aspect score based on the aspect difference. The cutoff function, otherwise referred to as the *bump function*, is defined using the following expression:

$$f(\text{diff}, \text{cutoff}) = \begin{cases} \exp\left(1 - \frac{1}{1-\left(\frac{\text{diff}}{\text{cutoff}}\right)^2}\right) & , \text{diff} \in [0, \text{cutoff}) \\ \\ 0 & \text{otherwise} \end{cases}$$

where *diff* is the aspect difference and *cutoff* determines where the bump function goes to zero. Figure 4.11 illustrates the properties of the bump function compared to a gaussian function of similar shape. The bump function has the desired properties of both maintaining a relatively high score for similar aspects and reducing the aspect score to zero for detections with opposite aspect. The cutoff was set at an arbitrary 160 degrees for visualization in Figure 4.11. The selection of parameter values, such as the aspect cutoff is presented in section 5.1.

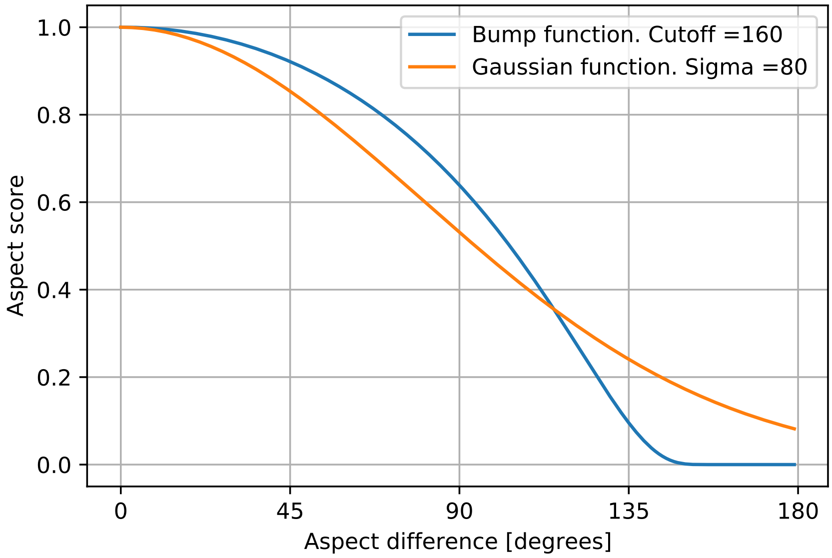

Figure 4.11: The blue line represents the bump function used for assigning aspect scores to detections. The gaussian function in orange is included only for reference as the comparison of the two highlights the desired cutoff properties of the bump function.

4.2.7 Calculate distance scores

Detections close to the observation location are intuitively considered more similar and more likely a match. The probability of the detection matching the avalanche described in the observation follows an unknown distribution of which distance is most likely one of the variables. Seeking the match probability and the associated distribution is difficult, as the true explanatory variables are mostly unknown and likely not independent. Using supervised machine learning methods to classify the detections as matches or no-matches is not an option without a dataset of confirmed matches and no-matches as training data.

In order to design a distance scoring function, the probability of an observation being placed a given distance away from the detection given that they are a match, can be used. There is no available dataset on the actual distance from the location stated in the observation entry to the true location of the avalanche. However, it is reasonable to assume that the easterly and northerly deviations from the true location are independent. The underlying causes for missing the mark when attempting to point at the map location of a field event is not known and can be numerous. In the absence of reasons suggesting otherwise, and for mathematical convenience, the deviations are assumed to be normally distributed around the aim point in each direction.

If the easterly- and northerly deviations (abbreviated : E, N) are assumed to be identically normally distributed, a two-dimensional distance vector of the two deviations would follow a circular bivariate normal distribution. The magnitude of this distance vector proves useful when building a distance scoring function. According to Ross (2004), the magnitude of the distance vector:

$$D = \sqrt{E^2 + N^2}$$

would then be chi-square distributed with 2 degrees of freedom, which is otherwise known as a Rayleigh distribution (Figure 4.12). The shape of the Rayleigh distribution is determined by its shape parameter, σ, which in general will be referred to as *sigma* from now on.

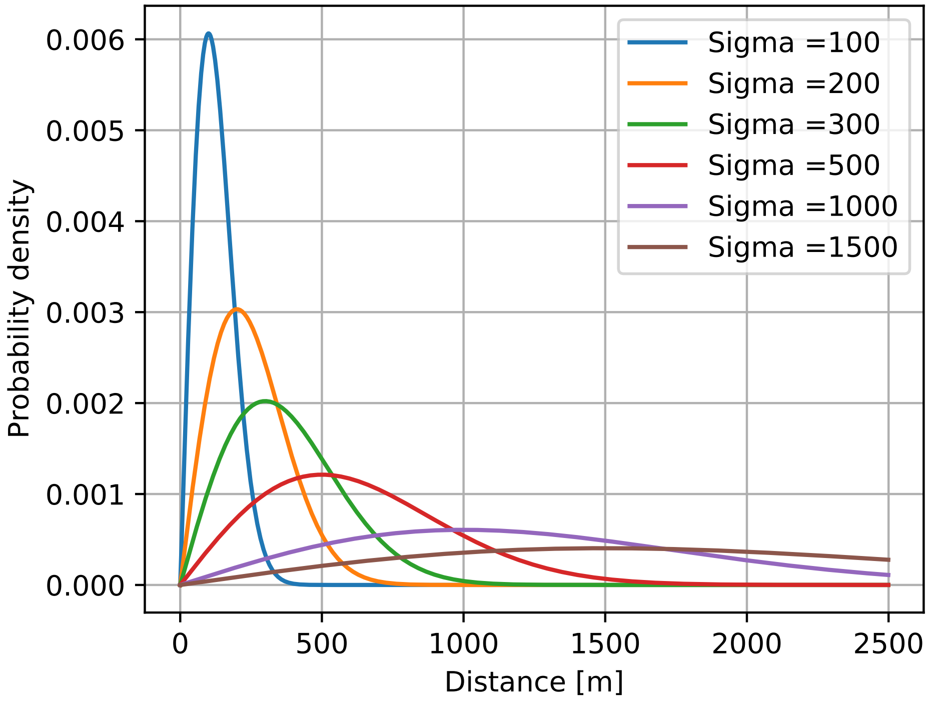

Figure 4.12: The probability density function of the Rayleigh distributed distance plotted for several values of sigma.

Unfortunately, as the easterly and northerly deviations were assumed to be normally distributed with an unknown spread, the sigma of the Rayleigh distribution is also unknown. The sigma value is set in section 5.1 by running the algorithm with multiple sigma values and choosing the most reasonable value based on the outputs.

The distance scoring function used in the algorithm is found by first integrating the probability density function of the Rayleigh distribution to get the cumulative distribution function (CDF). Then, the complementary cumulative distribution function (CCDF) is simply 1 - CDF. The CCDF has the desired properties for the distance scoring function: a short distance gives a high distance score (Figure 4.13).

Furthermore, using the CCDF for distance scoring makes the distance score equal to the probability of the distance taking on a greater value than d, given that the observation and detection are referring to the same avalanche event:

$$P(D > d|match)$$

Here, the detection location is used as a proxy for the field location the observer was aiming at when placing the map pointer. This is reasonable if the detection and observation are referring to the same avalanche, due to the high positional accuracy of the satellite detections (Eckerstorfer et al., 2019).

Note that the distance scoring function is only used to evaluate spatial proximity and must not be confused with the probability of match given a distance:

$$P(match|D = d)$$

The distance scoring function was established using the distribution of the magnitude of the two-dimensional distance vector given that the observation and detection match. This match assumption is used in a similar manner as a null hypothesis for a right sided hypothesis test (Ross, 2004, p. 292) to apply a distance threshold at a given significance level. When the null hypothesis is true, the distribution of the distance is as described above and the probability of a distance greater than the distance threshold equals the significance level. In Figure 4.13, the distance thresholds can be read from the intersections of the 5% dotted line and the distance scoring function for different values of sigma. Distances larger than the distance cutoff are considered unlikely to represent true matches.

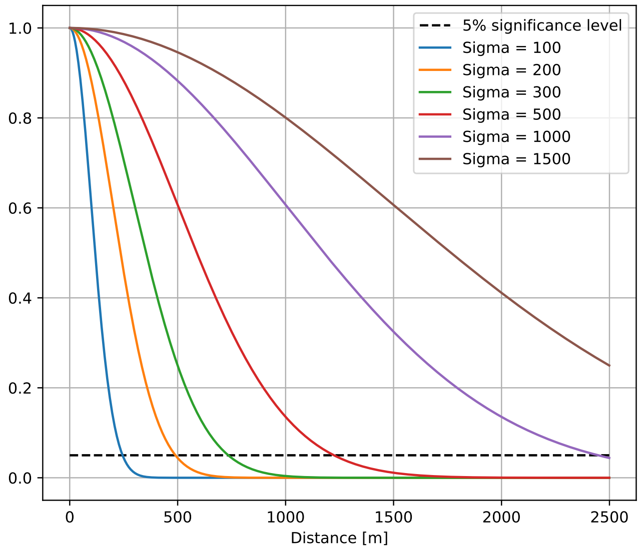

Figure 4.13: The complementary cumulative distribution function of the Rayleigh distributed distance plotted for several values of sigma.

The application of the distance threshold is described when the scores are combined in subsection 4.2.9.

4.2.8 Calculate time scores

The detections have already been filtered in time at this point. However, implementing a time score is useful to smooth the transition between detections considered timematches and those excluded due to observation times outside the allowed timeframe. The smooth cutoff function is the same bump function as the aspect score, only with *cutoff* set to t_1+timeslack. Figure 4.14 illustrates how the time score function gives full score to detections with the observation time fitting within the time interval from t_0 to t_1. Observations of avalanches from times before the reference image time t_0 will not match the change detections, hence the sharp rise from 0.0 to 1.0 at t_0.

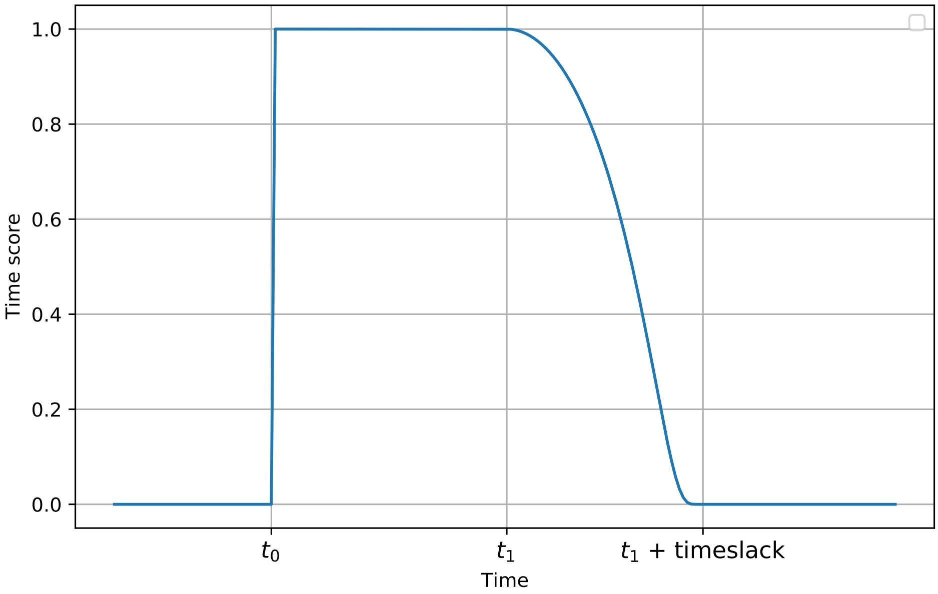

Figure 4.14: Time score function presented with a timeframe between t_0 and t_1 of six days and a timeslack of five days.

4.2.9 Combine scores

The comparison algorithm cannot tell with absolute certainty whether an observation and a detection refers to the same avalanche or not. Therefore, a *match* is a detection similar enough to the observation to be considered possibly referring to the same avalanche event from the similarity criteria applied in the algorithm. If an observation has more than one *match*, the one with the best overall score will be referred to as the *best match*.

In the *combine scores* algorithm step, the aspect- and time-scores are multiplied and the product score is evaluated against a threshold value to ensure that all matches have similar aspect and time as the observation. Likewise, the distance threshold mentioned in subsection 4.2.7 is applied to the distance score to ensure all matches are reasonably close to the observation. All detections with scores exceeding both thresholds are considered matches and their overall score, also referred to as *total score*, is the product of the aspect-, time- and distance-scores (Figure 4.15).

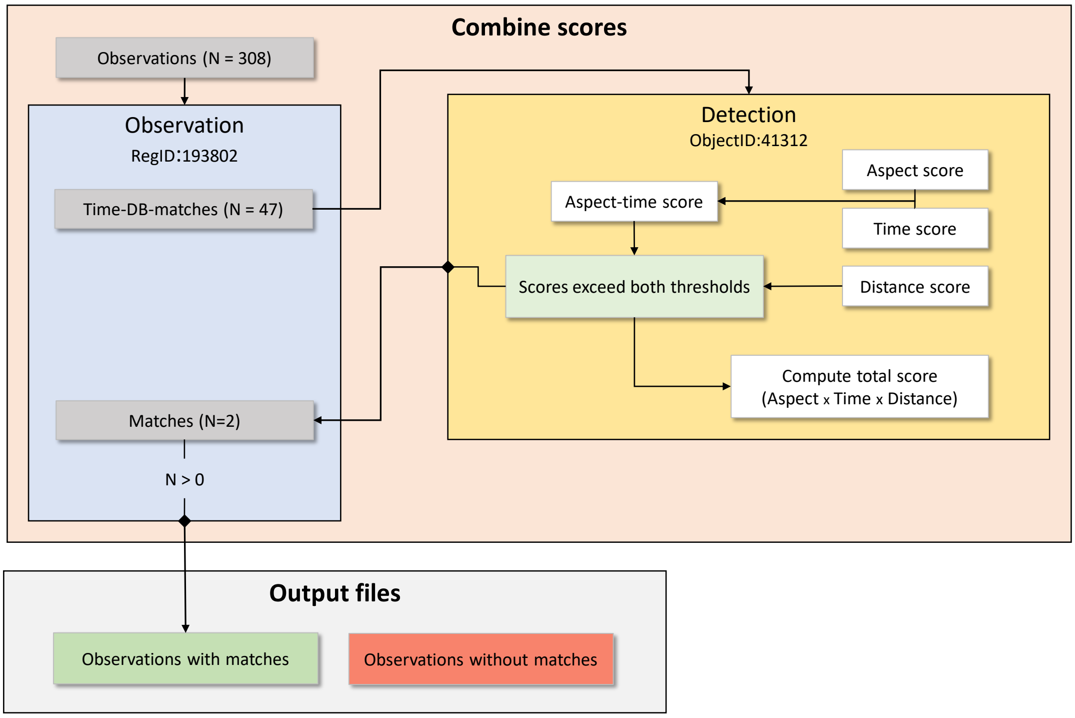

Figure 4.15: The workflow of the algorithm step where scores are evaluated against the score thresholds. The algorithm loopes over all 308 observations and evaluates the scores of all time-DB-matches of each observation. Observation with RegID 193802 and one of its time-DB-matches are used as examples.

Even though all the matches are considered similar enough to possibly refer to the same avalanche as the observation, the *best match* is more likely to be the one originating from the increased radar backscatter associated with the avalanche debris of the observed avalanche.

The different scores are designed to penalize detections with properties that point towards not referring to the same avalanche. Therefore, a full score in either category should be interpreted as "similar enough to avoid a penalty" and not as a "certain match". This score design, together with thresholds and multiplication to get the total score, is preferred over e.g a weighted average of scores as a single unacceptably low score in one of the categories can put the detection outside the list of matches. It is still worth noticing that the total score should not be used to determine the probability of a match, but merely a convenient way of quantifying similarity.

Figure 4.16 illustrates the total score of the matches of RegID 193802. The total score is obtained by multiplying the aspect-, time- and distance-scores. For the best match in Figure 4.16 the scores are as follows:

$$\text{Total score} = \text{Aspect score} \cdot \text{Time score} \cdot \text{Distance score}$$

$$\text{Total score} = 0.696 \cdot 1.00 \cdot 0.981$$

$$\text{Total score} = 0.684$$

This detection is considered a match because both the aspect-time threshold and the distance score threshold was exceeded (Figure 4.15). The total score is used to determine the best match if an observation has more than one match. There is no relation between the number of matches and the total score of the best match.

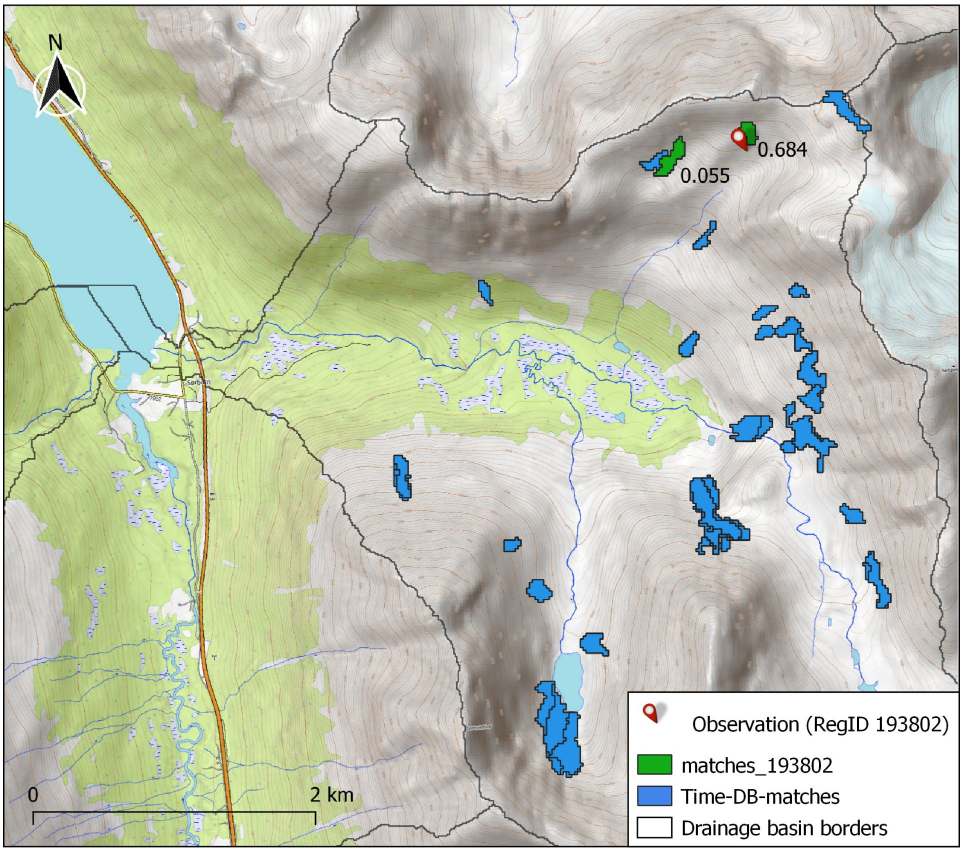

Figure 4.16: Matches of RegID 193802 represented with green polygons and the total scores rounded to three decimals are included next to the polygons. The time-DB-matches are represented by blue polygons. The distance scoring function sigma parameter was 300 and distance was measured between minimum elevation points and stop points.

4.3 Parameter values

The algorithm described above is dependent on a set of parameter values to run. All of the parameters can be tuned and their current values are found in the configuration file. Before producing the results, an optimal set of parameter values were chosen by running the algorithm multiple times and tuning only one of the parameters at a time. *Optimal* in this sense means the values that is thought to make the algorithm recognize as many true matches as possible, while keeping the false matches at a minimum.

The performance related parameters tuned and the corresponding plots are presented in section 5.1. Other algorithm input variables that are not related to algorithm performance, such as spatial and temporal extent of the comparison, are free to be chosen by the algorithm user and are not subject to parameter tuning.

5

Results

This chapter comprises two main sections. First, the selection of algorithm parameters is presented in section 5.1. The results from tuning parameters are given preliminary interpretations and a set of optimal parameter values is put together. Second, the results obtained from running the comparison algorithm is presented in section 6.2. The output from the algorithm is a classification of observations with stop point into a set of observations without matches and a set with at least one match. The most essential properties of the classified observations are explored for the whole AOI over the five seasons 2014 - 2019. Furthermore, a more detailed study of the Lyngseidet area is presented. Finally, an example is given of the results that could be obtained by comparing observations without stop point to the avalanche detections.

5.1 Selecting algorithm parameter values

5.1.1 Observations with stop point

The regObs database has 308 observations with stop points within the AOI for the period 2014 - 2019. This section explores the effects from adjusting parameters on the total number of timematches, the number of observations with *at least one* match, and the number of observations with *only one* match. The plots below are presented using observations with stop point from all five seasons if nothing else is specified.

Timeframe comparison: Timeslack value

The time scoring function used in the timeframe comparison step has a smooth cutoff. The time where the timescore function reaches zero is determined by the timeslack value (Figure 5.1). The interpretation of this parameter is the number of days beyond the timeframe between reference and activity image an observation can be made, and still receive a nonzero timescore.

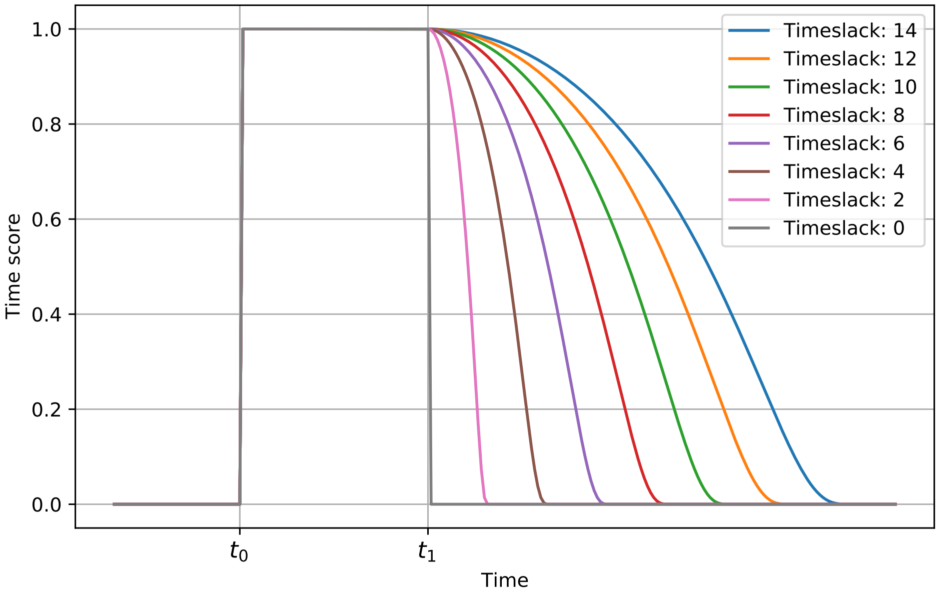

Figure 5.1: The time score function with different timeslack values. The square shape represents the timeframe between reference image time (t_0) and the activity image time (t_1), most often 6 days. The time score is zero for times before t_0, one within the timeframe and gradually slopes off to a cutoff at the timeslack value.

For a detection to be considered a timematch of an observation, the time of the observation must be within the timespan from t_0 to t_1+ timeslack for the detection to get a nonzero timescore. Therefore, by increasing the timeslack parameter value, more detections will be considered timematches. The linear trend of the increase is illustrated in Figure 5.2.

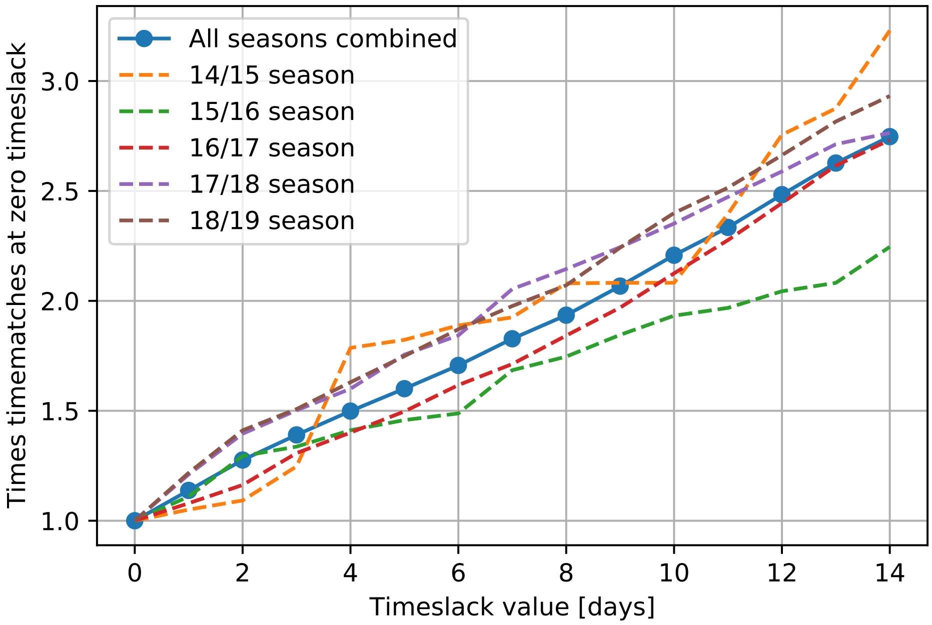

Figure 5.2: Relative timematch proportions plotted against timeslack values for each season (dashed lines). The blue line with dots indicate the combined number for all five seasons (2014 - 2019) and the dots indicate the timeslack values tested.

The optimal timeslack should be set to a value that gives the observers enough time to report an avalanche even if it occurred late in the timespan between t_0 an t_1. Furthermore, the timeslack should be small enough to prevent a high number of avalanches reccuring in the same area being considered matches.

After spatial filtering has been applied, the number of observations with at least one match can be counted. Figure 5.3 illustrates how the timeslack parameter affects the number of observations with at least one match. Consistently, for the three different sigmas tested, the number of matches increases as the timeslack gets larger, which is expected. With a timeslack of 5 to 6 days, there is a tendency in all three graphs of a more gentle increase. This can be interpreted as the timeslack value that optimizes the criteria mentioned above. The steeper increase corresponding to timeslacks of 8 to 10 days could point to when a significant number of avalanche recurrences are considered matches.

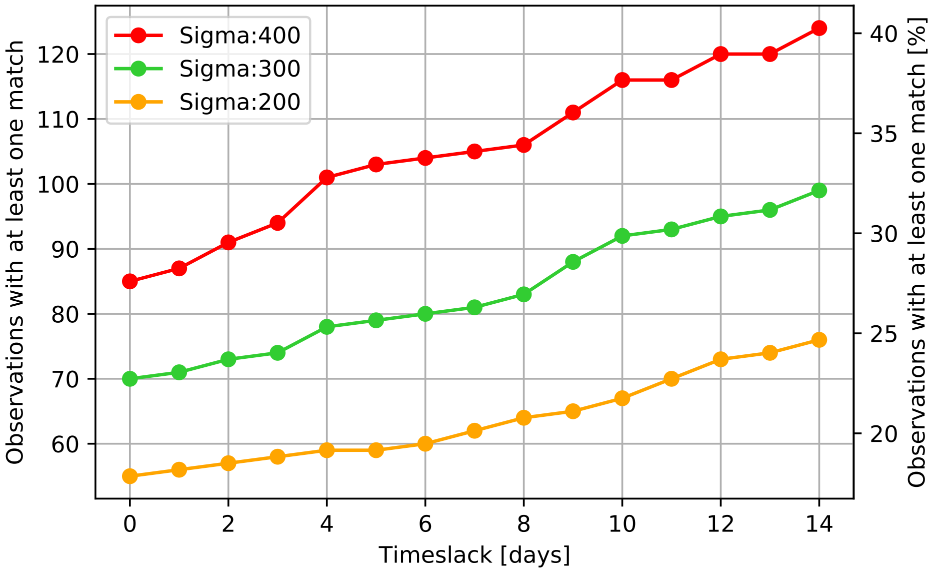

Figure 5.3: Observations with at least one match plotted for different sigma values against timeslack value. The left y-axis shows the number, while the right y-axis shows the percentage of the total of 308 observations. The other parameters were fixed at: aspect cutoff: 160, slope threshold: 3 degrees, CCDF threshold: 0.05, aspect-time threshold: 0.1

Distance scoring: Sigma value

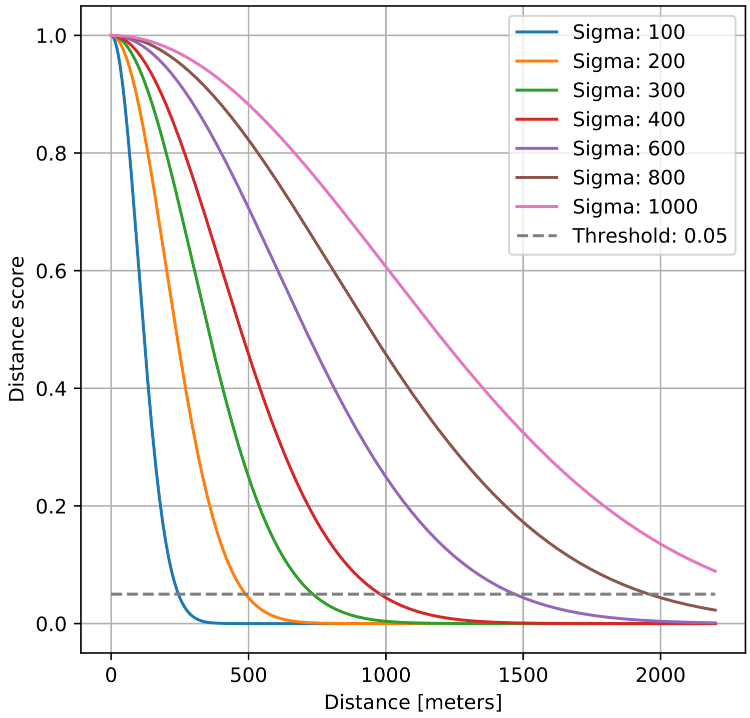

Figure 5.4: The distance scoring function based on the complementary cumulative distribution function of the assumed Rayleigh distributed distance variable. The 5% threshold intersections indicate at which distance the detections are too far to be considered likely matches for each sigma.

Sigma, the shape parameter of the distance scoring function determines how relaxed, or non-restrictive the algorithm is when evaluating the spatial similarity of observations and detections (Figure 5.4). The sigma value is an important parameter as it largely influences the count of observations with matches. This is apparent from Figure 5.3 where the larger sigma values produce larger match counts. The distance threshold is kept at a 5% of the maximum distance score, while the shape parameter is tuned in this section.

To decide on the optimal sigma value for the observations with stop point, the value that recognizes the most true matches while keeping the number of false matches low is again sought after. Without training data of actual matches, the procedure is again to apply reasoning and plot the results for different parameter values.

Two different effects determine the number of observations with only one match when increasing the sigma value:

1. Observations without matches getting their first match at a given sigma value contribute to a higher count
2. Observations with one match getting additional matches at a given sigma value contribute to a lower count.

The second effect is mostly unwanted as the additional matches are likely false matches, while the first is desired to ensure including the true matches. Figure 5.5 indicates that a sigma value around 400 is optimal. The figure was produced by running the algorithm on both age-tracked and the all-detections dataset. The local maximum at 400 indicate that this is the sigma value giving the most observations with only one match. However, there is no way of knowing whether the single match is a true match or not. Above 400, the second effect is larger than the first, making the count drop due to multiple matches.

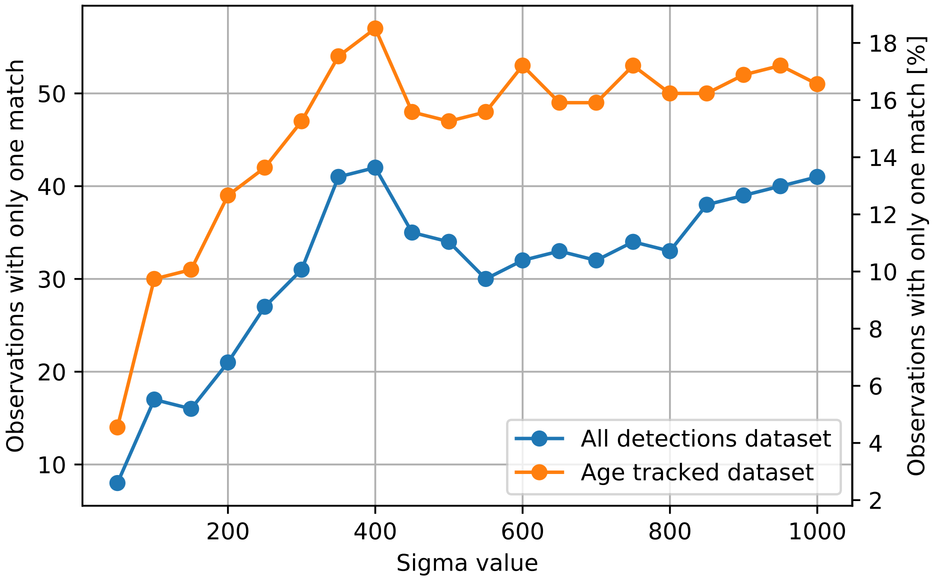

Figure 5.5: Number of observations with only one match plotted for each season against sigma value of the distance scoring function. The points on the lines indicate which sigma values were tested. The other parameters were fixed at: timeslack: 5 days, aspect cutoff: 160, slope threshold: 3 degrees, CCDF threshold: 0.05, aspect-time threshold: 0.1

After manually reviewing all regObs entries of avalanche observations in the Tromsø and Lyngen regions for the 2018 - 2019 season, the impression is that observers generally are quite accurate when placing stop points. A sigma value of 400 at a 5% threshold gives a threshold distance of 979 meters (Figure 5.4). This appears to be too relaxed, running the risk of including a large number of false matches. The distance thresholds for sigmas of 200, 300 and 400 is illustrated in Figure 5.6, centered around the avalanche observation with RegID 193802. By manual evaluation of the regObs entry with the attached comment and image, the detection closest to the observation is considered a match.

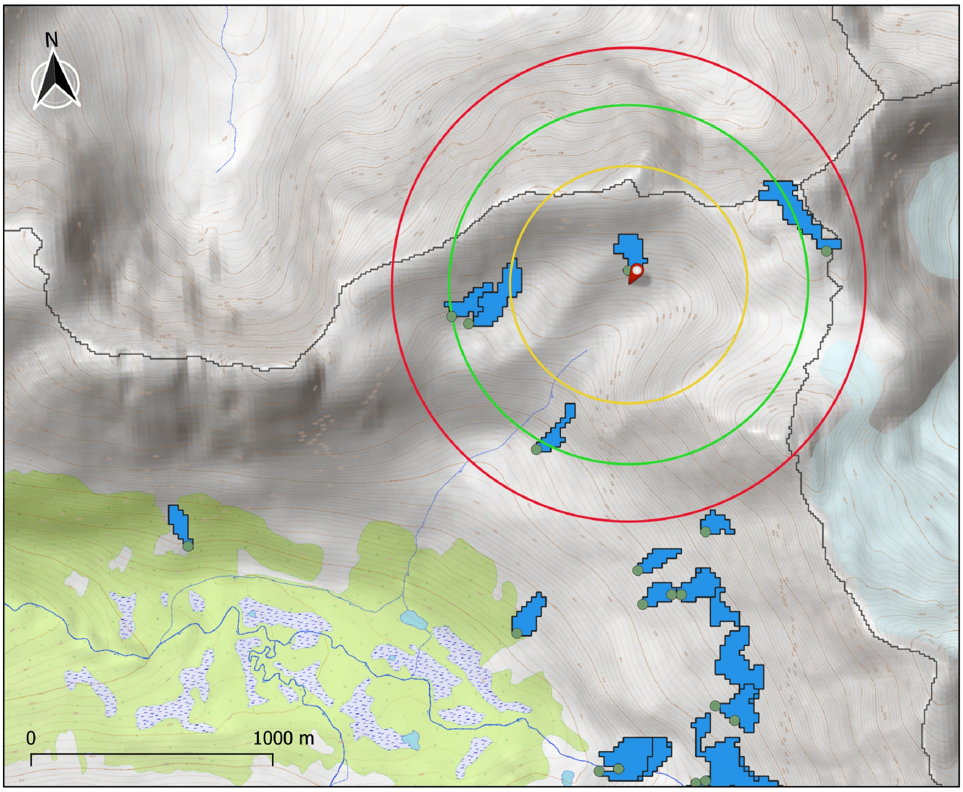

Figure 5.6: Observation with RegID 193802 (red marker) surrounded by circular distance 5% threshold cutoffs for sigma values of 200 (orange), 300 (green) and 400 (red). The radii are 489, 734 and 979 meters, respectively. Detections are illustrated by blue polygons with dark green points indicating their minimum elevation points.The drainage basin perimeter is represented by black lines along the watersheds.

By combining the impressions from manual evaluation of the regObs entries and Figure 5.5, the sigma value is set to 300 for the optimal set of parameters.

Aspect scoring: Aspect cutoff value

The aspect scoring function is defined using the same bump function as the smooth cutoff of the time score, and can be tuned by using different aspect cutoff values (Figure 5.7).

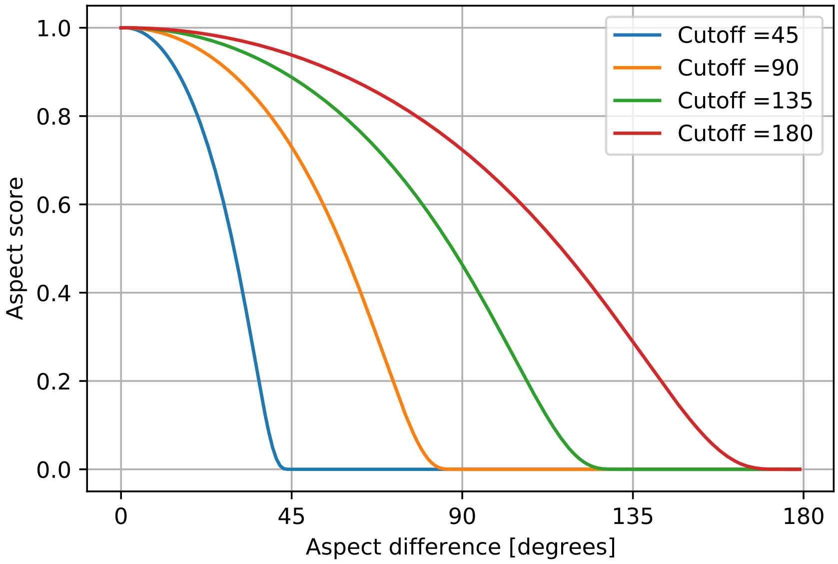

Figure 5.7: Aspect scoring function plotted for four different aspect cutoffs.

The purpose of aspect scoring is to reduce the score of detections with largely different aspect than the observation. Figure 5.8 illustrates how the aspect cutoff affects the number of observations with at least one match. The aspect cutoff does not significantly contribute to disregarding detections if the value is set above 90 degrees. There is also a tendency towards aspect filtering affecting the count more for large values of sigma. This is likely due to very few detections with large aspect differences being located within the distance cutoff circles (see Figure 5.6). Consequently, the aspect cutoff is more influential when using large sigma values.

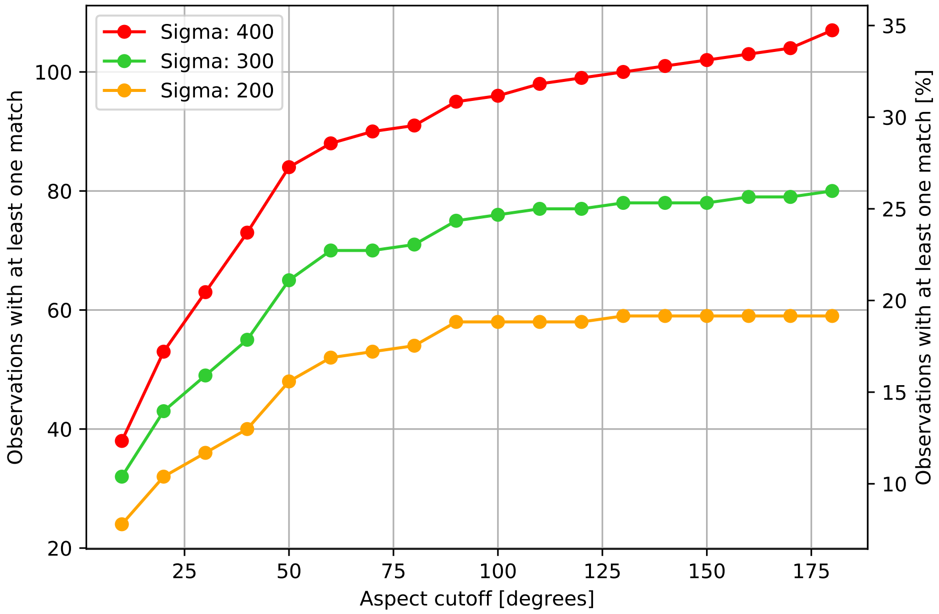

Figure 5.8: Observations with at least one match plotted against the aspect cutoff value using three different sigma values. The other parameters were fixed at: timeslack: 5 days, slope threshold: 3 deg, CCDF threshold: 0.05, aspect-time threshold: 0.1

Aspect scoring: Slope threshold value

The aspect of a slope is not well-defined for flat terrain. Therefore, a slope threshold is applied to avoid having to assign aspect values to points located on near-flat slopes. The aspect score is set to 1 for observations with stop point below the slope threshold. By design, this is equivalent to not evaluating their aspects, as the scoring system effectively assigns score penalties based on the degree of dissimilarity between observations and detections. Therefore, increasing the slope threshold will simply reduce the number of observations with aspect score less than one. Because the aspect would be close to arbitrary on near-flat terrain, potential matches could be disregarded if the slope threshold is set too low.

The histogram of the slope angles, measured at the stop point of the observations using the 10 m DEM is presented in Figure 5.9. Twelve observations with stop point at a slope below three degrees were made during the 2014 - 2019 period. The slope threshold decided on for the optimal parameter set is three degrees.

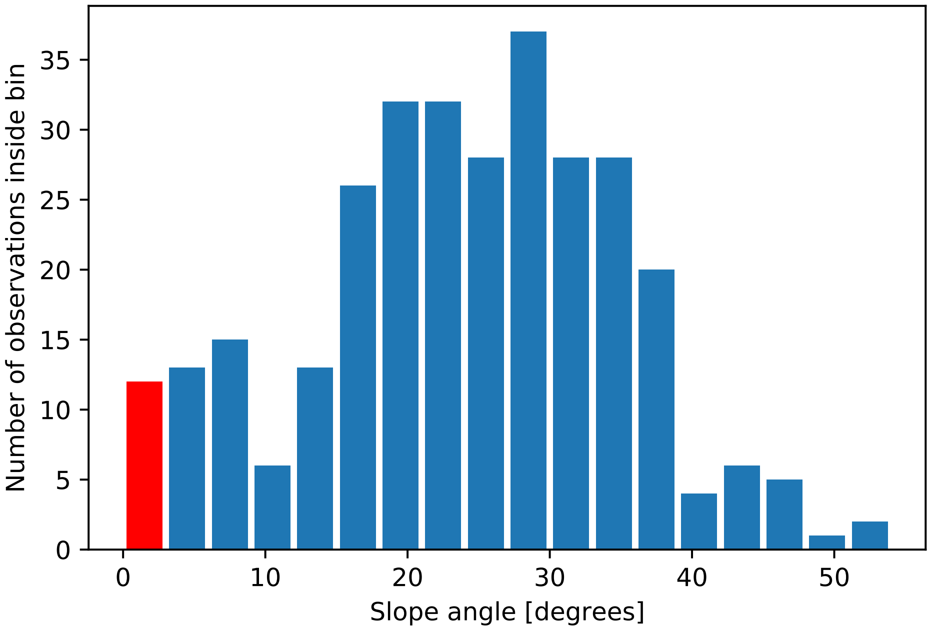

Figure 5.9: Histogram of avalanche observation slope angles measured at the stop point. The bin size used is three degrees. The red column represents the observations affected by the slope threshold.

Aspect-time threshold and distance threshold values

The thresholds placed on the aspect-time score and the distance score can be tuned to adjust the algorithm performance. However, the parameters of the scoring functions these thresholds are applied to have already been tuned. The thresholds are therefore kept at the initial values used during parameter tuning. The 5% significance level for the distance score threshold also has the added statistical reasoning behind it (Subsection 4.2.7).

Both thresholds are necessary to evaluate which detections have been assigned scores that are not compatible with referring to the same avalanche as the observation.

Parameter selection summary

The parameters set above are summarized in Table 5.1.

Table 5.1: The (assumed to be) optimal set of comparison algorithm parameters for observations with stop point.

Parameter	Optimal value
Timeslack	5 days
Sigma	300
Aspect cutoff	130 degrees
Slope threshold	3 degrees
Aspect-time threshold	0.1
CCDF threshold	0.05

5.1.2 Observations without stop point

If observations without stop point are used, a few of the parameters must be adjusted. The distance is then calculated from the position associated with the registration, as opposed to the stop point location. Therefore, the shape parameter of the distance scoring function, sigma, should be changed accordingly. The estimated optimal sigma used for observations with stop point can be reused here as an estimate of the error introduced by placing a pointer in the map in general.

From reviewing regObs entries manually, the general impression is that observers focus on the release area when entering registration location. The avalanche detection polygons only represent avalanche debris (Section 3.1). Consequently, comparing the polygon centroid to the registration location introduces a potential uncertainty related to the avalanche path length. The reported avalanche size can be used to choose the typical path length, following Table 2.1

The observer has the option of entering positional uncertainty related to the registration location. The seemingly unrealistic uncertainty value of zero meters is the most frequently entered for registations made using the regObs web site (Figure 3.5). Furthermore, all observations registered using the regObs mobile app are automatically assigned zero meters uncertainty. The observations with registration location set using the GPS location of a smart phone should be disregarded, as this position is the observer location and could potentially be very far from the avalanche.

The new sigma values can be calculated by adding the three uncertainty contributions in quadrature:

$$\text{sigma} = \sqrt{\text{path}^2 + \text{uncertainty}^2 + \text{pointer}^2}$$

Where *path* is the typical path length of an avalanche of the reported destructive size, *uncertainty* is the reported positional uncertainty and *pointer* is the error related to placing a pointer in the map. If not given, the path length can be computed as a weighted average of the other path lengths. In that case, the resulting typical path length of avalanches reported without stop point in the AOI during the 2014 - 2019 period is 598 meters.

5.2 Presenting results

In this section the results from running the algorithm with the parameter settings described in section 5.1 will be presented. The classification result for each avalanche observation can be found in Table 9.1 in the appendix. The output from the algorithm is, in essence, a classification of observations into those with at least one match and those without matches. Some of the classification results are validated by examining the regObs entries manually. All of the presented plots represent the algorithm output and are not adjusted according to the manual validation. Emphasis will be placed on the classification of observations with stop point. These results are first presented for the entire AOI, before the results from focusing on the Lyngseidet area are presented. Finally, an excerpt of the results obtained from running the algorithm with observations without stop point is presented in subsection 5.2.8.

Observations with stop point are considered the most applicable for direct comparison to avalanche detections (Section 3.2). In this category, a total of 308 avalanche observations from 2014 - 2019 were evaluated by the comparison algorithm. 78 (25.3%) of these had at least one match, while 230 (74.7%) had no matching detections. Several properties of the classified observations are investigated below. Consistently, green color is used to represent observations with matches, while red is used for observations without matches.

5.2.1 Observation location

The spatial distribution of the classified observations within the AOI is presented in Figure 5.10. The locations of the observations span most of the mountainous regions of the AOI. Some clusters of observations can be identified in popular areas for backcountry recreation, such as Lyngseidet (A) and Kattfjordeidet (B). Furthermore, clusters of observations can be identified close to the ground based radar installation in Holmbuktura (C) and infrasound installation in Lavangsdalen (D) (Section 3.2.2). Figure 5.10 is presented with green dots as the uppermost layer, which can give a false impression of very high match percentages in some of the observation clusters.

The area with a high density of observations that stood out with regards to low match percentage, was the area centered over Lyngseidet. This area has been investigated in detail and the results are presented in subsection 5.2.7.

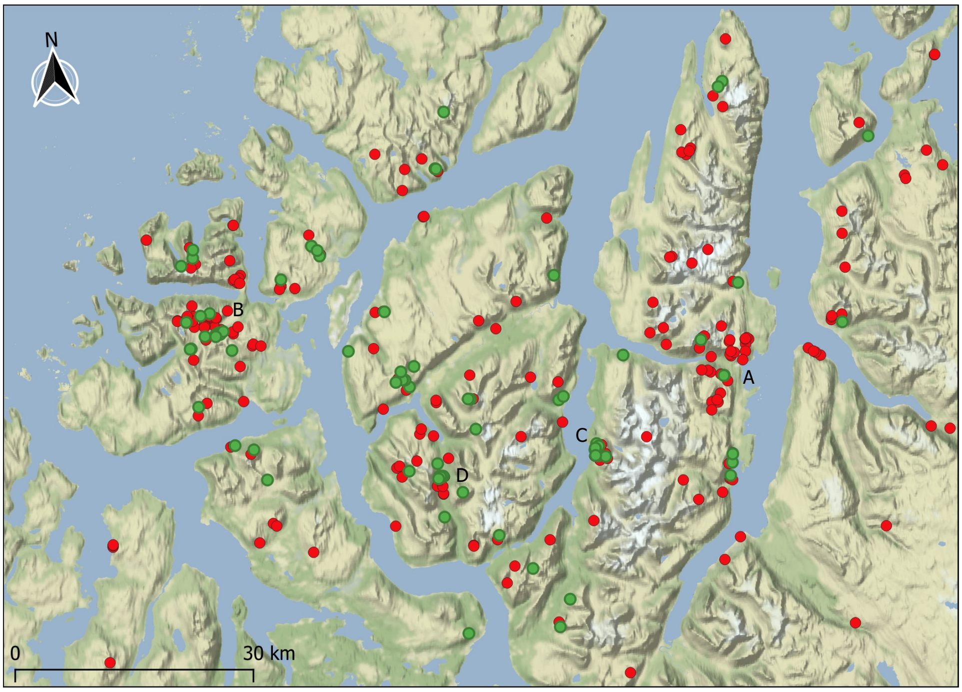

Figure 5.10: Map of the AOI with green points representing observations with matches and red points representing observations without matches. The green points have been added on top of the red and may hide some of the observations without matches. Labeled areas with a high density of observatons: Lyngseidet (A), Kattfjordeidet (B), Holmbuktura (C) and Lavangsdalen (D).

5.2.2 Reported Avalanche size

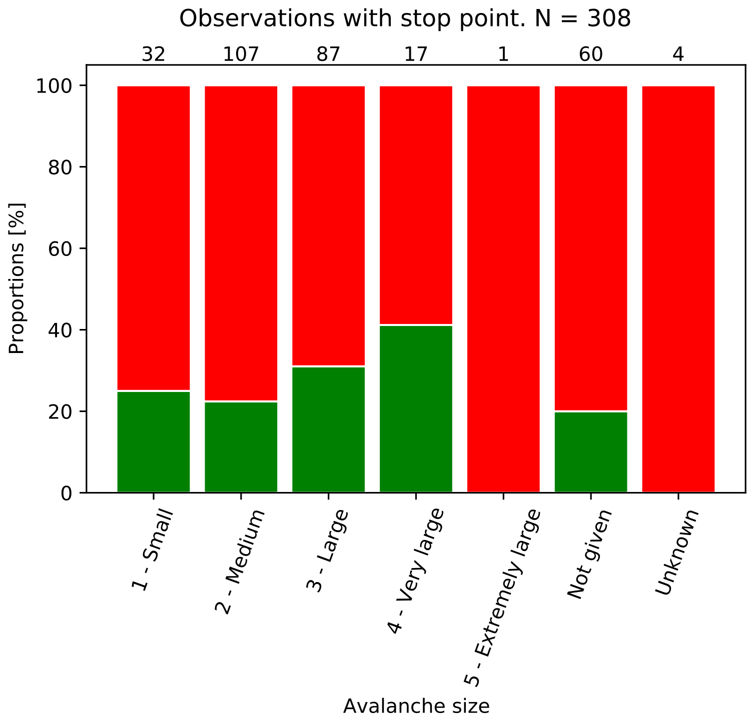

Figure 5.11: Reported avalanche size plotted for observations with stop point. The observations are classified into observations with at least one match (green) and without matches (red), and plotted by proportions within each avalanche size.

The observers have the option to estimate avalanche size when registering an avalanche observation. The distribution of reported avalanche size of the classified observations is presented in Figure 5.11. The two most frequently reported avalanche sizes are size 2-*Medium* and 3-*Large*.

The *Not given* category accounts for 60 of the observations and together with the 4 entered as *Unknown*, roughly one fifth of the observations have unspecified avalanche sizes. Further investigation of these observations found that 41 of the 60 observations with avalanche size *Not given* were entered by the account *drift@svv* (an account associated with the Norwegian Public Roads Administration (SVV)).

A tendency towards higher match percentages for the *Large* and *Very large* avalanches can be seen in Figure 5.11.

The 32 avalanche observations with reported avalanche size 1-*Small* were investigated further by manually applying all the entered regObs information, including text comments and images, to validate the comparison algorithm classification. Out of the 8 avalanches of reported size 1-*Small*, 6 had only false matches, i.e detections incorrectly classified as matches. The other two observations with matches, were both wet loose-snow avalanches with long runout lengths. All of the 24 observations without matches was considered by the manual validation to be correctly classified, meaning that the avalanche was not detected. The match proportion of observations of reported size 1-*Small* is 2 out of 32 (6%) using manually validated numbers.

The 17 observations with reported avalanche size 4-*Very large* were examined the same way with the following results. 6 of the 7 avalanche observations with matches were confirmed to be correctly classified, while the last one was a false match and the avalanche was not detected. 9 out of the 10 observations classified without matches were correctly classified by the comparison algorithm. One observation was incorrectly assigned no matches. This observation had two detections matching the images and comments entered to regObs. Further investigation found that the aspect difference was higher than the aspect threshold value of 130 degrees. In summary, the manual comparison found that two observations were incorrectly classified, while the match proportion of the size 4-*Very large* avalanches was correct at 7 out of 17 (41%).

The single avalanche of size 5-*Extremely large* without matches can not be used to infer any general knowledge of the detectability of destructive size five avalanches. Nevertheless, the observation was validated manually and found to be correctly classified. The image and comments indicated that this was a spontaneously released dry slab avalanche and the placement of the stop point was accurate.

5.2.3 Reported Avalanche type

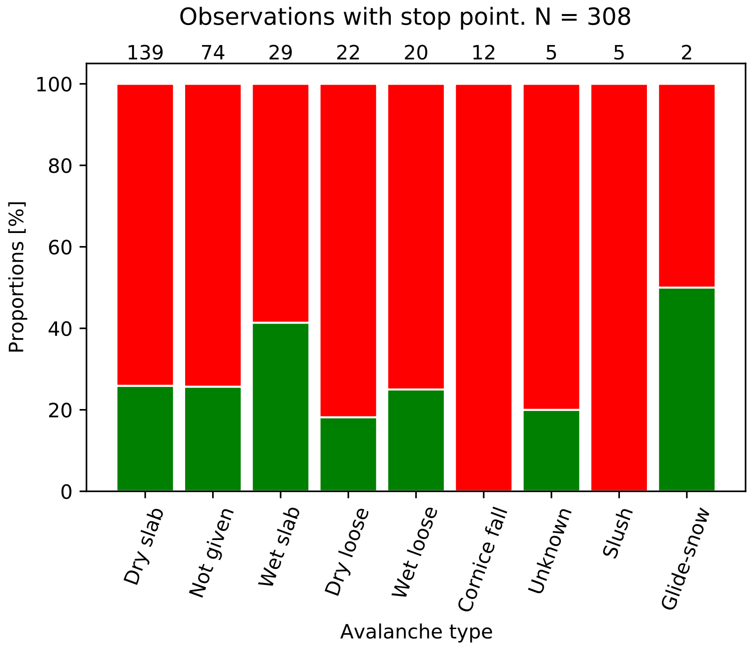

Figure 5.12: Reported avalanche type plotted for observations with stop point. The observations are classified into observations with at least one match (green) and without matches (red), and plotted by proportions within each avalanche type.

Similar to avalanche size information, it is optional to include the avalanche type. Figure 5.12 illustrates the reported avalanche types of the classified observations, including columns for *Not given*. Once again, a large portion (41 out of 74) of the observations with avalanche type *Not given* was entered by *drift@svv*. Out of the specified avalanche types, *Dry slab* avalanches were by far the most frequently entered.

Observations of *Wet slab* avalanches have the highest match percentage when disregarding the single *Glide-snow* avalanche with match resulting in 50%. A tendency towards the wet avalanches having a larger percentage of matches can be interpreted from Figure 5.12. Both within the slab avalanche category and the loose snow category the wet avalanches have higher match percentages. However, the match proportion of *Dry slab* and *Wet loose* are roughly equal, 36 out of 139 (26%) and 5 out of 20 (25%), respectively.

None of the 12 *Cornice fall* observations or 5 *Slush* avalanches have matching detections.

5.2.4 Observation time

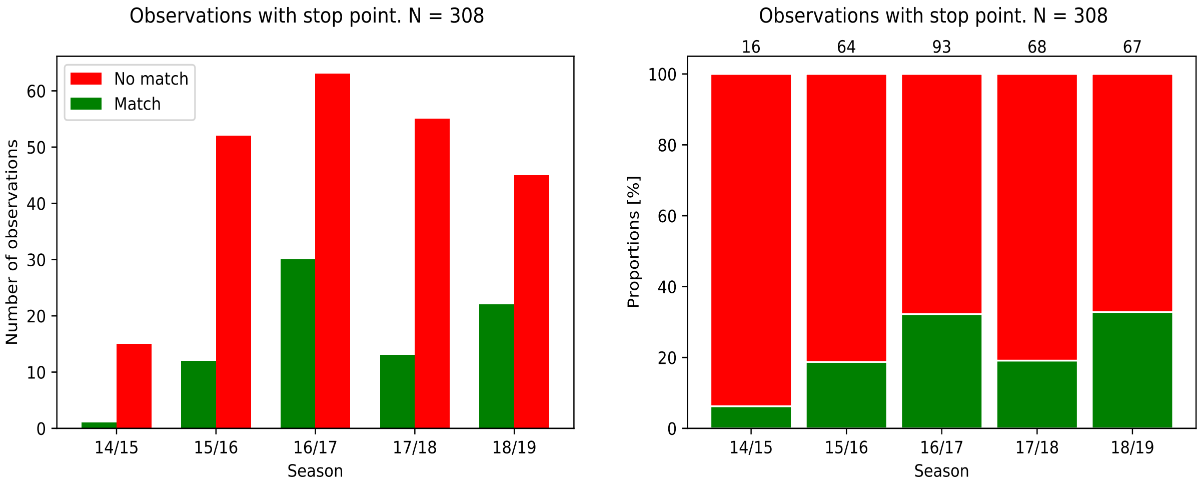

(a) (b)

Figure 5.13: Observations with stop point plotted against season. The observations are classified into observations with at least one match (green) and without matches (red), and plotted by number (a) and proportions (b) within each month.

The observation time of the observations divided into the five seasons studied is illustrated in Figure 5.13. Only 16 observations belong to the 2014 - 2015 season. The other four seasons have consistently over 60 observations with a maximum of 93 in the 2016 - 2017 season.

The match proportion for season 2018 - 2019 is only marginally larger than for season 2016 - 2017, with 33% and 32% respectively.

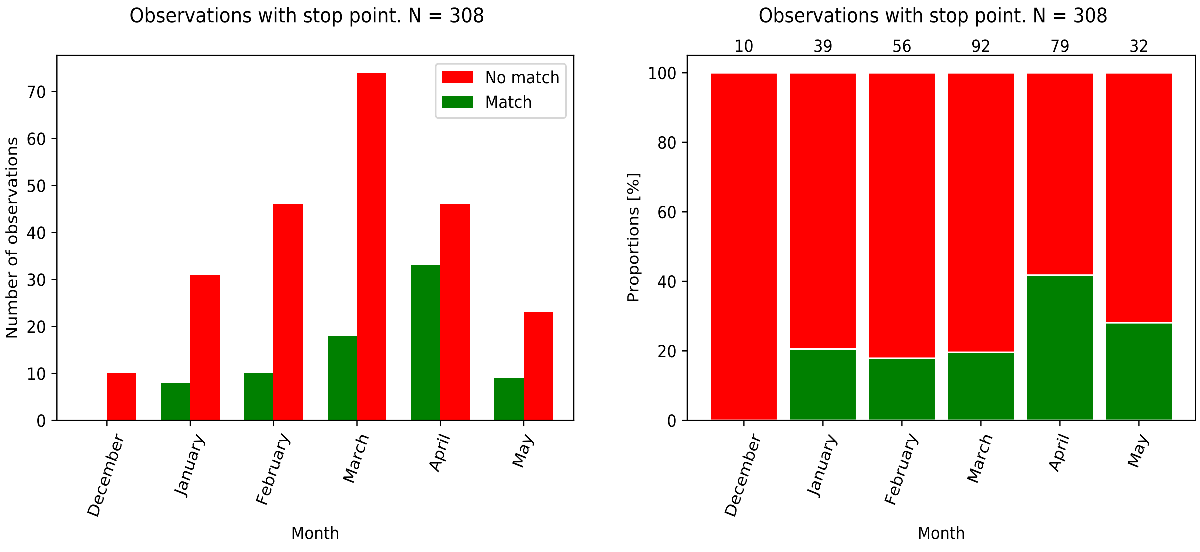

(a) **(b)**

Figure 5.14: Observations with stop point plotted against month. The observations are classified into observations with at least one match (green) and without matches (red), and plotted by number (a) and proportions (b) within each month.

The monthly distribution of the observation time is illustrated in Figure 5.14. The number of observations is highest for March and gradually decreases towards the end and beginning of the seasons.

None of the 10 observations from December had matching detections. The match percentage for April stands out as the highest with 42 %. For December and April, the avalanche sizes and avalanche types are illustrated in Figures 5.15 and 5.16. The size distribution for December is roughly even between sizes 1-*Small*, 2-*Medium* and 3-*Large*. The size distribution for April resembles the distribution from Figure 5.11, only with generally higher match proportions.

By comparing the avalanche type distributions for the two chosen months against the overall type distribution in Figure 5.12, some differences can be identified. *Dry slab* avalanches account for 9 out of 10 December observations, which is a higher proportion than 139 out of 308 (45%) overall. For April, dry slab avalanches are the most reported, but avalanches of types *Wet slab* and *Wet loose* are more represented than in Figure 5.12. Figure 5.17 illustrates the size distribution of the dry slab avalanches observed in April. No significant difference in size distribution can be found by comparing these avalanches to the overall size distribution illustrated by Figure 5.11.

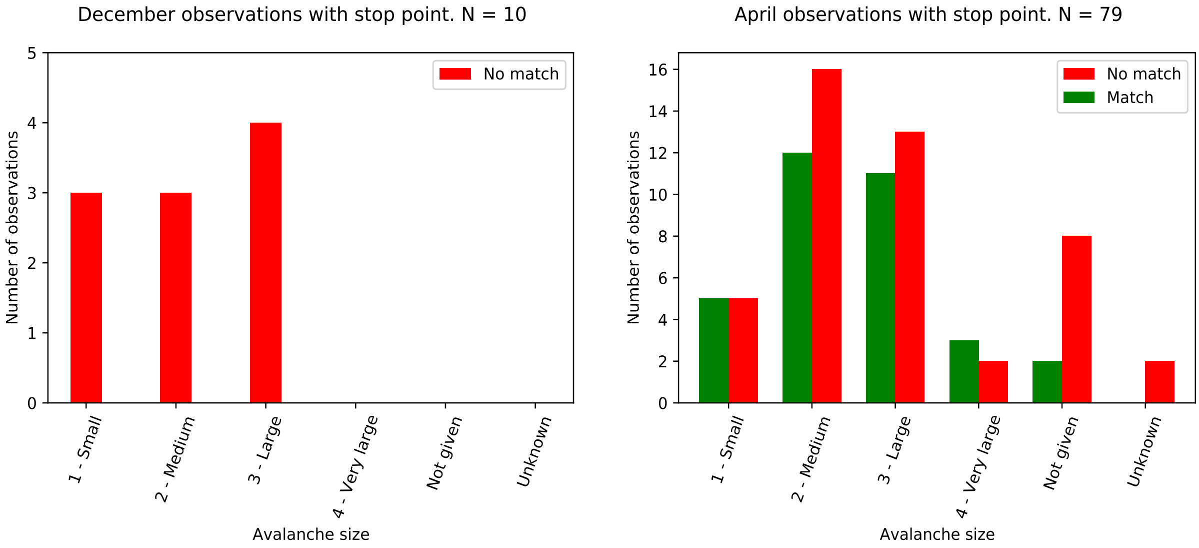

(a) **(b)**

Figure 5.15: Observations from December (a) and April (b) with stop point plotted against avalanche size. The observations are classified into observations with at least one match (green) and without matches (red).

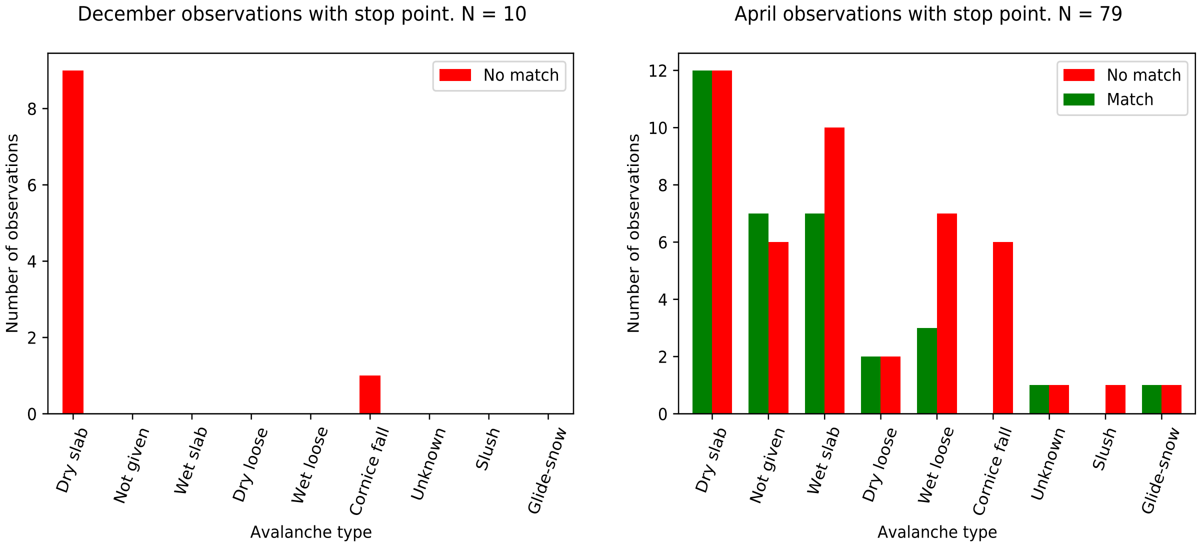

(a) **(b)**

Figure 5.16: Observations from December (a) and April (b) with stop point plotted against avalanche type. The observations are classified into observations with at least one match (green) and without matches (red).

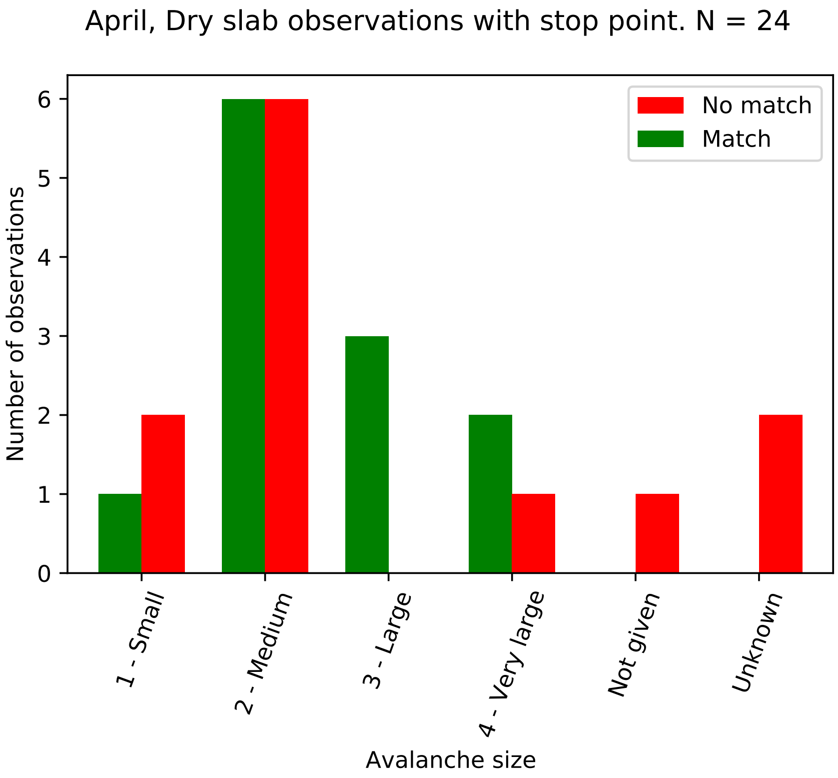

Figure 5.17: Observations from April of type *Dry slab* plotted against reported avalanche size. The observations are classified into observations with at least one match (green) and without matches (red).

5.2.5 Slope angle

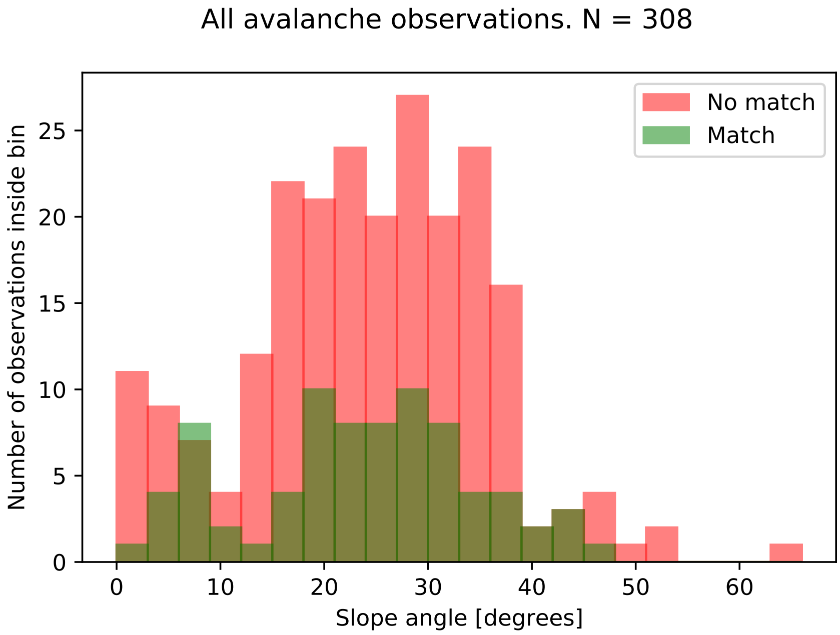

Figure 5.18: Superimposed slope angle histograms for observations with and without matches. The bin size is three degrees. The slope angle is computed from the DEM at the stop point location.

Figure 5.18 illustrates the slope angle distributions of the classified observations. The histograms are superimposed to investigate for shape differences suggesting slope angle dependency. No obvious shape differences can be seen from figure 5.18.

5.2.6 Aspect

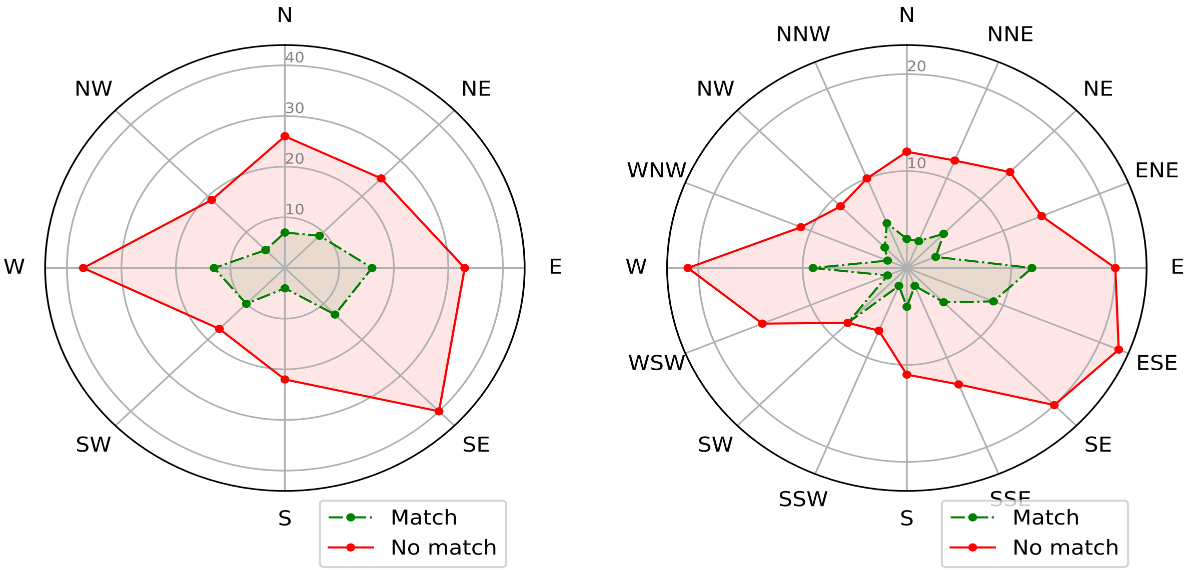

(a) **(b)**

Figure 5.19: Aspect plotted for observations with stop point and slope angle above slope threshold (N = 296). The observations are classified into observations with at least one match (green) and without matches (red), and divided into 8 and 16 directions in sub-figures (a) and (b), respectively. The radial axis represents the number of observations within each aspect direction.

The aspect of the observations measured at the avalanche stop point location is illustrated in Figure 5.19. A pattern where observations on slopes facing west and east/southeast can be seen. This pattern is found both when categorizing aspect into 8 and 16 directions. However, no significant difference in the aspect distributions between observations with matches and observations without matches can be determined from Figure 5.19.

8 of the 30 observations on slopes facing west in Figure 5.19 (b) were from the Holmbuktura radar installation. The eight avalanche observations from the infrasound installation in Lavangsdalen were done on slopes facing east (5 observations), east-southeast (2 observations) and northeast (1 observation).

5.2.7 Focus area: Lyngseidet

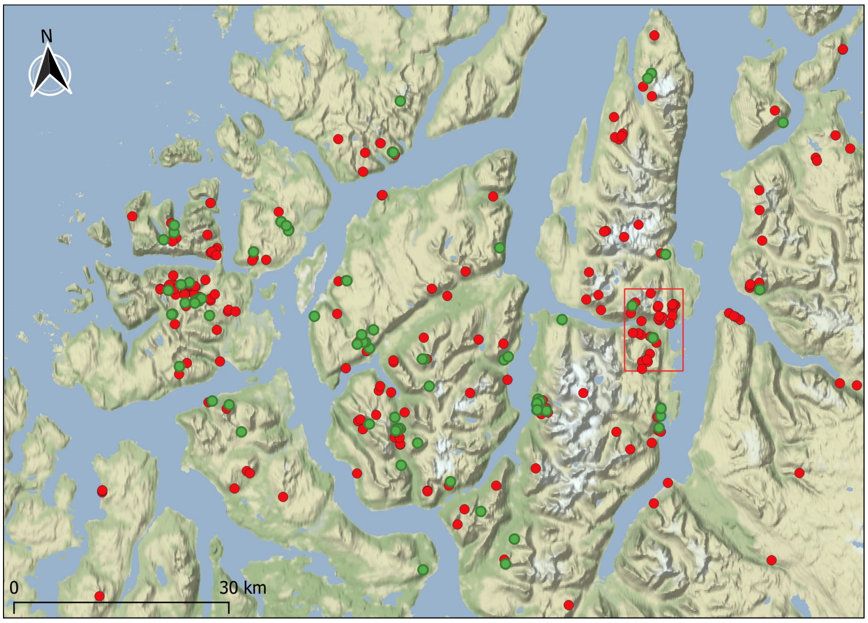

Figure 5.20: Map of the AOI with classified observations represented by red and green dots. The Lyngseidet focus area is illustrated by a red rectangle.

Some areas with a high density of observations were identified from studying Figure 5.10. One area with a high number of observations and a low number of observations with matches is Lyngseidet (Figure 5.20). Out of the 33 observations, 3 (9%) had matching detections.

In Figure 5.21, the observations and detections in the Lyngseidet area from 2014 - 2019 are illustrated. It should be noted that the detections are not time filtered with respect to any of the observation times. Therefore, only spatial proximity can be seen directly. The observations without matches located close to detected polygons in Figure 5.21 and Figure 5.22 have observation times that are very different from the detection timeframe, which explains the no-match classification.

The number of observations in the Lyngseidet area is relatively low, making it possible to manually review the observation entries. A thorough manual comparison of the observations and detections in the area was conducted using the observation comments and images in addition to the spatio-temporal information. The manual comparison gave the same classification as the comparison algorithm for the Lyngseidet area.

One of the observations can be interpreted from the comments to be a duplicate, meaning the same avalanche event has been entered twice. The comments

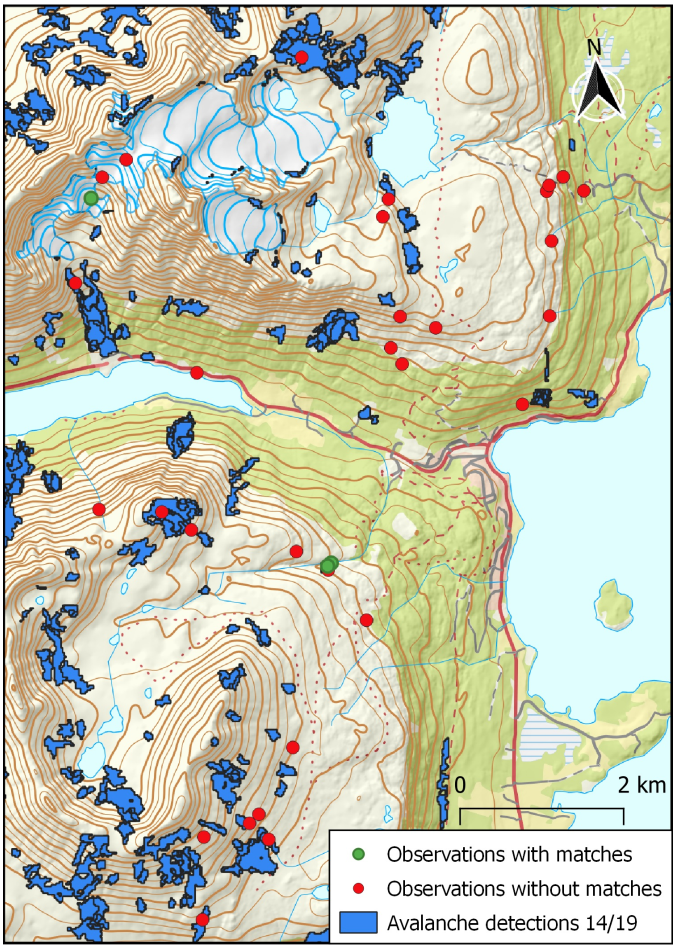

Figure 5.21: Overview of the Lyngseidet focus area with classified observations as green and red dots. The avalanche detections from 2014 - 2019 are presented as blue polygons.

added to the observation gives the impression that the observer who entered both observations did not understand the Norwegian questions in the form. The lenght and type of the avalanche is stated in the comments in English. The numbers presented for Lyngseidet are not altered to account for the duplicate entry.

The masks applied by Eckerstorfer et al. (2019) to remove detections on glaciers, in dense forest and agricultural areas are applied in Figure 5.22. The figure illustrates how all three observations in the upper left corner are within the area masked by the glacier mask. The residue of one detection polygon outside the glacier mask explains why one of the observations has a match. Several observations illustrated in Figure 5.22 are located in areas where no avalanche detections were made during the entire 2014 - 2019 period.

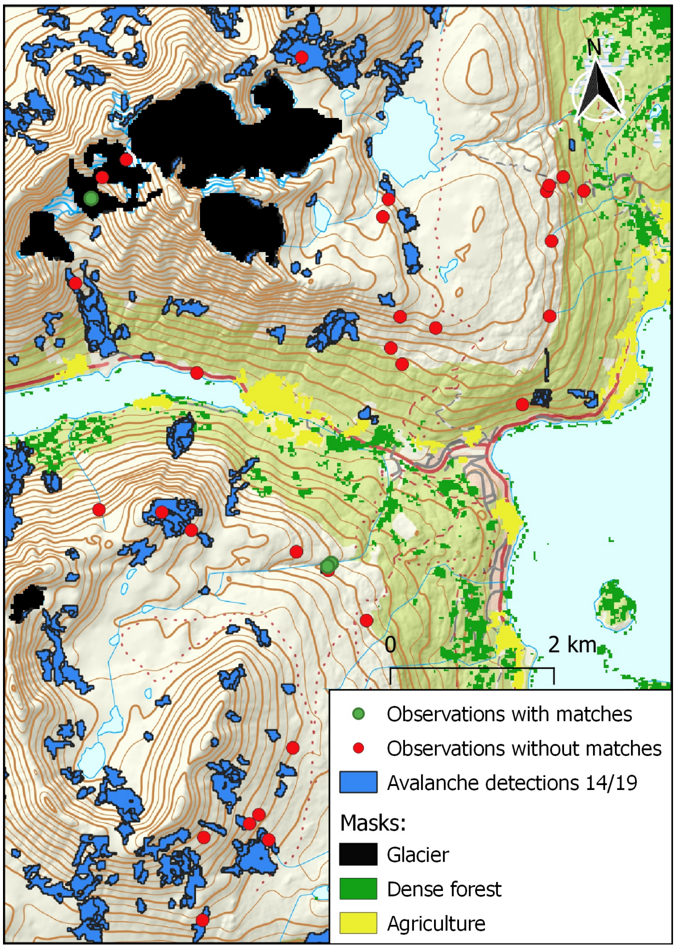

Figure 5.22: The classified observations from Lyngseidet with stop point plotted with some of the masks applied by Eckerstorfer et al. (2019).

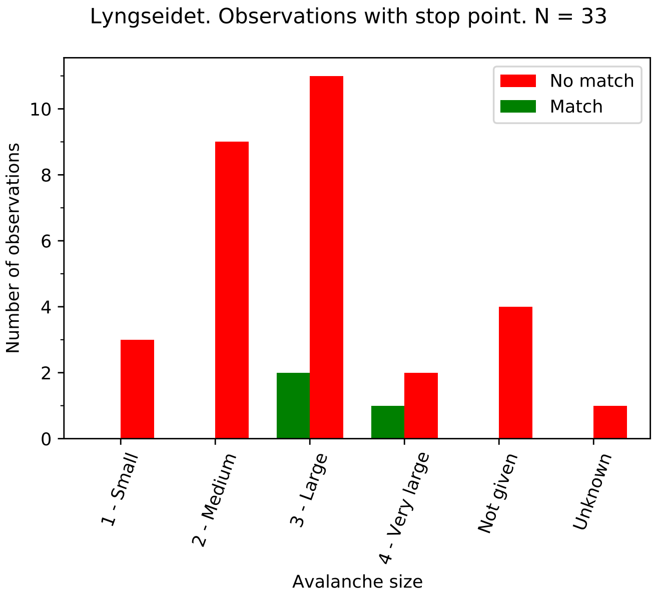

Figure 5.23: Reported avalanche size of the classified observations from the Lyngseidet area.

The three observations with matching detections belong to avalanche sizes 3-*Large* and 4-*Very large*. None of the size 1-*Small* or 2-*Medium* avalanches have matching detections (Figure 5.23).

Dry slab avalanches account for a substantial amount of the observations in the Lyngseidet area, with 21 out of 33 (Figure 5.24).

The majority of observations from the Lyngseidet area was registered by three observer accounts, as illustrated by Figure 5.25.

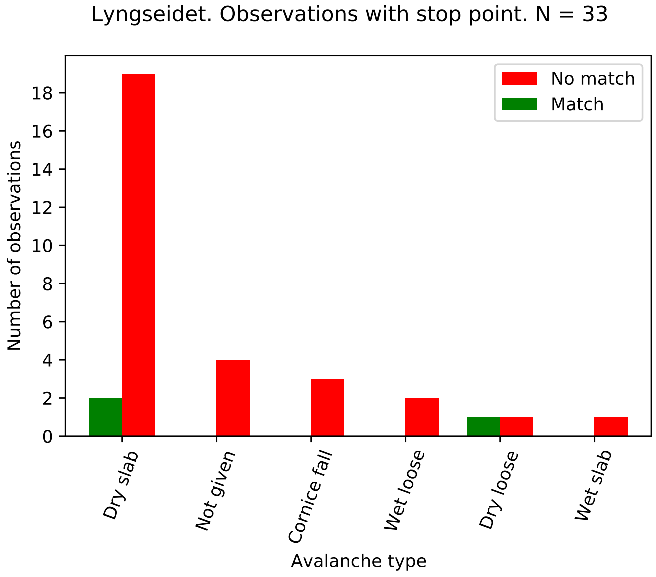

Figure 5.24: Reported avalanche type of the classified observations from the Lyngseidet area.

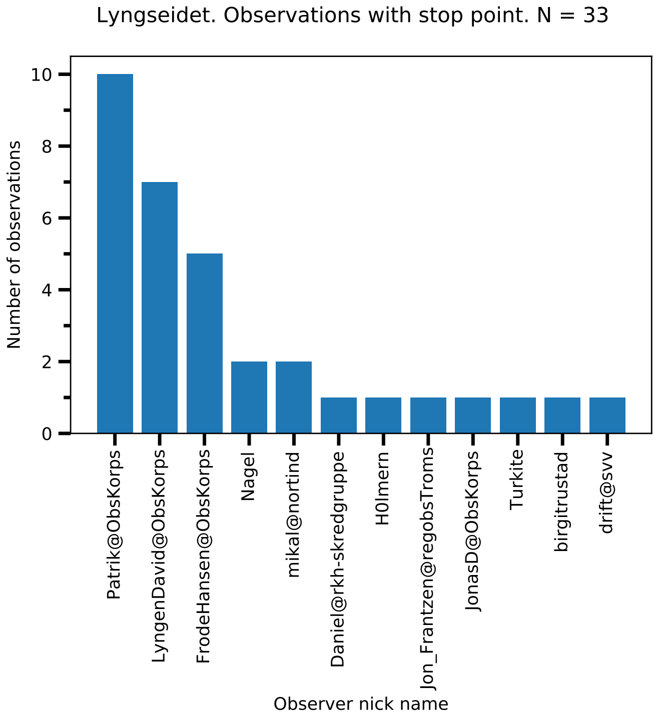

Figure 5.25: Bar-plot of the different observer accounts contributing to regObs in the Lyngseidet area in the 2014 - 2019 period.

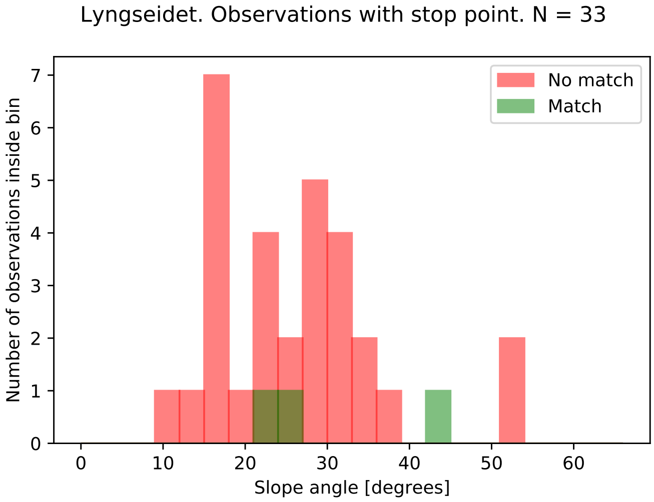

Figure 5.26: Superimposed histograms of stop point slope angle of the classified observations from the Lyngseidet area.

The slope angle distribution of the observations from Lyngseidet (Figure 5.26) does not differ significantly from the slope angle distribution observed elsewhere in the AOI (Figure 5.18).

5.2.8 Observations without stop point

Observations without stop point are considered to have a larger positional uncertainty and must be handled with care (Section 3.2.2). This section is not aiming to explore the result from running the comparison algorithm with these observations. Instead, the section should be viewed as an example of the results that can be obtained by adopting an approach that accepts the additional uncertainties associated with observations without stop point.

Only observations with the following position information sources are presented in this section: *pointer in web map* and *pointer in regObs app*. In these categories of observations, a total of 195 avalanche observations from 2014 - 2019 were evaluated. 55 (28%) of these had at least one match, while 140 (72%) had no matching detections.

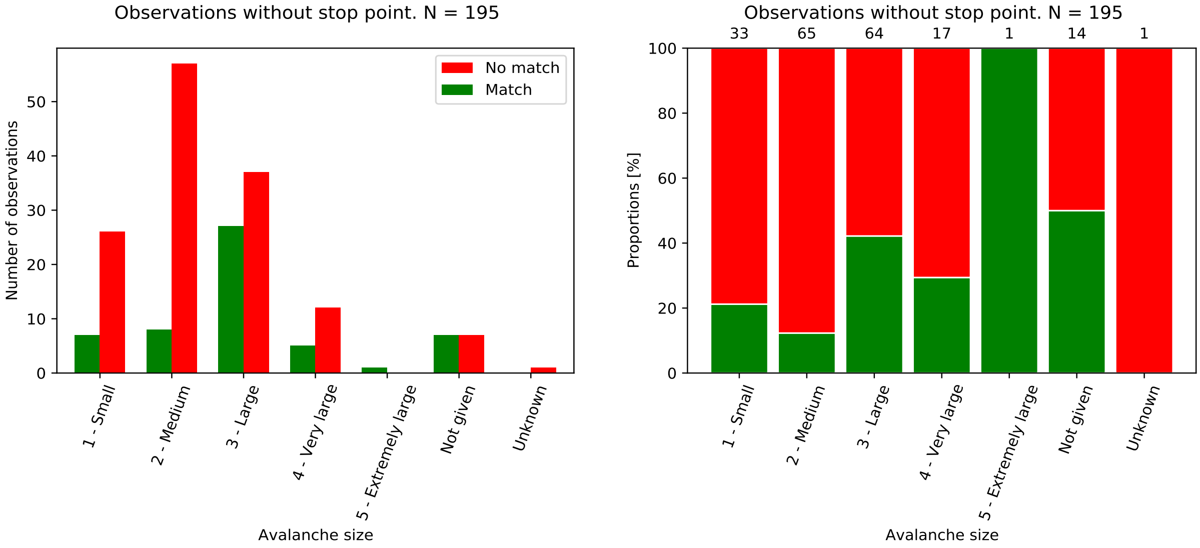

(a) **(b)**

Figure 5.27: Reported avalanche size plotted for observations without stop point. The observations are classified into observations with at least one match (green) and without matches (red), and plotted by number (a) and proportions (b) within each avalanche size.

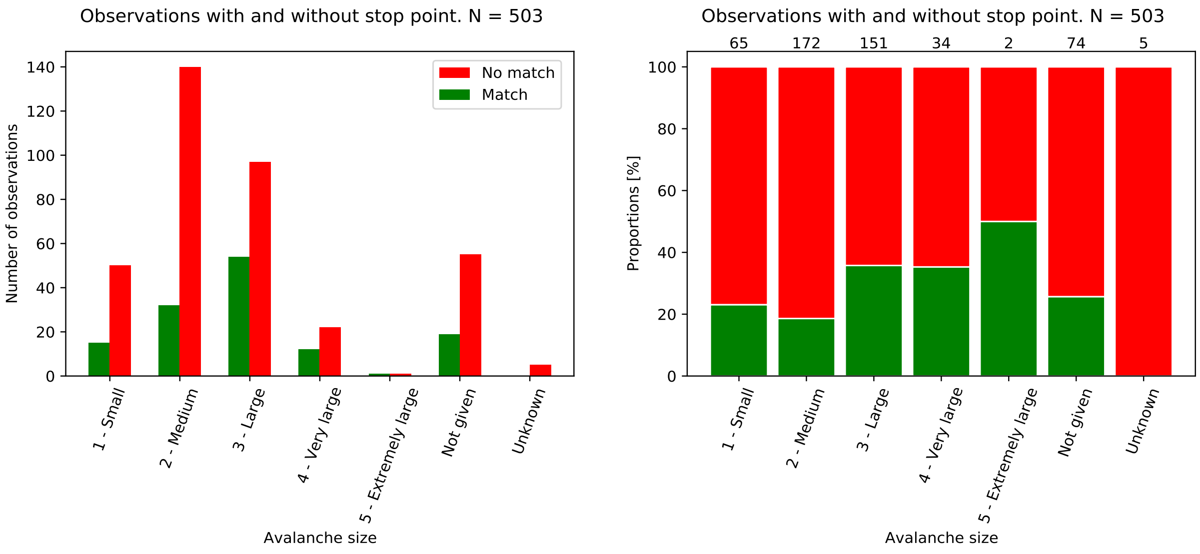

(a) **(b)**

Figure 5.28: Reported avalanche size plotted for observations regardless of stop point. The observations are classified into observations with at least one match (green) and without matches (red), and plotted by number (a) and proportions (b) within each avalanche size.

Figure 5.28 illustrates the distribution of reported avalanche size of observations regardless of stop point information. The result is equivalent to combining Figures 5.11 and 5.27. A trend of higher match percentages for the *Large* and *Very large* avalanches compared to *Small* and *Medium* avalanches is found in Figure 5.11. This trend is also present in Figure 5.28.

6

Discussion

This chapter comprises two main sections. In section 6.1, the comparison algorithm is discussed with emphasis on design choices, selection of input data and performance in general. Section 6.2 is a discussion of the results obtained from running the comparison algorithm to classify observations. The implications from the results on the performance of the Satskred avalanche detection algorithm are also discussed in section 6.2.

6.1 The comparison algorithm

6.1.1 Design

The design and workflow of the comparison algorithm is presented in section 4.2. The algorithm is designed to evaluate the temporal and spatial similarity of all the detections against each of the observations. A general assumption is made that all avalanche observations from regObs represent an avalanche occurrence. The observations can thus be used as a set of true avalanche events. The algorithm design reflects this assumption by evaluating the detections against observations. The reversed comparison of evaluating how many detected avalanches are also observed in the field is not considered relevant for improving the understanding of the detection algorithm performance. The reason being the satellite data enabling detecting avalanches in remote locations regardless of light- , weather- and avalanche danger conditions (Section

3.1).

Temporal comparison

The timeframe between the image time of the reference image (t_0) and the activity image time (t_1) limits the precision of the time comparison. The change detection states that the avalanche time of the detected feature must be within the t_0 - t_1 timeframe. The interesting design choice with regards to time is deciding how to relate the observation time of the avalanche observation to this timeframe. The avalanche time is entered and sometimes explained in the comments of the regObs entry, and other times only guessed at if the observation refers to an older avalanche. The implementation of a timeslack variable ensured that observation times after the change detection timeframe was allowed. The drawback of this approach is that observations entered to the regObs database shortly after the avalanche release time would benefit from a very short timeslack to avoid false matches. Meanwhile, observations of older avalanches would be disregarded if the avalanche release time was late in the change detection timeframe and a short timeslack was applied. An attempt to optimize the timeslack value to suit both these conflicting interests can be found in section 5.1, where the five day timeslack was decided on.

An alternative design avoiding the timeslack could be to perform the time comparison with the estimated avalanche time from the observation. This approach was not chosen due to the avalanche release times being considered too uncertain to rely on without reading the attached comments. The observation times, on the other hand, are assumed to be more accurate.

The avalanche observations in the regObs data base originating from ground radar- or infrasound- detections have accurate avalanche release times (Section 3.2.1). Therefore, a time comparison especially designed for these observations could be implemented using the estimated avalanche release time without the need of a timeslack variable.

Spatial comparison

The spatial similarity was evaluated using drainage basins in addition to scoring and thresholding of aspect and distance. The reasoning and effectiveness of each of the three criteria is discussed below.

The drainage basin approach is very effective as an initial rough filtering. For every observation, the number of timematches is much higher than the number of time-DB-matches with average values of 641 and 18, respectively.

The advantage of computing further statistics for 18 detections, as opposed to 641, is obvious. However, similar results could have been expected from a much more simple radial threshold or a bounding box. The other reason for using drainage basins is that the watersheds defining the boundaries of the drainage basin by definition, follows the highest points in the terrain (Figures 4.2 and 4.10). Therefore, the drainage basin filtering has the added benefit of dividing the AOI into regions in a way that detections with a different drainage basin membership can be disregarded as potential match candidates. This is highly beneficial where an observation is close to e.g a ridge, and therefore possibly close in distance to detections on the other side of the ridge. If the only spatial filtering applied was a simple distance threshold, such detections could have been considered matches. The assumption that observers are highly unlikely to misplace a stop point to the extent that it is assigned a different drainage basin membership is considered strong.

The drainage basin approach also has its drawbacks. First, the drainage basin raster must be prepared in advance and is not computed automatically when running the algorithm. This is an advantage when running the algorithm multiple times for the same area. However, if the algorithm was to be applied to a new region, such as entire Norway, preparing the drainage basins is tedious work and requires at least a basic understanding of GIS.

The second problem using drainage basins is the lower boundary in the terrain. Although the drainage basins fulfill their purpose along mountain tops and ridges, applying a strict drainage basin filter in the lower parts of the terrain is less meaningful. As a result, if an observation is located close to the lower drainage basin border, some of the potential matches could be incorrectly disregarded. This is not considered to introduce any significant errors in the results presented. One alternative approach to avoid the lower border problem is to draw lines along the prominent terrain features where matches on either side should not be allowed. Then, detections located where a straight line from the observation to the detection would have to cross the drawn line, would be filtered out.

Aspect score is assigned to the remaining detections after drainage basin filtering, the *time-DB-matches*. The purpose of evaluating the aspect is to reduce the score of detections located on slopes that are considered less likely to be where the avalanche registered in the avalanche observation entry is located. Thereby, false matches from detections on the opposing side of a valley can be avoided. Much of this score reduction is already taken care of by the distance scoring function. From Figure 5.7 it can be interpreted that aspect scoring becomes more influential for higher values of the sigma parameter of the distance scoring function. One problem with the aspect scoring approach became apparent from the manual validation of the algorithm results in subsection 5.2.2. One observation was incorrectly not assigned any matches even though the manual comparison concluded that two of the nearby detections most likely represented the same avalanches visible in the attached images. The explanation for this is likely twofold: The images suggest that the map pointer locating the stop point could be misplaced by roughly 400 m, and the valley where the avalanches occurred made the misplacement severe with respect to aspect difference. In general, the aspect scoring approach is not expected to introduce many similar errors, but the sensitivity to stop point placement in narrow valleys is noteworthy.

An alternative to evaluate aspect difference was explored in an early version of the comparison algorithm. Drainage basins divided into so-called *half-basins* along the rivers produced comparable results to evaluating aspect difference. The interpretation of detections located in the opposite half-basin was that they belonged to slopes of unacceptably large aspect difference and therefore should be disregarded. The reason why the half-basin design was abandoned is another drawback in addition to the two described above. The border between half-basins in the uppermost part of a valley creates a strict boundary between terrain that is essentially the same. The aspect scoring approach has no trouble evaluating detections in the upper part of a drainage basin correctly, and was therefore preferred over half-basins.

The most intuitive and essential spatial similarity measure applied by the comparison algorithm is the distance between an observation and the potential match candidates. In section 5.1, the sensitivity of the sigma parameter on the match count is illustrated by several figures (e.g Figure 5.3 and Figure 5.8). The sigma value of 300 appears to be reasonable from reviewing the algorithm results, and the Lyngseidet area in particular (Subsection 5.2.7). From the false matches identified by the manual validation, it should be argued that higher sigma values will likely result in a large increase in false matches. Ideally, this sensitive parameter would have been decided using a complete truth-set of confirmed matches if such a set was available.

6.1.2 Selecting useful regObs data

The different data categories of the regObs database is presented in section 3.2. Three main types of snow related entries are considered potentially useful for comparison with avalanche detections: *Avalanche observation*, *avalanche activity* and *danger sign*. In order to get the highest quality results, the main focus was placed on making the comparison algorithm compatible with evaluating *avalanche observation* type entries. The avalanche observations were considered to be more directly comparable to the detections, as they only refer to a single avalanche event and the observer has the option of specifying the stop point of the avalanche.

The stop point information is of great value for automatically comparing observations to detection polygons, as the avalanche detections represent avalanche debris. When using observations with stop point, there is no uncertainty related to which part of the avalanche the observer was referring to. Furthermore, the minimum elevation point is a natural choice for point representative of the detection polygons when calculating distance between the polygon and the stop point given in the observation. The total number of observations with stop point within the AOI in the 2014 - 2019 period was 308. Ideally, the number should be higher to be able to be confident in the conclusions inferred from the algorithm results.

One way of raising the number of observations is to add the avalanche observations without registered stop points. Doing so requires a number of difficult design choices, and introduces a number of new uncertainties that must be dealt with. The most obvious problem is the avalanche location. If no stop (or start-) point is given, the only option is to rely on the position related to the registration in general. As the registration location can refer to any point of the avalanche, the observer location in the field or indeed the home address of the observer, a significant uncertainty is introduced here. Even so, the general impression from manually reviewing the observations from Tromsø and Lyngen for 2018 - 2019 is that the registration location mostly can be trusted to refer to the avalanche location. Another impression from the comments, map pointers and images of the same observations is that observers often focus on the release area of the avalanche instead of the debris. An additional spatial uncertainty related to the size of the avalanche is thus introduced.

In section 5.1.2, a method for handling the positional uncertainties associated with observations without stop point was proposed. The sigma parameter of the distance scoring function was adjusted dynamically to account for the reported avalanche size, and stated positional uncertainty of the registration. One weakness of the method proposed, is the large impact on sigma from typical path length of the different avalanche sizes. As a result, the classification of observations of certain avalanche sizes could become biased for avalanches of significantly different length than the typical path length. This effect may partly explain the relatively large match numbers for avalanches of reported size *3-Large* in Figure 5.27. In order to keep the positional uncertainties at an acceptable level, observations with location information set using the GPS position of a smartphone was disregarded. These were considered the observations most likely to refer to a point far from the avalanche, as they certainly correspond to the observers' location when registering the avalanche observation to the database. The resulting number of observations without stop point is 195, which brings the total number of observations up to 503, provided that the added uncertainties can be accepted.

The *avalanche activity* type entries of single avalanches can likely be handled similar to the avalanche observations without stop point. The possibility that the regObs entry could comprise several observation types should be kept in mind when relying on the registration location. In these cases, the registration location could well refer to e.g a snow profile from the same trip. The same considerations apply when using the *danger sign* entries of recent avalanches, and avalanche observations where an uploaded image is the only information added to the regObs entry. If appropriate measures to account for the positional uncertainties are found, a substantial increase in number of useful data samples can be expected.

6.2 Interpreting results: Detection algorithm performance

The performance of the Satskred avalanche detection algorithm is discussed in this section on the basis of the results from section 5.2. The detection performance with regards to avalanche size, avalanche type, slope angle and aspect is discussed in separate subsections. Further, the results from the Lyngseidet focus area are discussed before some of the masks applied in the detection algorithm are evaluated. Even though a manual validation of the results was conducted for some of the observations, all numbers presented in this section represent the classification by the comparison algorithm, if nothing else is specified.

The results from running the comparion algorithm can be used to evaluate the performance of the Satskred avalanche detection algorithm. Even though the avalanche observations are associated with some degree of positional uncertainty, they are trusted to represent real field events. Furthermore, an avalanche observation without matches is interpreted as a non-detected avalanche. This reasoning was found to be valid for 49 out of the 50 classified observations of size 1, 4 and 5 validated by the manual comparison using all available information (Subsection 5.2.2). In general, the comparison algorithm is considered more prone to including false matches than incorrectly disregarding true matches.

Eckerstorfer et al. (2019) found a probability of detection (POD) of 57% for the automatic detection algorithm by comparing it to a set of 243 field observations. The POD obtained from counting the number of regObs avalanche observations with matches is 25.3% (78 out of 308) (Section 5.2). The large difference in

POD for the two field validations is likely to stem from the properties of the avalanches included in the two sets and will be revisited in subsection 6.2.2.

6.2.1 Avalanche size

The true size of the observed avalanches is not known, and not all of the regObs entries have images attached, making a complete manual validation of the reported sizes difficult. Therefore, without knowledge of systematic over- or under-estimation of avalanche size by the observers, the reported size is trusted when discussing avalanche sizes.

From dividing the observations into groups of each reported avalanche size, a trend of higher match proportions for observations of the larger sizes could be seen from Figure 5.11. This trend was further reinforced when accounting for the high number of false matches in the size 1-*Small* category. Consequently, the field validation suggests a very low detection capability of avalanches of size 1.

One problem when inferring knowledge of detection capability from the comparison algorithm results in general, is the option to not enter information such as avalanche size and avalanche type. If the 60 observations without specified avalanche size truly represent the other sizes in a significantly skewed manner, the identified trends may be false. One way of reducing the number of unspecified avalanche sizes and types would be to suggest that the observers from drift@svv could start to specify this information, as they already estimate the avalanche debris volume.

In despite of the identified size trend, the single avalanche of reported size 5-*Extremely large* was not detected. This avalanche was a dry slab avalanche observed in February 2017 near Kattfjordeidet on the Kvaløya island (Figure 6.1). The reason why this avalanche was not detected is unclear. However, the possibility that much of the avalanche debris was deposited on a small frozen lake (not included in the photo) below the slope can not be ruled out. If that is the case, a change detection feature corresponding to this avalanche debris could have been disregarded by the water mask.

Figure 6.1: Image attached to the regObs observation of the only avalanche of reported size 5-*Extremely large*. The crown can be seen below the cliffs and spans the width of the image. Photo by Silje Lauritsen, retrieved from www.regobs.no

6.2.2 Avalanche type

The results from dividing the classified observations into avalanche types give some interesting hints with regards to detection algorithm performance. For slab avalanches and loose snow avalanches, the wet avalanche type had the highest POD (Figure 5.12). This is consistent with the findings of Eckerstorfer et al. (2019), who found, through field validation, that the detection algorithm performed better for wet snow conditions than dry. With that said, none of the five slush avalanches observed in the 2014 - 2019 period were detected. Other factors than liquid water content of the avalanche debris are likely to explain this, as slush avalanches rarely stop before reaching water or the sea (NVE, 2013).

Some of the missed detections of cornice fall avalanches could potentially be explained by the area covered by cornice fragments being too small to exceed the 10 - pixel area threshold applied by the detection algorithm. For larger avalanches triggered by the cornice fall, this may not be the full explanation.

The data set of field observed avalanches applied by Eckerstorfer et al. (2019) consisted of 90% wet avalanches, out of which the vast majority was slab avalanches. In the set of the regObs avalanche observations, on the other hand, the dry avalanches (dry slab + dry loose) are represented, with 52% of the total. The difference in POD found by comparing each field set to the automatic avalanche detections, can partly be explained by the proportions of dry- and wet avalanches in the sets. However, the match proportions illustrated in Figure 5.12 do not suggest a POD of more than 50% for any set of field observations, regardless of the avalanche type distribution. Therefore, the avalanche type distributions alone do not account for the difference in POD.

By investigating the observation time, December and April were identified as the extremes with regards to low and high proportions of matches, respectively (Subsection 5.2.4). This is also partly explained by the avalanche types, as the majority of December avalanches were dry slab avalanches. Furthermore, the results for April showed that wet slab avalanches were over-represented compared to the overall type distribution illustrated in Figure 5.12. Curiously, several of the avalanche types had a higher match percentage in April than their overall percentage (Figure 5.16). Eckerstorfer et al. (2019) suggested that avalanches with low surface roughness were difficult to detect. If an argument can be made that the surface roughness of April avalanches is above average, and similarly below average for December avalanches, the surface roughness could potentially explain the large difference in match percentages for the two months.

The backscatter contributions from dry and wet snow are illustrated in Figure 2.4 for both undisturbed snow and avalanche debris. The partial transparency of dry snow to C-band microwave radiation may cause a weaker backscatter difference from dry avalanche debris, thus preventing these avalanches from being detected. One suggestion could be to experiment with avalanche detection based on images from radars of higher frequencies, such as X-band, to have a larger backscatter contribution from the air-snow interface, and possibly a higher POD for dry avalanches.

6.2.3 Slope angle and aspect

Some aspects may be over-represented due to installations such as ground based radars and infrasound detection systems. Regarding detection capabilities, no dependencies on slope angle or aspect were possible to identify from Figures 5.18 and 5.19. However, in order to confidently compare slope angle and aspect distributions between the match and no match categories, a larger number of samples would be required.

6.2.4 Lyngseidet

From Figure 5.10, a tendency towards avalanches being observed and registered in popular areas for backcountry recreation, close to public roads and at the locations of avalanche detection systems. Lyngseidet was identified as an area with a low proportion of detected avalanches (9%) and therefore investigated further in subsection 5.2.7. The classification performed by the comparison algorithm was validated manually and found to be correct for all 33 avalanche observations.

The single duplicate observation in the Lyngseidet area was likely caused by the regObs platform user being inexperienced, or by the user struggling with the Norwegian questions in the avalanche observation form, according to the attached comments. In general, duplicate observations of the same avalanche event could be a problem when relying on regObs data. With that said, the manual validation of the comparison algorithm result does not indicate that duplicates are common enough to significantly affect the results. Creating a reliable automatic algorithm to check for duplicates is likely difficult, as two different observations close in time and space do not necessarily refer to the same avalanche. Evaluating images of the avalanches would be a more reliable approach to determine if similar observations are indeed duplicates.

The low detection probability in the Lyngseidet area is unlikely explained by avalanche size, avalanche type or slope angle, as none of these distributions differ significantly from the overall. Two of the non-detected avalanches had reported stop points in areas masked out by the glacier mask. Therefore, if these avalanches were detected, they would likely not be included in the data set of avalanche detections. However, one example that the masked out detections in some cases can match an observed avalanche was found in the Lyngseidet area. After masking, the small fractions of one polygon was found to likely represent one avalanche observation (Figure 5.21 and Figure 5.22). If these small residue-polygons are undesirable, the 10-pixel area threshold could be applied again after masking to make sure the masked out detections are removed completely. In summary, the glacier mask could be responsible for 2 of the 30 non-detected avalanches observed within the Lyngseidet area. The forest mask and agriculture mask do not appear to inhibit detection performance.

The low number of different observers contributing to the regObs database in the Lyngseidet focus area is not considered a problem with regards to reliability, and is unlikely a factor explaining the low proportion of matches. The overall impression is that the regular observers are competent and know the area well. Regardless of observer competence, an observer is trusted to be able to place a pointer in the map with reasonable accuracy.

7

Conclusions

In this thesis, I designed, implemented and tested a prototype algorithm for automatic comparison of avalanche detections to crowd-sourced avalanche observations from regObs. The effectiveness and general performance of the comparison algorithm has been evaluated and discussed with emphasis on algorithm design and choice of input data. The main design features of the comparison algorithm relate to assessment of spatial and temporal similarity of observations and detections. Drainage basin regions and aspect maps were used in addition to distance calculations to evaluate spatial similarity. The change detection timeframe between reference- and activity image was extended by a timeslack variable and was required to span the observation time if the detection was to be considered a time-match. The optimal parameter settings for the comparison algorithm were estimated through running the algorithm multiple times and adjusting one parameter at the time. Strict parameter settings in time and space led to disregarding a large number of detections and consequently very few matches. Too relaxed parameter settings (i.e large timeslack and a large sigma of the distance scoring function) were found to give a high number of false matches that likely did not represent the same field event.

The field observations from regObs were used as a truth-set, and the performance of the Satskred detection algorithm was quantified by counting the number of observed avalanches detected. Thus, by further investigation of the information attached to the regObs entries, the detection algorithm performance was evaluated for different scenarios.

The main conclusions of the study can be summarized as follows:

- Validation of Sentinel-1 borne snow avalanche detections can be conducted systematically by an automated comparison scheme based on crowd-sourced avalanche observations from regObs. The comparison algorithm enables validation of avalanche detections without the workload associated with manually reviewing all the observations. In general, the presented comparison algorithm was effective, and a manual assessment of all regObs entries of avalanche size 1-, 4- and 5 supported the classification results in the vast majority of the cases.

- The reliability of the comparison is largely influenced by the accuracy of the information entered by the observer. Entries within the regObs category *Avalanche observations*, and especially observations with specified avalanche stop point information, were found most directly comparable to the Satskred avalanche detections. The stop point location was sought after, as the stop point could be directly compared to the minimum elevation point of the detected avalanche debris regardless of avalanche path length. Avalanche observations without stop point, *avalanche activity* entries and *danger sign* entries were considered not applicable as comparison algorithm input. If the positional uncertainty associated with these observation categories can be addressed properly, the amount of regObs data applicable for automatic comparison purposes can be increased substantially.

- By counting observations with at least one match, the resulting probability of detection (POD) for the Satskred detection algorithm was 25.3% (78 out of 308). A large part of the field observed avalanches were dry slab avalanches, which the Satskred detection algorithm has problems with detecting. The probability of detection was found to depend on both avalanche type and avalanche size, which is in line with the findings of Eckerstorfer et al. (2019). The POD differed significantly from the 57.3% POD found by Eckerstorfer et al. (2019). The large difference was mostly attributed to dry avalanches being over-represented in the regObs set and likewise for wet avalanches in the validation set applied by Eckerstorfer et al. (2019). Evidently, dry snow avalanches are difficult for the Satskred algorithm to detect and could be an important focus forward when building a reliable avalanche activity monitoring system for forecasting purposes.

- The Lyngseidet area was chosen as a focus area due to a high density of avalanche observations without matching detections. The distribution of reported avalanches with regards to factors such as size and type did not differ significantly from the respective distributions from the entire area of interest. The masks applied to the features detected by the Satskred algorithm was investigated along with avalanche observation locations. The glacier mask was found to likely be responsible for two missed matches in the Lyngseidet focus area. This shows that the masking approach designed to reduce the number of false alarms also reduces the POD. The reason why the Lyngseidet area in general had a relatively low proportion of observations with matches is unclear.

/8

Further work

8.1 Implementation into Satskred processing chain

The comparison algorithm could, with some adjustments, be implemented to the operational processing chain at NORCE to automatically compare detections to the regObs database every time new Sentinel-1 images are available. For new detections within the AOI, the main adjustment needed is to compute the minimum elevation points of the detections polygons at runtime. The minimum elevation points associated with the 44048 detections studied in this thesis were pre-computed, stored locally and taken as algorithm input to avoid the time consuming computations every time the algorithm ran. When running the comparison algorithm for longer time periods, such as entire seasons, the minimum elevation points should be computed in advance.

Alternatively, if the coordinates of the minimum elevation points are easily accessible during the last stages of the Satskred algorithm, these coordinates could be outputted along with the other metadata of the detection polygon shapefile.

If the Satskred detection algorithm is expanded to detect avalanches in all of Norway, the comparison algorithm would have to be adjusted accordingly. Expanding the current version of the comparison algorithm involves e.g computing larger versions of the input maps. The production of input files would preferably be automated, as this is tedious work even for the relatively small Satskred AOI. The main focus should be placed on automating and improving the production of drainage basin maps, as the procedure used in this study involved several computationally expensive steps.

8.2 Use of other observation categories in regObs

The regObs database comprises snow related observations of different types (Subsection 3.2.1). Anyone with a registered account are allowed to enter their relevant observations, the information is presented *as is* and the quality and actuality can not be guaranteed. Even though the observers accounts are assigned a competence level, many of the optional information fields can be left blank, also for highly competent observers. When using regObs observations as a truth-set to evaluate the performance of another information source, accurate and complete observations are sought after. The regObs data would become even more valuable for validation purposes if observers were instructed to specify the avalanche stop point location. Furthermore, for more detailed investigations of size and type of detected and non-detected avalanches, incomplete information of these factors is detrimental to statistical analysis. The observers entering avalanche observations on behalf of the Norwegian Public Roads Administration (account: *drift@svv*) could thus be instructed to specify avalanche type and size, as this account registered a large proportion of the entries without this information (Subsection 5.2.2).

In this thesis, avalanche observations with stop point was used. Avalanche observations without stop point, image-only entries, avalanche activity entries and danger signs are all potentially useful and combined these observations greatly outnumber the avalanche observations with stop point. However, without stop point information, evaluating the spatial similarity to detections is challenging. The proposed approach for estimating the sigma parameter of the distance scoring function in these cases must be revised, as it is expected to introduce many false matches for the larger avalanche sizes. One possible approach to reduce false matches could be to make the distance cutoff boundary elliptical and align the major axis of the ellipse with the local slope gradient.

For the purpose of field validating avalanche detections, a new category of quality controlled avalanche observations could potentially be introduced to the regObs database. Observations in this category would be required to be complete and include images to enable manual validation of the registered information.

8.3 Optimal parameter settings for the comparison algorithm

The comparison algorithm performance is dependent on the selection of parameter values (Section 5.1). The tuning of parameter values was performed through multiple algorithm runs with slightly different parameter settings, adjusting the parameters one at the time. Ideally, if a set of confirmed matches was available, the parameters of the comparison algorithm could be chosen so that the classification results were as close as possible to the confirmed set.

In the absence of such a set, a manual evaluation of the regObs entries with all ancillary information could be used for tuning of the parameters. This kind of manual validation was performed for 50 of the 308 avalanche observations used in this study. The manual approach is labour intensive, and even more so when recognizing that the 2019 - 2020 season raises the count of avalanche observations with stop point by more than 140 new entries. Nevertheless, the work could very well be worthwhile as the result is valuable training data for finding the optimal comparison algorithm parameter values.

9

Appendix

Table 9.1: The 308 avalanche observations with stop point classified by the comparison algorithm.

RegID	ObsDate	Matches	ObjectID of matches	Best match tot. score	Avalanche size	Avalanche type
52818	2015-02-20	2	24239 40477	0.87	4 - Very large	Dry slab
79710	2016-01-31	2	6769 21194	0.47	Not given	Not given
79717	2016-02-02	3	6769 21192 21194	0.96	Not given	Not given
79718	2016-02-02	2	6768 21193	0.72	Not given	Not given
78933	2016-02-06	2	44 11877	0.68	3 - Large	Dry slab
79025	2016-02-06	1	6745	0.52	1 - Small	Dry slab
79386	2016-02-06	2	44 11877	0.74	Not given	Not given
79163	2016-02-07	2	2687 6744	0.06	2 - Medium	Dry slab
91234	2016-03-29	1	22672	0.2	2 - Medium	Dry slab
92304	2016-04-06	1	43708	0.68	3 - Large	Unknown
92308	2016-04-06	3	12709 33148 33149	0.25	1 - Small	Dry slab

Continued

RegID	**ObsDate**	**Matches**	**ObjectID of matches**	**Best match tot. score**	**Avalanche size**	**Avalanche type**
94357	2016-04-16	3	5822 5823 5825	0.89	2 - Medium	Wet slab
98423	2016-05-23	2	37201 37202	0.32	3 - Large	Wet slab
109159	2017-01-06	1	11643	0.08	2 - Medium	Dry slab
112517	2017-01-27	1	11120	0.07	3 - Large	Dry slab
115213	2017-02-17	1	42172	0.01	1 - Small	Dry loose
119839	2017-03-18	2	5190 33423	0.83	3 - Large	Dry slab
119883	2017-03-18	2	5184 25311	0.08	1 - Small	Dry slab
120218	2017-03-20	2	5190 33423	0.99	3 - Large	Dry loose
120461	2017-03-22	4	25373 26563 33427 39601	0.96	3 - Large	Dry slab
121317	2017-03-27	4	1046 5483 5484 6351	0.83	2 - Medium	Dry slab
121534	2017-03-28	1	5502	0.27	2 - Medium	Dry slab
121936	2017-03-31	1	18389	0.57	3 - Large	Dry slab
122122	2017-03-31	4	1670 6350 18371 31744	0.77	4 - Very large	Dry slab
122253	2017-04-01	3	18407 26983 31771	0.57	4 - Very large	Dry slab
122609	2017-04-04	4	8102 13778 29760 37952	0.1	4 - Very large	Wet slab
122622	2017-04-04	6	8090 8099 8100 13776 29754 37950	0.99	Not given	Not given
166767	2017-04-04	4	21345 21347 29405 29409	0.71	2 - Medium	Not given

Continued

RegID	ObsDate	Matches	ObjectID of matches	Best match tot. score	Avalanche size	Avalanche type
122646	2017-04-04	4	21345 21347 29405 29409	0.82	2 - Medium	Wet loose
122677	2017-04-04	10	13654 18369 18370 21333 26975 29368 31741 31742 31743 37830	0.92	3 - Large	Wet slab
166764	2017-04-04	1	29407	0.88	1 - Small	Dry loose
122777	2017-04-05	4	8098 13775 37949 45071	0.91	3 - Large	Wet slab
123185	2017-04-07	1	21353	0.88	3 - Large	Wet slab
123418	2017-04-08	3	29652 36825 36831	0.99	2 - Medium	Dry slab
123471	2017-04-09	6	7926 13727 21415 29579 36774 37909	0.5	2 - Medium	Dry slab
123948	2017-04-12	2	36679 36686	0.22	2 - Medium	Dry slab
124747	2017-04-19	1	25560	0.02	2 - Medium	Wet slab
125045	2017-04-21	1	13348	0.88	3 - Large	Glide-snow
126769	2017-05-05	7	4853 4854 9581 9582 16606 32188 32190	0.79	2 - Medium	Wet slab
126965	2017-05-07	1	15395	0.29	2 - Medium	Dry slab
127131	2017-05-09	1	24197	0.44	4 - Very large	Dry slab
127729	2017-05-16	1	24199	0.1	3 - Large	Not given
127725	2017-05-16	1	24199	0.12	3 - Large	Wet slab
140817	2018-01-16	1	8943	0.57	3 - Large	Not given
140813	2018-01-16	1	8943	0.07	3 - Large	Dry slab

Continued

RegID	ObsDate	Matches	ObjectID of matches	Best match tot. score	Avalanche size	Avalanche type
151286	2018-03-18	1	9030	0.29	2 - Medium	Dry slab
155675	2018-04-02	3	24465 33578 44733	0.63	Not given	Not given
155702	2018-04-02	4	14412 24455 33570 44727	0.9	3 - Large	Dry slab
155650	2018-04-02	1	24461	0.19	2 - Medium	Dry slab
155653	2018-04-02	3	24459 24461 44728	0.4	2 - Medium	Dry slab
155740	2018-04-02	3	24459 33574 44728	0.82	3 - Large	Dry loose
158054	2018-04-11	1	9823	0.13	3 - Large	Not given
166717	2018-04-11	1	9823	0.14	3 - Large	Not given
162884	2018-04-28	1	33761	0.06	1 - Small	Wet slab
162982	2018-04-29	2	30818 33743	0.97	1 - Small	Wet loose
164270	2018-05-10	1	7498	0.12	4 - Very large	Wet slab
182385	2019-01-10	6	928 12183 12184 12185 18782 18783	0.94	Not given	Not given
175494	2019-01-12	8	952 955 2157 12205 12409 12410 18822 40165	0.97	Not given	Dry slab
175493	2019-01-13	16	955 957 958 2157 12205 12409 12410 12411 18822 18825 18827	0.79	Not given	Dry slab

Continued

RegID	ObsDate	Matches	ObjectID of matches	Best match tot. score	Avalanche size	Avalanche type
			23309 39611 40165 40168 40170			
181034	2019-02-14	2	30379 30384	0.85	3 - Large	Wet slab
182384	2019-02-15	4	30398 30399 33459 33460	0.73	Not given	Not given
196416	2019-03-02	5	1892 1898 1903 20877 208790	0.95	Not given	Not given
196417	2019-03-02	2	1903 20879	0.09	Not given	Not given
183809	2019-03-02	1	45023	0.48	2 - Medium	Not given
183985	2019-03-03	1	16960	0.33	3 - Large	Dry slab
184331	2019-03-05	1	21023	0.98	2 - Medium	Dry slab
188668	2019-03-28	6	3082 3084 35163 35164 44104 44580	1.0	3 - Large	Not given
188807	2019-03-29	1	44172	0.28	3 - Large	Dry slab
189005	2019-03-30	5	3033 3034 3879 28340 28342	0.98	3 - Large	Dry slab
189556	2019-04-02	3	3077 3972 12571	0.91	2 - Medium	Dry slab
189612	2019-04-03	8	3989 12580 20633 28466 35162 44326 44575 44577	0.99	3 - Large	Dry slab
190430	2019-04-09	8	2762 2764	0.52	4 - Very large	Dry slab

Continued

RegID	ObsDate	Matches	ObjectID of matches	Best match tot. score	Avalanche size	Avalanche type
			23423 23424 34741 44307 45307 45314			
190496	2019-04-09	1	23581	0.88	3 - Large	Dry slab
191217	2019-04-14	5	2762 2764 23423 23424 34741	0.26	2 - Medium	Not given
191445	2019-04-15	1	28611	0.96	1 - Small	Wet loose
191340	2019-04-15	1	34741	0.01	2 - Medium	Not given
193780	2019-05-05	3	242 3589 19674	0.71	2 - Medium	Wet loose
193802	2019-05-05	2	212 41312	0.68	2 - Medium	Wet loose
46807	2015-01-20	0	-	-	2 - Medium	Dry slab
50043	2015-02-08	0	-	-	1 - Small	Cornice fall
52333	2015-02-13	0	-	-	Not given	Not given
53175	2015-02-13	0	-	-	Not given	Not given
53176	2015-02-13	0	-	-	Not given	Not given
52312	2015-02-16	0	-	-	Not given	Not given
56125	2015-03-09	0	-	-	Not given	Not given
56403	2015-03-15	0	-	-	2 - Medium	Wet loose
65788	2015-03-16	0	-	-	Not given	Not given
57698	2015-03-26	0	-	-	3 - Large	Dry slab
58717	2015-04-03	0	-	-	1 - Small	Wet loose
59303	2015-04-08	0	-	-	Not given	Not given
59970	2015-04-14	0	-	-	1 - Small	Dry loose
62276	2015-05-07	0	-	-	3 - Large	Wet slab
62288	2015-05-07	0	-	-	4 - Very large	Wet slab
70482	2015-12-13	0	-	-	1 - Small	Dry slab
71836	2015-12-24	0	-	-	2 - Medium	Dry slab
71884	2015-12-24	0	-	-	2 - Medium	Dry slab
74118	2016-01-09	0	-	-	Not given	Not given
74120	2016-01-09	0	-	-	Not given	Not given
74008	2016-01-10	0	-	-	Not given	Not given
77234	2016-01-22	0	-	-	Not given	Not given
76734	2016-01-23	0	-	-	3 - Large	Dry slab
76758	2016-01-23	0	-	-	Not given	Not given
76956	2016-01-24	0	-	-	3 - Large	Dry slab
76964	2016-01-24	0	-	-	2 - Medium	Dry slab

Continued

RegID	ObsDate	Matches	ObjectID of matches	Best match tot. score	Avalanche size	Avalanche type
77441	2016-01-27	0	-	-	3 - Large	Dry slab
78067	2016-01-31	0	-	-	Not given	Not given
79713	2016-01-31	0	-	-	Not given	Not given
78273	2016-02-02	0	-	-	4 - Very large	Dry slab
78334	2016-02-02	0	-	-	Not given	Not given
78927	2016-02-06	0	-	-	3 - Large	Dry slab
79388	2016-02-06	0	-	-	Not given	Not given
79107	2016-02-07	0	-	-	2 - Medium	Dry slab
79162	2016-02-07	0	-	-	4 - Very large	Unknown
79141	2016-02-07	0	-	-	2 - Medium	Dry slab
79158	2016-02-07	0	-	-	3 - Large	Dry slab
81702	2016-02-11	0	-	-	Not given	Not given
82151	2016-02-13	0	-	-	3 - Large	Dry slab
80998	2016-02-13	0	-	-	3 - Large	Dry slab
81063	2016-02-13	0	-	-	Unknown	Dry slab
82438	2016-02-16	0	-	-	Not given	Not given
81601	2016-02-16	0	-	-	2 - Medium	Dry slab
82077	2016-02-19	0	-	-	3 - Large	Dry slab
82191	2016-02-20	0	-	-	2 - Medium	Dry slab
82232	2016-02-20	0	-	-	1 - Small	Dry slab
82212	2016-02-20	0	-	-	4 - Very large	Not given
83884	2016-03-02	0	-	-	3 - Large	Dry slab
83896	2016-03-03	0	-	-	3 - Large	Dry slab
83899	2016-03-03	0	-	-	2 - Medium	Dry slab
89309	2016-03-13	0	-	-	Not given	Not given
90239	2016-03-22	0	-	-	3 - Large	Dry slab
90317	2016-03-22	0	-	-	3 - Large	Dry slab
90586	2016-03-24	0	-	-	2 - Medium	Dry slab
90609	2016-03-24	0	-	-	2 - Medium	Dry slab
90745	2016-03-25	0	-	-	2 - Medium	Wet loose
91373	2016-03-27	0	-	-	2 - Medium	Dry slab
91239	2016-03-29	0	-	-	2 - Medium	Wet loose
91851	2016-04-03	0	-	-	3 - Large	Cornice fall
92427	2016-04-07	0	-	-	1 - Small	Dry slab
94427	2016-04-17	0	-	-	1 - Small	Dry slab
95088	2016-04-22	0	-	-	2 - Medium	Not given
95129	2016-04-22	0	-	-	1 - Small	Wet loose
95970	2016-04-29	0	-	-	3 - Large	Wet slab
96089	2016-04-30	0	-	-	2 - Medium	Cornice fall
96090	2016-04-30	0	-	-	2 - Medium	Cornice fall
96634	2016-05-02	0	-	-	1 - Small	Wet slab
105626	2016-12-09	0	-	-	3 - Large	Dry slab
107699	2016-12-27	0	-	-	2 - Medium	Dry slab
108264	2016-12-31	0	-	-	1 - Small	Cornice fall
112497	2017-01-07	0	-	-	2 - Medium	Dry loose

Continued

RegID	ObsDate	Matches	ObjectID of matches	Best match tot. score	Avalanche size	Avalanche type
109292	2017-01-07	0	-	-	2 - Medium	Dry slab
110418	2017-01-14	0	-	-	1 - Small	Dry slab
111092	2017-01-18	0	-	-	Not given	Not given
112496	2017-01-20	0	-	-	2 - Medium	Dry loose
112110	2017-01-24	0	-	-	2 - Medium	Dry slab
112173	2017-01-25	0	-	-	2 - Medium	Dry loose
112121	2017-01-25	0	-	-	2 - Medium	Wet slab
112178	2017-01-25	0	-	-	2 - Medium	Wet slab
114442	2017-02-11	0	-	-	2 - Medium	Cornice fall
114677	2017-02-13	0	-	-	2 - Medium	Wet slab
116002	2017-02-22	0	-	-	2 - Medium	Dry slab
116825	2017-02-24	0	-	-	Not given	Not given
166768	2017-02-24	0	-	-	3 - Large	Dry loose
116348	2017-02-24	0	-	-	3 - Large	Dry loose
116502	2017-02-25	0	-	-	2 - Medium	Dry slab
116841	2017-02-27	0	-	-	5 - Extremely large	Not given
116857	2017-02-27	0	-	-	2 - Medium	Dry slab
117569	2017-03-04	0	-	-	3 - Large	Dry slab
117867	2017-03-05	0	-	-	2 - Medium	Dry slab
117791	2017-03-06	0	-	-	3 - Large	Dry slab
117996	2017-03-07	0	-	-	2 - Medium	Dry slab
118819	2017-03-12	0	-	-	2 - Medium	Cornice fall
118826	2017-03-12	0	-	-	3 - Large	Dry slab
118829	2017-03-12	0	-	-	3 - Large	Dry loose
118837	2017-03-12	0	-	-	3 - Large	Unknown
118839	2017-03-12	0	-	-	2 - Medium	Dry slab
118905	2017-03-13	0	-	-	3 - Large	Dry slab
119221	2017-03-14	0	-	-	Not given	Not given
119225	2017-03-14	0	-	-	Not given	Not given
119171	2017-03-14	0	-	-	2 - Medium	Dry slab
119832	2017-03-18	0	-	-	3 - Large	Dry slab
120026	2017-03-19	0	-	-	3 - Large	Dry slab
120196	2017-03-19	0	-	-	1 - Small	Dry loose
120337	2017-03-21	0	-	-	2 - Medium	Dry loose
120923	2017-03-24	0	-	-	2 - Medium	Dry slab
121062	2017-03-25	0	-	-	3 - Large	Dry slab
121373	2017-03-27	0	-	-	3 - Large	Dry loose
121918	2017-03-28	0	-	-	3 - Large	Dry slab
121733	2017-03-29	0	-	-	3 - Large	Dry slab
121789	2017-03-30	0	-	-	3 - Large	Dry slab
129188	2017-03-31	0	-	-	Not given	Not given
122391	2017-04-02	0	-	-	2 - Medium	Glide-snow
122469	2017-04-02	0	-	-	2 - Medium	Dry slab
123371	2017-04-08	0	-	-	2 - Medium	Wet loose

Continued

RegID	ObsDate	Matches	ObjectID of matches	Best match tot. score	Avalanche size	Avalanche type
123915	2017-04-12	0	-	-	3 - Large	Cornice fall
124086	2017-04-13	0	-	-	2 - Medium	Dry slab
124568	2017-04-17	0	-	-	3 - Large	Dry loose
124646	2017-04-18	0	-	-	2 - Medium	Dry slab
125033	2017-04-20	0	-	-	Not given	Dry slab
125141	2017-04-22	0	-	-	2 - Medium	Dry slab
125161	2017-04-22	0	-	-	Unknown	Dry slab
125561	2017-04-25	0	-	-	2 - Medium	Wet loose
126302	2017-05-01	0	-	-	4 - Very large	Not given
127839	2017-05-17	0	-	-	1 - Small	Slush
128174	2017-05-20	0	-	-	3 - Large	Slush
166795	2017-05-22	0	-	-	2 - Medium	Not given
128401	2017-05-23	0	-	-	Not given	Not given
128376	2017-05-23	0	-	-	3 - Large	Wet loose
128804	2017-05-27	0	-	-	2 - Medium	Dry loose
133939	2017-12-04	0	-	-	1 - Small	Dry slab
133981	2017-12-05	0	-	-	3 - Large	Dry slab
133990	2017-12-05	0	-	-	3 - Large	Dry slab
137874	2017-12-30	0	-	-	3 - Large	Dry slab
139074	2018-01-07	0	-	-	2 - Medium	Dry loose
149063	2018-01-11	0	-	-	3 - Large	Dry slab
166763	2018-01-18	0	-	-	2 - Medium	Dry loose
142523	2018-01-26	0	-	-	1 - Small	Dry loose
148662	2018-03-03	0	-	-	2 - Medium	Dry slab
148811	2018-03-04	0	-	-	2 - Medium	Dry loose
149574	2018-03-09	0	-	-	2 - Medium	Dry slab
150086	2018-03-12	0	-	-	2 - Medium	Dry slab
150188	2018-03-13	0	-	-	1 - Small	Dry slab
166759	2018-03-17	0	-	-	2 - Medium	Not given
166758	2018-03-17	0	-	-	2 - Medium	Not given
151242	2018-03-18	0	-	-	1 - Small	Dry slab
166756	2018-03-19	0	-	-	2 - Medium	Dry loose
166755	2018-03-19	0	-	-	2 - Medium	Dry loose
151388	2018-03-19	0	-	-	3 - Large	Dry slab
151471	2018-03-19	0	-	-	3 - Large	Not given
151536	2018-03-19	0	-	-	2 - Medium	Dry slab
151757	2018-03-19	0	-	-	3 - Large	Dry slab
152106	2018-03-21	0	-	-	3 - Large	Dry slab
152228	2018-03-22	0	-	-	3 - Large	Dry slab
153159	2018-03-25	0	-	-	2 - Medium	Dry slab
153510	2018-03-26	0	-	-	2 - Medium	Dry slab
153576	2018-03-26	0	-	-	Unknown	Unknown
154152	2018-03-28	0	-	-	3 - Large	Dry slab
154188	2018-03-28	0	-	-	4 - Very large	Dry slab
154701	2018-03-29	0	-	-	Not given	Dry slab

Continued

RegID	ObsDate	Matches	ObjectID of matches	Best match tot. score	Avalanche size	Avalanche type
154817	2018-03-30	0	-	-	Not given	Not given
155230	2018-03-31	0	-	-	3 - Large	Dry slab
166718	2018-03-31	0	-	-	4 - Very large	Dry slab
155287	2018-03-31	0	-	-	4 - Very large	Dry slab
155399	2018-04-01	0	-	-	Not given	Not given
155488	2018-04-01	0	-	-	Unknown	Dry slab
155674	2018-04-02	0	-	-	Not given	Not given
157022	2018-04-07	0	-	-	4 - Very large	Dry slab
157266	2018-04-08	0	-	-	2 - Medium	Dry slab
158355	2018-04-12	0	-	-	3 - Large	Wet loose
158515	2018-04-13	0	-	-	2 - Medium	Wet loose
158741	2018-04-13	0	-	-	3 - Large	Wet slab
159561	2018-04-16	0	-	-	3 - Large	Wet slab
160244	2018-04-18	0	-	-	3 - Large	Wet slab
160477	2018-04-20	0	-	-	3 - Large	Cornice fall
160625	2018-04-20	0	-	-	3 - Large	Wet slab
162487	2018-04-25	0	-	-	2 - Medium	Wet loose
163213	2018-05-01	0	-	-	1 - Small	Not given
163322	2018-05-01	0	-	-	1 - Small	Dry slab
166716	2018-05-04	0	-	-	2 - Medium	Not given
166713	2018-05-04	0	-	-	2 - Medium	Not given
163685	2018-05-04	0	-	-	Not given	Not given
164139	2018-05-09	0	-	-	1 - Small	Wet loose
166710	2018-05-10	0	-	-	2 - Medium	Wet loose
164577	2018-05-12	0	-	-	2 - Medium	Wet slab
175498	2019-01-13	0	-	-	1 - Small	Cornice fall
178482	2019-01-24	0	-	-	Not given	Not given
177575	2019-01-25	0	-	-	Not given	Not given
177540	2019-01-25	0	-	-	2 - Medium	Dry slab
177590	2019-01-25	0	-	-	2 - Medium	Dry slab
177602	2019-01-25	0	-	-	1 - Small	Dry slab
179318	2019-02-03	0	-	-	1 - Small	Dry slab
179381	2019-02-06	0	-	-	Not given	Not given
179955	2019-02-09	0	-	-	2 - Medium	Dry slab
180662	2019-02-12	0	-	-	Not given	Not given
181096	2019-02-12	0	-	-	2 - Medium	Dry slab
180758	2019-02-12	0	-	-	Not given	Not given
182965	2019-02-14	0	-	-	Not given	Not given
182968	2019-02-14	0	-	-	Not given	Not given
195543	2019-02-14	0	-	-	Not given	Not given
182996	2019-02-15	0	-	-	Not given	Not given
181541	2019-02-17	0	-	-	2 - Medium	Dry slab
182973	2019-02-21	0	-	-	Not given	Not given
183617	2019-02-22	0	-	-	Not given	Not given
183447	2019-02-28	0	-	-	2 - Medium	Dry slab

Continued

RegID	ObsDate	Matches	ObjectID of matches	Best match tot. score	Avalanche size	Avalanche type
196418	2019-03-02	0	-	-	Not given	Not given
186595	2019-03-16	0	-	-	2 - Medium	Cornice fall
186904	2019-03-17	0	-	-	2 - Medium	Dry slab
186758	2019-03-17	0	-	-	3 - Large	Dry slab
188095	2019-03-18	0	-	-	Not given	Not given
187125	2019-03-19	0	-	-	2 - Medium	Dry slab
187768	2019-03-23	0	-	-	3 - Large	Dry slab
188467	2019-03-27	0	-	-	3 - Large	Dry slab
189213	2019-03-31	0	-	-	3 - Large	Dry slab
189404	2019-04-01	0	-	-	Not given	Unknown
190125	2019-04-06	0	-	-	2 - Medium	Dry slab
190535	2019-04-09	0	-	-	2 - Medium	Cornice fall
191350	2019-04-15	0	-	-	2 - Medium	Wet slab
191357	2019-04-15	0	-	-	3 - Large	Wet slab
192276	2019-04-22	0	-	-	Not given	Wet slab
192335	2019-04-22	0	-	-	4 - Very large	Wet slab
192627	2019-04-24	0	-	-	3 - Large	Not given
192725	2019-04-25	0	-	-	Not given	Slush
192731	2019-04-25	0	-	-	Not given	Not given
193185	2019-04-29	0	-	-	3 - Large	Wet slab
193723	2019-05-04	0	-	-	2 - Medium	Dry slab
193913	2019-05-06	0	-	-	2 - Medium	Wet loose
194421	2019-05-11	0	-	-	1 - Small	Slush
194497	2019-05-12	0	-	-	2 - Medium	Wet loose
195203	2019-05-21	0	-	-	2 - Medium	Slush

Bibliography

W. Ammann. *Der Lawinenwinter 1999: Ereignisanalyse*. Eidgenössisches Institut für Schnee-und Lawinenforschung, 2000.

Avalanche Canada. glossary, 2020. URL `https://www.avalanche.ca/glossary/#avalanche-path-definition`.

Y. Bühler, C. Bieler, C. Pielmeier, A. Wiesmann, R. Caduff, R. Frauenfelder, C. Jaedicke, and G. Bippus. Allweather avalanche activity monitoring from space. In *Proceedings, International Snow Science Workshop, Banff*, pages 795–802, 2014.

EAWS. Glossary, 2019. URL `https://www.avalanches.org/glossary-2/ loosesnowavalanchepointreleaseavalanche`.

EAWS. Avalanche sizes, 2020. URL `https://www.avalanches.org/standards/avalanche-size/`.

M. Eckerstorfer and E. Malnes. Manual detection of snow avalanche debris using high-resolution radarsat-2 sar images. *Cold Regions Science and Technology*, 120:205–218, 2015.

M. Eckerstorfer, Y. Bühler, R. Frauenfelder, and E. Malnes. Remote sensing of snow avalanches: Recent advances, potential, and limitations. *Cold Regions Science and Technology*, 121:126–140, 2016.

M. Eckerstorfer, E. Malnes, and K. Müller. A complete snow avalanche activity record from a norwegian forecasting region using sentinel-1 satellite-radar data. *Cold regions science and technology*, 144:39–51, 2017.

M. Eckerstorfer, E. Malnes, H. Vickers, K. Müller, R. Engeset, and T. Humstad. Operational avalanche activity monitoring using radar satellites: From norway to worldwide assistance in avalanche forecasting. 2018.

M. Eckerstorfer, H. Vickers, E. Malnes, and J. Grahn. Near-real time automatic snow avalanche activity monitoring system using sentinel-1 sar data in norway. *Remote Sensing*, 11(23):2863, 2019.

C. Elachi and J. J. Van Zyl. *Introduction to the physics and techniques of remote sensing*, volume 28. John Wiley & Sons, 2006.

R. V. Engeset. National avalanche warning service for norway–established 2013. In *Proceedings ISSW*, pages 301–310, 2013.

R. V. Engeset, R. Ekker, T. Humstad, and M. Landrø. Varsom: Regobs–a common real-time picture of the hazard situation shared by mobile information technology. In *Proceedings of the International Snow Science Workshop, 7–12 October, Innsbruck, Austria*, 2018.

ESA. Introducing sentinel-1, 2020. URL `https://www.esa.int/Applications/Observing_the_Earth/Copernicus/Sentinel-1/Introducing_Sentinel-1`.

M. Hallikainen, F. Ulaby, and M. Abdelrazik. Dielectric properties of snow in the 3 to 37 ghz range. *IEEE transactions on Antennas and Propagation*, 34 (11):1329–1340, 1986.

E. R. LaChapelle. The fundamental processes in conventional alavalanche forecasting. *Journal of Glaciology*, 26(94):75–84, 1980.

E. R. LaChapelle. *The ABC of avalanche safety*. Mountaineers Books, 1985.

M. Landrø. *Skredfare : snøskred, risiko, redning*. Fri Flyt AS, Oslo, 2007.

A. Liu and S. Wu. Satellite remote sensing sar. 2001.

E. Malnes, M. Eckerstorfer, Y. Larsen, R. Frauenfelder, A. Jonsson, C. Jaedicke, and S. A. Solbø. Remote sensing of avalanches in northern norway using synthetic aperture radar. In *Proceedings of the International Snow Science Workshop*, pages 955–959, 2013.

E. Malnes, M. Eckerstorfer, and H. Vickers. First sentinel-1 detections of avalanche debris. *The Cryosphere Discussions*, 9(2):1943–1963, 2015.

D. McClung. The elements of applied avalanche forecasting, part i: The human issues. *Natural Hazards*, 26(2):111–129, 2002a.

D. McClung. The elements of applied avalanche forecasting, part ii: the physical issues and the rules of applied avalanche forecasting. *Natural Hazards*, 26 (2):131–146, 2002b.

L. Meier. Radarmålinger av snoskred ved fv. 293 holmbuktura. *Statens vegvesens rapporter*, 2018.

NGI. Ulykker med død, 2019. URL `https://www.ngi.no/Tjenester/Fagekspertise/Snoeskred/snoskred .no2/Ulykker-med-doed`.

NVE. Hva er sørpeskred?, 2013. URL `http://publikasjoner.nve.no/faktaark/2013/faktaark2013_06.pdf`.

NVE. Snøskred - tørre og våte?, 2016. URL `http://publikasjoner.nve.no/faktaark/2016/faktaark2016_01.pdf`.

regObs. Om regobs, 2020. URL `https://www.regobs.no/Home/About`.

S. M. Ross. *Introduction to probability and statistics for engineers and scientists*. Elsevier, 2004.

J. Schweizer. Rutschblock 73–verifikation der lawinengefahr. *Bergundsteigen-Zeitschrift für Risikomanagement im Bergsport. Oesterreichischer Alpenverein, Innsbruck, Austria*, 12(4):56–59, 2003.

J. Schweizer and J. Jamieson. Snow cover properties for skier triggering of avalanches. *Cold Regions Science and Technology*, 33(2-3):207–221, 2001.

J. Schweizer, J. Bruce Jamieson, and M. Schneebeli. Snow avalanche formation. *Reviews of Geophysics*, 41(4), 2003a.

J. Schweizer, K. Kronholm, and T. Wiesinger. Verification of regional snowpack stability and avalanche danger. *Cold Regions Science and Technology*, 37(3): 277–288, 2003b.

F. Techel, C. Mitterer, E. Ceaglio, C. Coléou, S. Morin, F. Rastelli, R. S. Purves, K. Müller, R. Engeset, and K. W. Birkeland. Spatial consistency and bias in avalanche forecasts-a case study in the european alps. *Natural Hazards & Earth System Sciences*, 18(10), 2018.

B. Tremper. *Staying alive in avalanche terrain*. The Mountaineers Books, Seattle, WA, 2008.

F. T. Ulaby, R. K. Moore, and A. K. Fung. Microwave remote sensing: Active and passive. volume 3-from theory to applications. 1986.

USGS. Watersheds and drainage basins, May 2020. URL `https://www.usgs.gov/special-topic/water-science-school/science/`

watersheds-and-drainage-basins?qt-science_center_objects=0#qt-science_center_objects.

Varsom. Hvordan lages et snøskredvarsel?, 2019a. URL https://www.varsom.no/snoskredvarsling/hvordan-lages-et-snoskredvarsel/.

Varsom. Snøskredulykker og hendelser, 2019b. URL https://www.varsom.no/ulykker/snoskredulykker-og-hendelser.

Varsom. Kompetanse, 2020a. URL https://www.varsom.no/regobs/kompetanse/.

Varsom. Varsom:snoskredvarsling, 2020b. URL https://www.varsom.no/snoskredvarsling/?ref=mainmenu/.

Varsom. Snoskredstorrelser, 2020c. URL https://www.varsom.no/snoskredskolen/snoskredvarselet-forklaring/snoskredstorrelser/.

H. Vickers, M. Eckerstorfer, E. Malnes, Y. Larsen, and H. Hindberg. A method for automated snow avalanche debris detection through use of synthetic aperture radar (sar) imaging. *Earth and Space Science*, 3(11):446–462, 2016.

H. Vickers, M. Eckerstorfer, E. Malnes, and A. Doulgeris. Synthetic aperture radar (sar) monitoring of avalanche activity: an automated detection scheme. In *Scandinavian Conference on Image Analysis*, pages 136–146. Springer, 2017.

V. T. Vu, D. N. Nehru, M. I. Pettersson, and T. K. Sjögren. An experimental ground-based sar system for studying sar fundamentals. In *Conference Proceedings of 2013 Asia-Pacific Conference on Synthetic Aperture Radar (APSAR)*, pages 424–427. IEEE, 2013.

D. S. Wesselink, E. Malnes, M. Eckerstorfer, and R. C. Lindenbergh. Automatic detection of snow avalanche debris in central svalbard using c-band sar data. *Polar Research*, 36(1):1333236, 2017.

A. Wiesmann, U. Wegmuller, M. Honikel, T. Strozzi, and C. L. Werner. Potential and methodology of satellite based sar for hazard mapping. In *IGARSS 2001. Scanning the Present and Resolving the Future. Proceedings. IEEE 2001 International Geoscience and Remote Sensing Symposium (Cat. No. 01CH37217)*, volume 7, pages 3262–3264. IEEE, 2001.

Wyssen. Ida - infralydbasert detekteringssystem, 2019. URL https://www.wyssenavalanche.com/nb/detekteringssystemer/ida-infralydbasert-detekteringssystem/.